UNIVERSITEIT GENT

FACULTY OF **SCIENCES**

Radial spin wave modes in magnetic vortex structures

Doctoral thesis
by Mathias Helsen

Thesis submitted to obtain the degree of
«*Doctor in de Wetenschappen, Natuurkunde*»
at the Ghent University, Department of Solid State Sciences.

Public defense: 3rd June 2015
Promotor: dr. Bartel Van Waeyenberge

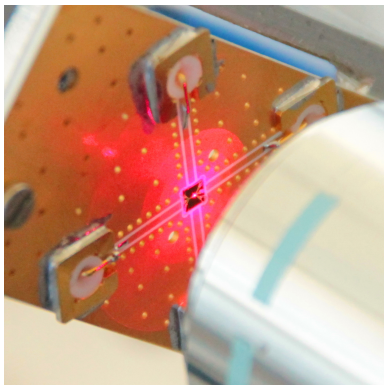

Dankwoord (acknowledgements)

Ik zou willen beginnen door mijn promotor, prof. dr. Bartel Van Waeyenberge, te bedanken voor zijn ondersteuning gedurende mijn doctoraat. Bedankt dat ik jouw deur mocht platlopen om vragen te komen stellen, en je kantoor vol te stouwen met lawaaierige elektronica.

Daarnaast zou ik graag mijn mentor, dr. Arne Vansteenkiste ook willen bedanken voor al zijn goede raad die onontbeerlijk was. En uiteraard om bij te sturen wanneer nodig (i.e. vaak), maar misschien nog het meest om samen koffie te drinken. De werkdag kon en mocht niet beginnen zonder een kop om-ter-sterkste koffie (hoewel de kwaliteit de laatste tijd toch zwaar achteruit ging).

I would also like to thank my former colleague, dr. Mykola Dvornik; your deep cynism and honesty have been inspiring. It was more than once an «educational moment», especially your seminal work on flash-drive reliability.

Daarnaast wil ik ook nog Jonathan en Annelies bedanken, jullie zijn een bijzonder sympatiek koppel en ik was blij om samen met jullie op conferentie te kunnen gaan. Jonathan, uiteraard ook bedankt voor het aanslepen van koffie en flash drives. Hoewel die laatste niet heel erg betrouwbaar bleken (volgens het werk van dr. Dvornik).

A special thanks goes to Ajay Gangwar of the University of Regensburg for preparing all my samples. Ajay, you have been a great colleague and I can not thank you enough for all the samples you prepared for me. Thank you very much.

Another special thanks goes to Markus Weigand and Michael Bechtel of the Maxymus STXM at Bessy II, for helping me setting up the STXM experiments. Sorry calling you at the most inapropriate hours of the day because the software/STXM crashed.

I would like to thank prof. dr. Georg Woltersdorf for joining the reading commitee and thoroughly reading this work. Your comments and suggestions have been

appreciated. Professor dr. ir. Luc Dupré, prof. dr. Erik Folven and prof. dr. Jan Ryckebusch are thanked for joining the jury.

De vrienden-van-de-fysica wil ik bedanken om de sfeer erin te houden, niet alleen voor maar ook na ons afstuderen.

Mijn ouders wil ik bedanken om mij altijd de vrijheid te geven te studeren wat ik wou, en mij daar ook in te steunen.

Zowel het Fonds voor Wetenschappelijk Onderzoek als de Universiteit Gent wens ik te bedanken voor hun financiële steun.

Tenslotte wil ik mijn toekomstige echtgenoot, Nathan, bedanken om mij te steunen wanneer het moeilijk ging, maar voor ook nog oneindig veel meer.

Mathias Helsen,
16 mei 2015.

Voor mijn vader, Achilles Helsen.

Contents

List of Figures

List of Tables

Samenvatting

Computers zijn niet meer weg te denken uit onze huidige maatschappij. Cruciaal hierbij is de mogelijkheid voor het opslaan van gigantische hoeveelheden data. Hiertoe is de dichtheid van de databits op harde schijven (de dominante vorm van opslag) steeds toegenomen sinds de eerste commerciële harde schijf in 1957 (IBM 305 RAMAC). Daarnaast heeft de snelheid waarmee bits geschreven en gelezen worden ook een hoge vlucht genomen.

Dit alles heeft het onderzoeksgebied van het magnetisme in de richting van het «*micromagnetisme*» geduwd. Hier bestudeert men magnetisme simultaan op de micron- en picosecondeschaal. Zo heeft men onder andere niet-triviale (i.e. niet-uniforme) grondtoestanden van de magnetisatie gevonden, zoals «*vortex*»-toestanden. Deze magnetische structuren kunnen ook excitaties bevatten, net zoals men een snaar of vel van een trom kan aanslaan. In dit werk worden een bepaalde soort excitaties (namelijk «*radiale spingolven*») van de vortex grondtoestand bestudeerd.

Hoofdstuk 1 behelst een inleiding tot magnetisme, met speciale aandacht voor magnetische structuren met microscopische afmetingen. Daarnaast worden ook de aangeslagen toestanden van deze structuren geïntroduceerd.

Hoofdstuk 2 start met een bespreking van de bestaande technieken om deze structuren te onderzoeken. Uit deze bespreking blijkt dat er een hiaat is, en het niet mogelijk is om frequentiespectra van geïsoleerde elementen met hoge frequentie resolutie (en in de afwezigheid van een magnetisch veld) te meten. Daarom wordt een nieuwe methode ontwikkeld en die in groot detail beschreven wordt.

Uniforme precessie van een dunne magnetische film wordt in Hoofdstuk 3 aangewend om de nieuwe methode te testen. Deze uniforme precessie wordt zeer vaak gebruikt voor het bepalen van de magnetische eigenschap-

pen van een materiaal. Indien men deze precessie kan meten, is het mogelijk om direct materiaaleigenschappen van microscopische structuren te bepalen.
De radiale spingolven in dunne magnetische schijven worden uiteindelijk bestudeerd in Hoofdstuk 4. Hier wordt nagegaan wat het effect is van de aspectverhouding van deze schijven op de resonantiefrequentie. De resultaten worden vergeleken met theoretische voorspellingen en micromagnetische simulaties. Daarnaast wordt getoond dat het verhogen van de amplitude van de excitatie kan leiden tot niet-lineare effecten. Dit wordt verder uitgewerkt met micromagnetische simulaties, die ook het zelf-focusserend effect aantonen bij zeer sterke velden.

Summary

The hard drive is celebrating its 50th anniversary soon, as the IBM 305 RAMAC (the first commercial hard disc drive) was first put into operation in 1957. Since then, great improvements in both speed and capacity have been obtained in magnetic storage. This trend has been made possible only by decreasing the size of the individual bits of data and writing and reading them faster. Therefore, this work will contribute on the fundamental knowledge of the dynamics of small magnetic structures.
In Chapter 1 we give a broad introduction on magnetism and elaborate on the basic, non-trivial magnetic groundstates of small magnetic elements. Just as a string, or the sheet of a drum, such states can be excited into oscillating behaviour. To study these excited states is the goal of this work.
We start Chapter 2 with a discussion about the existing techniques to probe such excitations and come to the conclusion that a certain approach is missing. More precisely, no method allows measuring the resonance spectrum (with high resolution) of single microscopic magnetic structures in remanence. We then proceed to explain in great detail how we developed a new experimental technique which fulfills our requirements.
In Chapter 3 we benchmark our new technique on the uniform precession of a thin magnetic film. This uniform precession is frequently used to determine material parameters. Should we be able to accurately measure the resonance spectrum, our technique could be used to determine these parameters for micron-scale elements.
We come to the main objective of this thesis in Chapter 4. Here we study a specific type of excitation in thin magnetic discs, the «*radial spinwaves*». We will examine the effect of the aspect ratio on the position of the resonance frequency of these modes and compare the results with theoretical predictions and micromagnetic simulations. It it will also be shown that we can push these modes into a nonlinear regime by increasing the strength of the

excitation. Micromagnetic simulations indicate that self focussing of spin-waves takes place at these excitation levels.

Chapter 1

Introduction

In this chapter we will briefly review the history of magnetism and also take a look at its microscopic origin. We also investigate magnetism on the microscopic scale («*micromagnetics*»), which is described by the Landau-Lifschitz-Gilbert equation.

1.1 A brief history of magnetism

Magnetism is a phenomenon that has been known about since ancient times and for as long, it has had a significant impact on technology and society. It was introduced into Western thinking by Thales of Miletus (⋆624, †546 BC), through his discussion of the «*lodestone*»[1]. He attributed a soul to this mineral, as it had to power to attract iron[1].

The first practical use of magnetism was made in ancient China around the start of our calendar. At this time a spoon made from lodestone was used to indicate the south. A practical compass was only developed thousand years later by Zheng Gongliang (⋆1031, †1095), to be reinvented in the Western world about a century later.

What followed were several centuries of mysticism and pseudo-science surrounding magnetism, with magnets still being attributed souls, applied to cure diseases (with little result) and the perpetuum mobile (a blooming field of study until this day). The only serious contributions were by William Gilbert (⋆1544, †1603), attributing the working of a compass to the

[1] A lodestone is a piece of magnetised magnetite, Fe_3O_4.

magnetic field of the earth itself, and Daniel Bernouilli (⋆1700, †1782) developing the horseshoe magnet.
It was not until 1820 that real scientific progress was made, this time by Hans-Christian Ørsted (⋆1777, †1851). Discovering that current flowing through a wire can influence the needle of a compass, he made the first connection between electricity and magnetism. André-Marie Ampère (⋆1775, †1836) expanded on this by showing that a current carrying coil acts as a magnet. In 1831 Michael Faraday(⋆1791, †1867) then discovered the law of induction, stating that a changing magnetic field can induce an electric potential. Together with Ampère's law, this made possible the unification of electricity and magnetism by James Clerk Maxwell (⋆1831, †1879) in 1864, giving us Maxwell's equations:

$$\nabla \cdot \mathbf{E} = \frac{\rho}{\epsilon_0}, \tag{1.1a}$$

$$\nabla \cdot \mathbf{B} = 0, \tag{1.1b}$$

$$\nabla \times \mathbf{E} = -\frac{\partial \mathbf{B}}{\partial t}, \tag{1.1c}$$

$$\nabla \times \mathbf{B} = \mu_0 \left(\mathbf{J} + \epsilon_0 \frac{\partial \mathbf{E}}{\partial t} \right). \tag{1.1d}$$

Despite all this progress it was still unclear why materials possessed spontaneous magnetism or could increase the field strength of an electromagnet. Not until the advent of quantum mechanics shed some light on this topic. After the discovery electron spin, Werner Heisenberg(⋆1901, †1976) postulated in 1929 that the Pauli principle is responsible for orienting the spins in a magnetic material through what is now known as the exchange mechanism. The Schrödinger equation for the electrons in a material would have a term added to its Hamiltonian:

$$\hat{\mathcal{H}}_{\text{exch}} = -2\mathcal{J}\hat{\mathbf{S}}_i \cdot \hat{\mathbf{S}}_j, \tag{1.2}$$

where $\hat{\mathbf{S}}_i$ and $\hat{\mathbf{S}}_j$ are the total electron spin of two neighbouring atoms. $\mathcal{J}$ is the strength of the exchange interaction, which can also be negative, leading to ferrimagnetism or antiferromagnetism.
Parallel to the scientific research, magnetism was also being applied in new technologies such as electric motors, generators and transformers. Today, scientific research and technological progress go hand in hand, as new scientific discoveries (NdFeB permanent magnets; Giant Magneto Resistance,

Tunnel Magneto Resistance, both used in hard drive read heads) are rapidly taken up by the technological community. This is especially true for data storage, where magnetic storage has dominated for decades.

1.2 Static magnetism

Before proceeding towards the underlying quantum mechanics of magnetism, it is necessary to review several concepts of classical magnetism.

When a ferromagnetic material is subjected to an external field, the microscopic dipoles start aligning with this field. This is the basic concept behind the working of an electromagnet. This entails that the total current $\mathbf{J}$ in Eqn. (1.1d) obtains a contribution from the sum of all the virtual currents responsible for the magnetic dipoles of the material, $\mathbf{J}_M$[2]. This is related to the macroscopic magnetisation $\mathbf{M}$ (defined as the net dipole moment of the material per unit volume) by $\mathbf{J}_M = \nabla \times \mathbf{M}$.

The external current $\mathbf{J}_{ext}$ (e.g. current flowing through a wire) induces an auxiliary field $\mathbf{H} = \nabla \times \mathbf{J}_{ext}$, responsible for the alignment. Combining these two contributions to the total current, by making use of Eqn. (1.1d) we arrive at:

$$\mathbf{B} = \mu_0 (\mathbf{M} + \mathbf{H}) . \tag{1.3}$$

This is illustrated in Fig. 1.1 for a simple bar magnet. When no external field is present, i.e. no currents flowing, the auxiliary field $\mathbf{H}$ outside of the magnetic material is called the stray field. Internally to the material, it is called the demagnetising field because of the orientation with respect to the magnetisation.

In this work we will typically use the term $\mathbf{B}_{ext} = \mu_0 \mathbf{H}_{ext}$ and Tesla as the unit for external fields.

When the external field is increased, the number of aligned dipoles increases as well. This does not need to happen in a linear fashion, but is typically characterised by hysteresis, such as shown in Fig. 1.2.

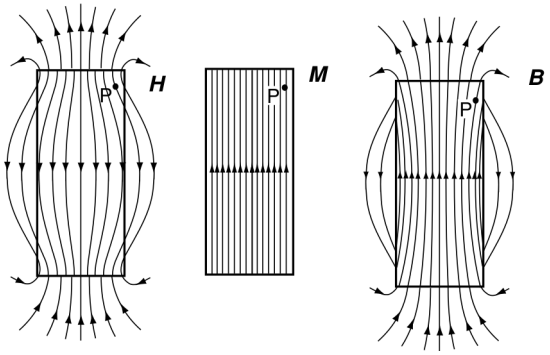

Figure 1.1: The field lines corresponding to **H**, **M** and **B** are shown for a bar magnet. Reproduced from [3].

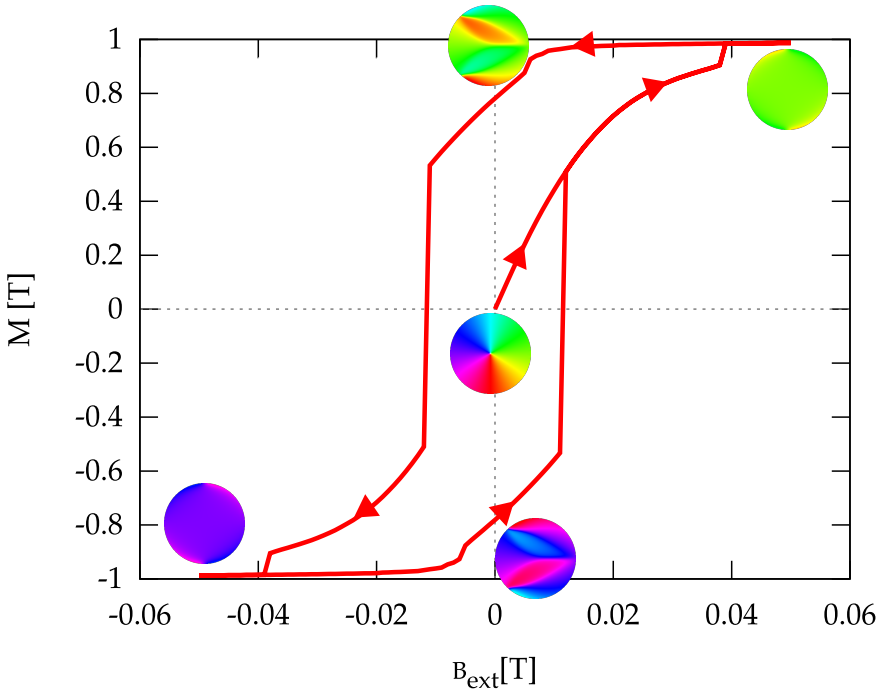

Figure 1.2: A hysteresis loop of a 1 µm diameter Permalloy disc(30 nm thick), with an in-plane external field. The images show the configuration of the magnetisation, the colour code of which can be found on p.11.

When the maximum number of dipoles of the material are aligned, the saturation state is reached and $|\mathbf{M}| = M_S$, the saturation magnetisation.

1.3 Origin of Magnetism

1.3.1 Origin of the exchange energy

We can start our discussion about the quantum mechanical origin of magnetism by looking at the excited states of helium. This two electron system has a wave function $|\Psi\rangle$ and a Hamiltonian:

$$\hat{\mathcal{H}} = \underbrace{\frac{\hat{\mathbf{p}}_1^2}{2m_e} + \frac{\hat{\mathbf{p}}_2^2}{2m_e} - \frac{2e^2}{4\pi\epsilon_0|\mathbf{r}_1|} - \frac{2e^2}{4\pi\epsilon_0|\mathbf{r}_2|}}_{\hat{\mathcal{H}}_0} + \underbrace{\frac{e^2}{4\pi\epsilon_0|\mathbf{r}_1 - \mathbf{r}_2|}}_{\hat{\mathcal{H}}_{ee}} \tag{1.4}$$

As indicated, the Hamiltonian can be split into two parts: the first part is the interaction of the electrons with the nucleus, $\hat{\mathcal{H}}_0$. The second part is the electron-electron interaction, $\hat{\mathcal{H}}_{ee}$, which complicates matters substantially. The ground state of helium has the two electrons both in the 1s orbital. Pauli's principle requires however that the total wave function be anti-symmetric. Therefore the electrons have to have opposite spin:

$$|\Psi\rangle = (\phi_{1s}(\mathbf{r}_1)\phi_{1s}(\mathbf{r}_2))\,\frac{|\uparrow,\downarrow\rangle - |\downarrow,\uparrow\rangle}{\sqrt{2}}, \tag{1.5}$$

the first factor being the spatial wave function, the second the spin part. This wave function is a solution of

$$\hat{\mathcal{H}}_0\,|\Psi\rangle = E_0\,|\Psi\rangle\,, \tag{1.6}$$

and neglects the electron-electron interaction, $\hat{\mathcal{H}}_{ee}$, which we will treat as a perturbation.
For the first excited state we have two possible spatial wave functions:

$$\phi_{sym} = \frac{\phi_{2s}(\mathbf{r}_1)\phi_{1s}(\mathbf{r}_2) + \phi_{2s}(\mathbf{r}_2)\phi_{1s}(\mathbf{r}_1)}{\sqrt{2}}, \tag{1.7}$$

$$\phi_{asym} = \frac{\phi_{2s}(\mathbf{r}_1)\phi_{1s}(\mathbf{r}_2) - \phi_{2s}(\mathbf{r}_2)\phi_{1s}(\mathbf{r}_1)}{\sqrt{2}}. \tag{1.8}$$

In this way, we can also form two total wave functions, taking into account the spin of the electrons:

$$|\Psi_S\rangle = \phi_{sym}\,(|\uparrow,\downarrow\rangle - |\downarrow,\uparrow\rangle)\,, \tag{1.9}$$

$$|\Psi_T\rangle = \phi_{asym}\left(|\uparrow,\uparrow\rangle \text{ or } |\downarrow,\downarrow\rangle \text{ or } \frac{(|\uparrow,\downarrow\rangle + |\downarrow,\uparrow\rangle)}{\sqrt{2}}\right). \tag{1.10}$$

The first wave function is the singlet state, the second are the triplet states. We can now evaluate the energy values associated with these states. For $\hat{\mathcal{H}}_0$ we find that

$$E_0 = \langle \Psi_S | \hat{\mathcal{H}}_0 | \Psi_S \rangle = \langle \Psi_T | \hat{\mathcal{H}}_0 | \Psi_T \rangle = E_{1s} + E_{2s}, \tag{1.11}$$

where

$$\hat{\mathcal{H}}_0 | \phi_{1s} \rangle = E_{1s} | \phi_{1s} \rangle \text{ and } \hat{\mathcal{H}}_0 | \phi_{2s} \rangle = E_{2s} | \phi_{2s} \rangle . \tag{1.12}$$

For the interaction Hamiltonian $\hat{\mathcal{H}}_{ee}$ we find on the other hand that

$$E^S_{ee} = \langle \Psi_S | \hat{\mathcal{H}}_{ee} | \Psi_S \rangle = I + J, \tag{1.13}$$

$$E^T_{ee} = \langle \Psi_T | \hat{\mathcal{H}}_{ee} | \Psi_T \rangle = I - J, \tag{1.14}$$

where

$$I = \int\int |\phi_{1s}(\mathbf{r}_1)|^2 \frac{e^2}{4\pi\epsilon_0 |\mathbf{r}_1 - \mathbf{r}_2|} |\phi_{2s}(\mathbf{r}_2)|^2 \, d\mathbf{r}_1 d\mathbf{r}_2, \tag{1.15}$$

$$J = \int\int \phi_{1s}(\mathbf{r}_1)\phi_{2s}(\mathbf{r}_2) \frac{e^2}{4\pi\epsilon_0 |\mathbf{r}_1 - \mathbf{r}_2|} \phi^*_{1s}(\mathbf{r}_2)\phi^*_{2s}(\mathbf{r}_1) d\mathbf{r}_1 d\mathbf{r}_2. \tag{1.16}$$

The first integral I is called the Coulomb integral and represents the repulsion between the two electron probability densities. The second integral is the exchange integral and is related to the energy when two electrons are exchanged. Because of this term the singlet level has a higher energy than the triplet level, given by $E_S = E_T + 2J$. Thus, despite the absence of any spin-related term in the Hamiltonian, the required anti-symmetry and consequential exchange energy result in alignment of the spins (resulting in a triplet state) at the first excited level.
The same reasoning can be applied to molecular bindings as well, but for a detailed discussion the reader is referred to Stöhr & Siegmann[4].

1.3.2 Ferromagnetic metals

For metals the situation is much more complicated than for the helium atom. The electrons are not completely localised but are subjected to a periodic potential, besides the electron-electron interaction. Instead of discrete energy levels, we arrive at a situation where the electrons can have any energy within an energy band. The number of electrons allowed for each energy is then given by the density of states (DOS). The DOS is then filled

up with electrons up to the Fermi energy level. This is illustrated for both Fe and Cu in Fig. 1.3.

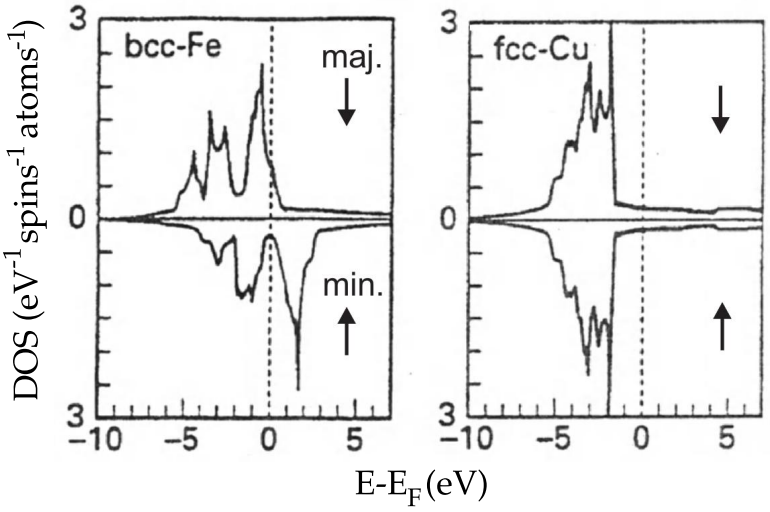

Figure 1.3: The density of states for Fe and Cu, showing the filling up to the Fermi level. For Fe the bands are split in energy by their spin orientation, and this is due to the exchange interaction. Reproduced from [5].

The difference is that the DOS for Fe is split by the two possible spin orientations by the exchange interaction. Because of this splitting, the number of spin-↓ electrons is higher (thus called the majority carrier) than the number of spin-↑ electrons. This results in a net magnetisation, anti-parallel to the spin-↓ electrons (taking into account the negative magnetic dipole of the electron).
This unequal filling has a number of consequences. For example for conduction, scattering of minority electrons is more likely than for majority carriers due to more vacant states being available for the former. Therefore, the resistance will differ for both carriers. Another consequence is the appearance of optical activity related to the local magnetisation, such as X-Ray Magnetic Dichroism, Magneto-Optical Kerr Effect, etc.[4, 3]

1.4 Micromagnetics

On the atomic level, the exchange interaction forces alignment of the spins of nearby atoms. It is only when we look at larger length scales (typically

nanometre length scale) that magnetic structure is introduced. This area of research is called micromagnetism.

1.4.1 Introduction

Micromagnetics is the study of magnetism at the microscopic level, with typical length scales between 10 nm and 100 µm. The dynamics of the local magnetisation $\mathbf{M}(\mathbf{r}, t)$ can then be described by the Landau-Liftshitz-Gilbert equation, illustrated in Fig. 1.4:

$$\frac{d\mathbf{M}}{dt} = \underbrace{\gamma\mu_0 \mathbf{M} \times \mathbf{H}_{\text{eff}}}_{\text{precession}} - \underbrace{\frac{\alpha}{M_S}\mathbf{M} \times \frac{d\mathbf{M}}{dt}}_{\text{damping}}, \tag{1.17}$$

where γ is the gyromagnetic ratio for the electron, and $\gamma\mu_0 = 28\,\text{GHz/T}$. α is a dimensionless parameter which indicates the damping. For materials such as Fe and Ni this is typically in the order of 0.01, but for Yttrium Iron Garnet (YIG) this can be as low as 0.0001.
$\mathbf{H}_{\text{eff}}(\mathbf{r}, t)$ is the local, effective magnetic field and carries contributions from several factors.

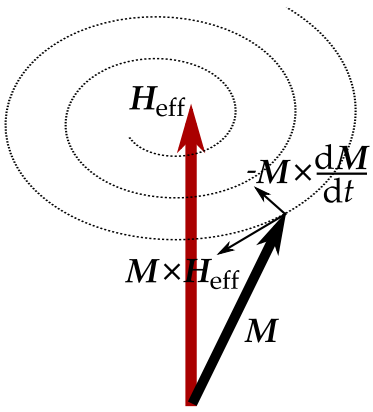

Figure 1.4: The Landau-Lifshitz-Gilbert equation graphically represented. We can discern between a precession term and a damping term. Prefactors have been omitted.

These contributions are[6]:

- **Zeeman field** is the contribution from an external field, for example

the high frequency oscillating field used for exciting a sample. Typically the Zeeman field is indicated as $\mathbf{H}_{\text{ext}}$.

- **Exchange field**, $\mathbf{H}_{\text{exch}}$, which is the largest contribution on short length scales. This forces neighbouring spins to align parallel to each other. It can be shown that the resulting field is given by:

$$\mathbf{H}_{\text{exch}} = l_{\text{exch}}^2 \nabla^2 \mathbf{M}, \tag{1.18}$$

  where l_{exch} is the material dependent constant called the exchange length. For Fe, l_{exch} =3.4 nm and for Ni, l_{exch} =7.7 nm.

- **Demagnetisation field**, also called magnetostatic field, $\mathbf{H}_{\text{demag}}$, is the field created by each magnetic dipole in the material. Because this is the stray field created by each dipole, it also encompasses the dipole-dipole interaction in the material. It acts over a large length scale in comparison with the exchange, and in contrast to the exchange, it tries to orient the spins anti parallel, so as to minimise the stray magnetic field.

  In the absence of external fields and anisotropy, any variations smaller than l_{exch} would have to overcome the energy barrier created by the exchange interaction, which is stronger than the $\mathbf{H}_{\text{demag}}$. Thus l_{exch} sets a lower bound on the size of variations of magnetisation. On larger length scales, the exchange interaction becomes negligible and demagnetisation interaction becomes dominant.

- **Anisotropy field** is a material dependent field that forces the magnetisation to lie along one or more preferred directions, and finds its origin in the coupling between spin and orbital angular momentum. The latter is locked to the crystal lattice, thus establishing one or more axes of anisotropy. Soft magnetic materials are defined as having no or very little anisotropy, in contrast to hard magnetic materials. In this work, we have only studied soft magnetic materials.

These are the most common contributions to the effective field and the LLG equation. However, many other terms can be included as well, to account for Spin Transfer Torque[7], Dzyaloshinskii-Moriya interaction[8], ...
To solve the LLG equation, we made use of the in-house developed software package mumax3[9]. This divides the geometry into a number of

rectangular cells, each with a specific magnetisation vector. It is thus a Finite Difference Method.
In this work, we only used Permalloy (20% Fe, 80% Ni) as magnetic material, which is a soft magnetic material with a typical M_S of 860 kA/m (1.08 T). We used this material because it is also virtually absent of any sources of anisotropy.

1.4.2 Magnetic systems at the microscopic level

A macroscopic sample of Permalloy will, in the absence of any external magnetic field, have no net magnetisation. However, as we start looking at smaller scales, we can discern discrete domains of uniform magnetisation. When averaging out to the macroscopic level, these domains yield no net result. Because of the absence of anisotropy, the largest field on the macroscopic level is the demagnetisation. For a thin film, $|H_{demag}| \approx M_S$ when the magnetisation tilts out-of-plane. Therefore the magnetisation will remain in-plane, unless some excitation forces it. The demagnetisation field also forces the magnetic material to structure itself so that there is almost no stray field. This collapse of (macroscopic) order is only halted by the exchange interaction, setting the lower limit on structure variations.
For structures where the exchange interaction is stronger than the dipole-dipole interaction, the result is a single domain structure. Two examples, shown in Fig. 1.5, are the S-state and C-state.

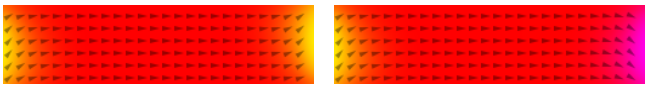

Figure 1.5: The magnetic ground states of a $500 \times 125 \times 3\,nm^3$ Permalloy rectangle. The arrows indicate the local direction of the magnetisation which is also represented by the colour code. The colour definition is shown in Fig. 1.6.

For somewhat larger[2] structures, the dipole-dipole interaction can force flux closure, resulting in a negligible net magnetisation. Examples of this are the Landau- and vortex-states shown in Fig. 1.6. Our work will focus on

[2]Larger in the sense of larger aspect ratio between lateral dimensions and thickness

the latter. These vortex states have a curled up magnetisation, eliminating any stray fields, except near the centre. But on these short length scales the exchange interaction starts to dominate, and the magnetisation is forced to turn completely out-of-plane. Therefore, the out-of-plane vortex core will have a diameter in the range of the exchange length.

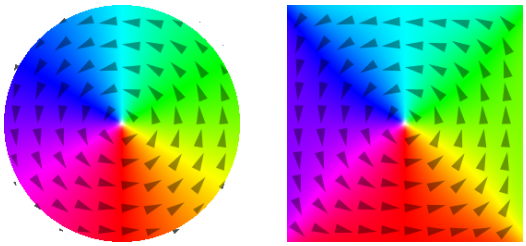

Vortex state Landau state

Figure 1.6: The magnetic ground states of both a square and circle of $500 \times 500 \times 30\,\mathrm{nm}^3$ Permalloy. This also introduces the colour code for the magnetisation direction (indicated by the arrows), note that white equals positive out-of-plane and black negative out-of-plane.

The last topic we need to address in this introduction are spin waves, which are excitations of the magnetic system. Consider for example a chain of spins, all pointing in the same direction. Inverting the spin of a single element would require an energy of $4\mathcal{J}S^2$ according to the Heisenberg model. If this would be the lowest excitation, the spin wave dispersion spectrum would show an energy gap at the origin. It can be shown that because of this, these excitations can not occur at room temperature. However, it is known that they in fact do exist. This can be understood if the spin flip is shared between several elements, as shown in Fig. 1.7.

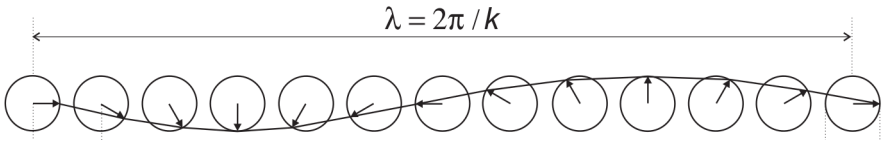

Figure 1.7: A sketch of a spin-flip distributed among several atoms. Reproduced from [4].

If ϵ is the angle between the magnetisation of each atom in the chain, it can be shown that for the N atoms sharing the spin flip, the energy of the

system is increased by[4]

$$\Delta E = N\mathcal{J}S^2\epsilon^2, \tag{1.19}$$

where ϵ is the angle between two neighbouring spins. Because this dispersion relation does not feature an energy gap, thermal excitations are possible.

The excitation source needs not to be thermal, but can be an external magnetic field or optical excitation. An example of a spin wave induced by an external field is shown in Fig. 1.8. Here a strip of Permalloy of 500×125 nm wide and 3 nm thick is saturated along its length by an external field of 1 T. Superimposed on this field is an oscillating field (of 35 GHz and 10 mT) along the width of the strip. This generates spin waves that propagate along the length of the strip. But because of the relatively high damping of Permalloy, these spin waves do not propagate very far.

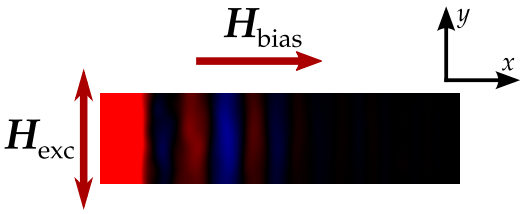

Figure 1.8: An illustration of a spin wave in a 500×125 nm wide strip, 3 nm thick. The strip is saturated along the x-axis by a 1 T external field and excited with a 35 GHz, 10 mT oscillating field along y-axis in the brightly coloured red area. The spin wave is shown as variations in m_z, which propagate along the x-axis. Red indicates positive out-of-plane, blue negative out-of-plane magnetisation.

We can discern three types of spin waves:

- Magnetostatic Surface Spin Waves (MSSW) or Damon-Eshbach modes, where the wave vector is orthogonal to the magnetisation, and both lie in-plane;
- Backward Volume Magnetostatic Spin Waves (BVMSW), where the wave vector is parallel to the magnetisation, and both lie in-plane;
- Forward Volume Magnetostatic Spin Waves (FVMSW), again wave vector and magnetisation are orthogonal, but in this case the wave vector lies in plane but the magnetisation tilts out-of-plane.

The field of magnonics is dedicated to all possible forms in numerous geometries and lattices[10], but in this work we will focus on the MSSW type. An example of a dispersion relation for these spin waves for a thin film is shown in Fig. 1.9. Note that this diagram is only valid for wavelengths that are much longer than the exchange length, i.e. they are still on the length scale where the dipole-dipole interaction dominates.
These waves can also be confined in a specific geometry, which will lead to quantisation. In the case of magnetostatic spin waves, the edges will form the dominant boundary condition. The dynamics can occur at these edges, leading to what is named «*edge modes*» for obvious reasons, with the bulk of the element remaining static. In other cases, the edge can remain fixed and only in the bulk does the magnetisation show some dynamic behaviour. These are called bulk modes.
In contrast to the motion of a drum, or the electric field in a cavity, the boundary conditions for confined spin waves are not that strict. For example, for the radial spin waves we have studied, the bulk volume shows dynamics, though the edges are partially pinned.

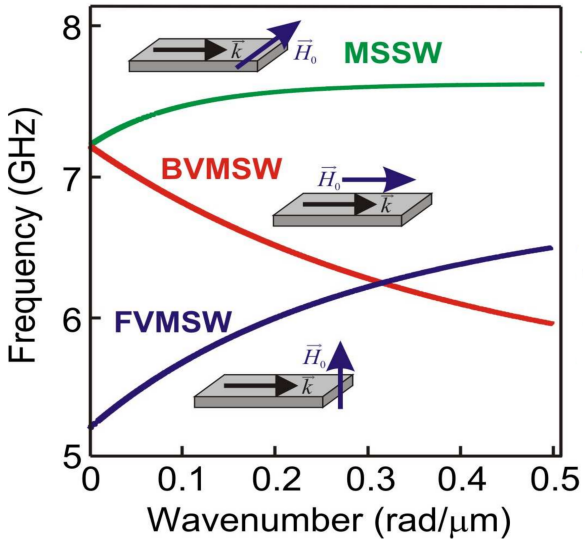

Figure 1.9: A possible dispersion spectrum for the three types of spin waves for a uniformly magnetised thin film. Reproduced from [11]

Chapter 2

Experimental methods

We start with an overview of methods available to the experimenter for investigating nano-scale magnetisation dynamics and discuss the advantages and disadvantages. Methods only applicable to macroscopic samples (e.g. cavity FMR) have been omitted. A great deal of attention will go to the Time Resolved Scanning Transmission X-ray Microscopy (TR-STXM) and stripline FMR as these methods have been used in this work.
Each of the existing methods is optimised for a specific problem, however we find that a certain approach is missing. We will explain in great detail how we came to a solution for this niche problem and discuss the caveats that have been encountered and its advantages and disadvantages. The main results of this work have been published in Ref. [12].

2.1 Introduction

In the field of nano-scale magnetism one tries to observe the dynamics both at the nanometre length scale and picosecond time scale. This poses numerous technical challenges, as not only is the signal very small, but the time scale very short. Noise can easily surpass the magnetic signal in magnitude and mask any dynamics.
We can make two orthogonal divisions among the different methods, the first being in the detection mechanism: optical (including X-rays) or electrical. The second division is in the measurement domain: frequency or temporal.

2.1.1 Optical detection methods

Optical methods rely on the interaction of light with the electrons of the sample under study. One such interaction is the Magneto-Optical Kerr Effect where the polarisation of linearly polarised light, reflected of a ferromagnetic sample is slightly rotated depending on the magnetisation.
Time Resolved Magneto-Optical Kerr Effect Microscopy (TR-MOKE) makes use of exactly this effect[13]. Typically a mode-locked Ti:Sapphire laser produces a train of light pulses that are tens of femtoseconds long[14].
These light pulses have to be synchronised with the magnetisation, as illustrated in Fig. 2.1. Because the sample is illuminated at the same point in time (i.e. phase) of its dynamics, the time averaged value of the reflected light will have gained a static rotation of the polarisation.

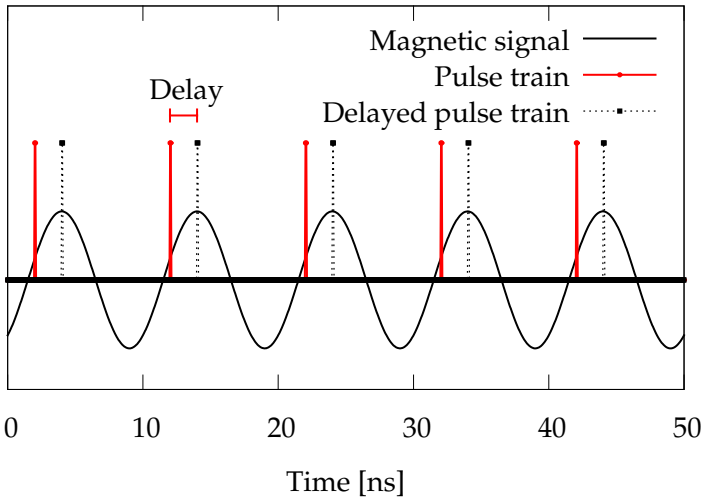

Figure 2.1: The timing of a TR-MOKE experiment. A train of very short light pulses are phase locked to the magnetic signal that is being studied. Because these pulses always illuminate the sample at the same phase of the dynamics, the time averaged rotation of polarisation (of the reflected light) is proportional to the magnetisation at this point. By shifting the arrival time, e.g. by elongating the optical path, different points of the magnetisation can be studied.

The repetition frequency of the laser is in the order of 100 MHz for most systems, and only magnetisation dynamics at a multiple of this frequency can be measured. This forms a limit on the frequency resolution obtainable

by TR-MOKE experiments. In light of a discussion that will follow later, it is interesting to view this as a «*mixing process*». At very high frequency two signals, the illumination and the magnetisation, are mixed (i.e. multiplied) together, producing a signal at much lower frequency (DC in the case for TR-MOKE). For TR-MOKE this mixing takes place at the sample and is an optical process.
Though TR-MOKE is suited to study transient behaviour, which requires a time domain method, the amount of frequency domain information it can yield is limited. The frequency resolution obtainable depends on the damping parameter of the sample. If the system is excited using a continuous sine wave, this is not a limiting factor, but with pulsed excitation the oscillations can damp quite quickly.
The second optical probing method is Brillouin Light Scattering Microscopy (BLS)[15]. This method makes use of the fact that photons that scatter inelastically of magnons, will have transfered a small amount of energy and momentum. This entails that the wavelength of the photon will have shifted slightly (up or down). In order to resolve these photons from the majority of elastically scattered photons, a spectrometer with a high resolution and sensitivity is necessary. Only by using a Tandem-Fabry-Perot Interferometer is it possible to detect the frequency shift of the inelastically scattered photons. Such a set up has an extra ordinary sensitivity, being able to even detect thermal magnons. The method measures directly in frequency domain, but has the added advantage of wavevector selectivity, due to conservation laws dictating that only magnons with in-plane momentum $\mathbf{k} = (2h/\lambda)\sin\theta$ (with λ the wavelength of the incoming photon, h Plank's constant and θ the angle of incidence) can inelastically scatter photons.
Both of the above methods have a high sensitivity and the ability to produce high quality measurements in either the frequency or temporal domain, but they have significant drawbacks as well. Besides the high initial cost, both require proper alignment and maintenance of the many components in the optical path.

2.1.2 Electrical detection methods

The second method of detection uses electromagnetic coupling between the sample and an antenna. Again, we can make a distinction between

time domain and frequency domain methods.

Pulsed Inductive Microwave Magnetometry (PIMM) is the main method for investigating transient behaviour[16, 17]. First the magnetic system is excited using a magnetic pulse, generated by passing a current through a nearby conductor, leaving the magnetic sample to perform its relaxation oscillation to equilibrium. The precession of the magnetisation then induces an alternating voltage in a nearby antenna, due to Faraday's law of induction. After amplification, this voltage can be sampled using an oscilloscope with a high bandwidth. Unlike the previous optical methods, the method requires a massive array of nano-elements to obtain sufficient signal.

Such arrays consist of many elements, which all can vary a small amount in size and position. The signal of each of those elements will average out, leading to extrinsic line broadening.

To probe in the frequency domain we could employ a Vector Network Analyser (VNA), to set up a VNA-FMR experiment[18, 19]. Here one uses a sine wave excitation at a number of frequencies and measures the magnitude and phase of both the reflected and transmitted signal. Again, to have a signal of sufficient strength, single elements are not enough and entire arrays, measured simultaneously, are required. Even then one needs a VNA that can resolve very small variations on top of a very large baseline. This is due to the fact that electrical effects (from parasitic capacitance and inductances) can surpass the magnetic effect by orders of magnitude.

PIMM and VNA-FMR have the disadvantage that they need to measure entire arrays at once, in contrast to the optical methods, which probe single elements. Both electrical methods are also sensitive to pure electrical effects, thus requiring baseline corrections.

It is also possible to use effects such as anisotropic magnetoresistance (AMR), giant magnetoresistance (GMR), etc. to detect magnetisation dynamics. For example, Goto *et al.* have used AMR to detect vortex gyration[20]. To employ such an effect, sample preparation becomes more complicated because of additional microscopic contacts and special layers that are required.

In conclusion, optical methods have the advantage of highest sensitivity, but come with a high complexity and maintenance. The electrical methods are easier to set up, but lack the sensitivity and require large arrays of nano elements. None of the above methods have been employed during this work, but a hybrid method was developed as will be discussed later in this

chapter.

2.2 Scanning Transmission X-ray Microscopy

In the past, the research in our group has mainly focussed on work using Time Resolved Scanning Transmission X-ray Microscopy (STXM) using in-house developed acquisition hard- and software at the Maxymus Endstation of the Bessy II synchrotron in Berlin[21, 22, 23, 24].

STXM uses a monochromatic, circularly polarised X-ray beam which is focussed onto the sample. The sample is then scanned under this spot and the intensity of the transmitted beam that passes through is recorded for each position.

2.2.1 X-ray microscope

The X-ray beam is produced at the synchrotron. This is a circular particle accelerator, specifically designed for X-ray production. In such an accelerator, electrons are accelerated to near the speed of light, so their kinetic energy is several orders of magnitude more than their rest mass. When they are deflected, at points such as bending magnets, they produce X-ray under the form of «*Bremsstrahlung*».

Though radiation is emitted at the bending magnets, the intensity is relatively low. To increase the light intensity, the electrons can be deflected in a higher strength magnetic field with periodically inverting polarisation. This is called either an undulator or a wiggler, depending on the output spectrum of the light. Several features of the Bessy II synchrotron and undulator used, are summarised in Table 2.1.

Table 2.1: Several key features of the Bessy II synchrotron and undulator used for the STXM experiments presented in this work. Data from [25].

Bessy II synchrotron & UE46 undulator	
Electron energy:	1.7 GeV
Typical current:	300 mA
Circulation frequency:	499.665 MHz
# of Buckets:	400
Typical pulse width:	$\approx$ 70 ps
Undulator energy range:	150 eV - 1900 eV
Undulator photon intensity:	10^{13} photons/s/100 mA

An overview of the X-ray optics, from undulator to detector, is shown in Fig. 2.2.

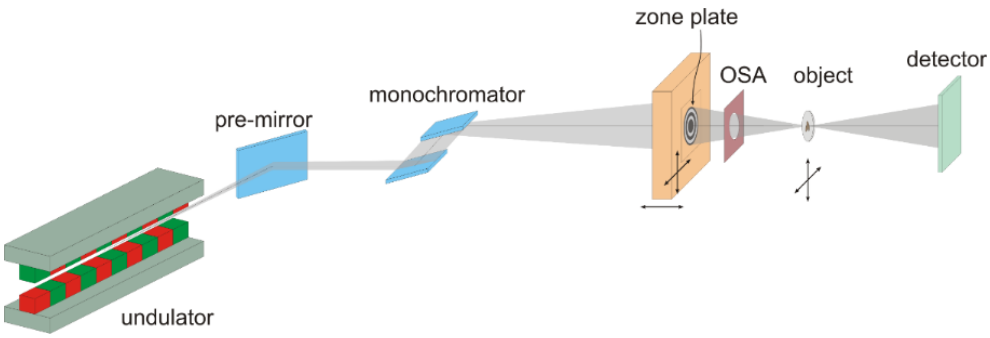

Figure 2.2: An overview of the X-ray optics used in a scanning X-ray microscope. Reproduced from [26].

The deflection of electrons in an undulator yields radiation with a wide range of energies (of the order of 100 eV) and several harmonics, which is not directly usable for our type of studies, thus a monochromator selects a narrow range from the spectrum. Afterwards the beam is focussed onto the sample through a diffracting Fresnel zone plate, as refractive lenses do not exist for soft X-rays. A photograph of the actual microscope is shown in Fig. 2.3.

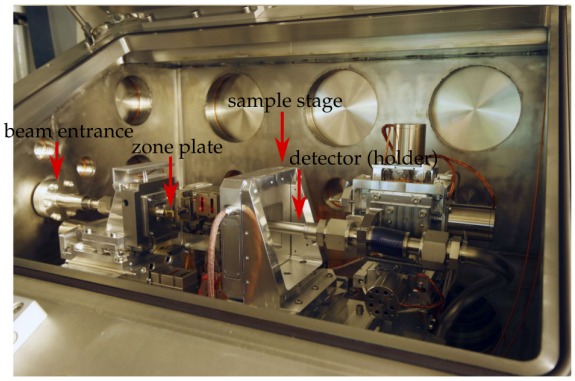

Figure 2.3: A photograph of the Maxymus STXM at the Bessy II synchrotron in Berlin, which was used for work in this thesis. The X-rays enter from the left side, and are focussed by the zone plate (mounted on the brass holder). The samples are mounted on the piezo stage at the right. The detector is mounted on a tube and placed right behind the sample, and can be moved by electrical motors.

Using this configuration, it is possible to resolve features down to 25 nm, such as a magnetic vortex as illustrated in Fig. 2.4,[21].

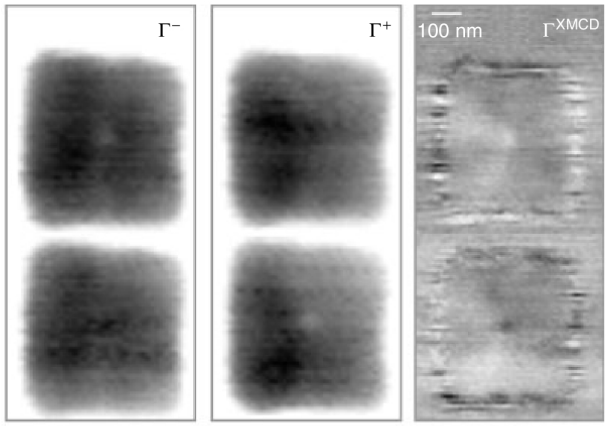

Figure 2.4: STXM microscopy of a 500x500 nm 40 nm thick Permalloy square, showing a vortex core at centre. The two leftmost panels are images from left-handed and right-handed circularly polarised X-rays at the L_3 edge of Ni. The rightmost panel shows the differential image obtained by subtracting the two left images, most clearly showing the two possible vortex core polarisations. Because the beam was oriented perpendicular to the sample only out-of-plane magnetisation is imaged. Reproduced from Ref. [21].

2.2.2 Origin of magnetic contrast

Magnetic contrast is obtained through the X-ray Magnetic Circular Dichroism effect[27, 4]. Because of this effect, the helicity of the incoming beam with respect to the magnetisation direction (parallel or anti-parallel) yields different absorption rates. We denote positive helicity as right-handed polarisation (RCP) and negative helicity as left-handed polarisation (LCP). The origin of XMCD lies in the unequal filling of the density of states as is shown in Fig. 2.5, by electrons with different spin orientation.

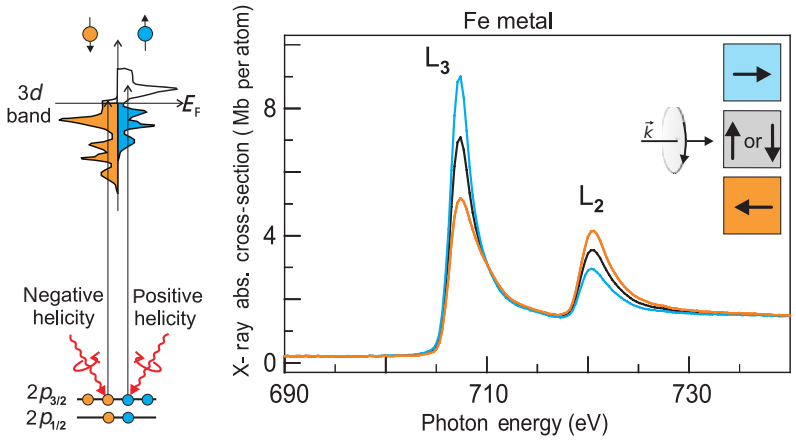

Figure 2.5: The XMCD effect illustrated. As the 3d energy levels of electrons with spin up and down are shifted, the filling of the states differs. This asymmetry yields a different absorption cross section depending on the orientation of the angular momentum of the incoming photon and the magnetisation. Reproduced from Ref. [4].

Electrons from a L_2 ($p_{1/2}$) or a L_3 ($p_{3/2}$) level can be excited to the valence d-band, through the absorption of a photon. The angular momentum carried by the photon is transferred to the angular momentum of the photoelectron, which in turn is transferred to the spin via the spin-orbit coupling. In this way RCP and LCP photons result in photoelectrons with opposite spin. If the magnetisation is parallel to the helicity, RCP photons will yield minority photoelectrons (spin-up) for the L_3 edge, due to the positive spin-orbit coupling term. These have more available states in the valence band, thus the absorption for RCP photons will be larger than for LCP photons (which yield majority photoelectrons). If the magnetisation is reversed,

RCP photons will still yield spin-up electrons, but these are now majority photoelectrons and thus the effect on absorption is inverted. At the L_2 edge, the effect is opposite to the L_3 edge because of an opposite sign in the spin-orbit coupling. At the L_3 edge of Ni (850 eV) the relative change in absorption is approximately 20%[28].

2.2.3 Timing

The electrons in a synchrotron are not continuously distributed along the ring, but are grouped together in bunches. The time between two bunches is about 2 ns, i.e. the emitted X-rays form a pulse train with a repetition frequency of 500MHz and a typical width of 70 ps. The use of a narrow pulses of X-ray photons enables time resolved microscopy if the frequency of the pulse train and the excitation are phase locked, like TR-MOKE measurements.
The timing of the X-ray probe in relation to the magnetisation dynamics is illustrated in Fig. 2.6 for the simple case where there are four probe moments in three periods of the oscillation of the magnetisation.

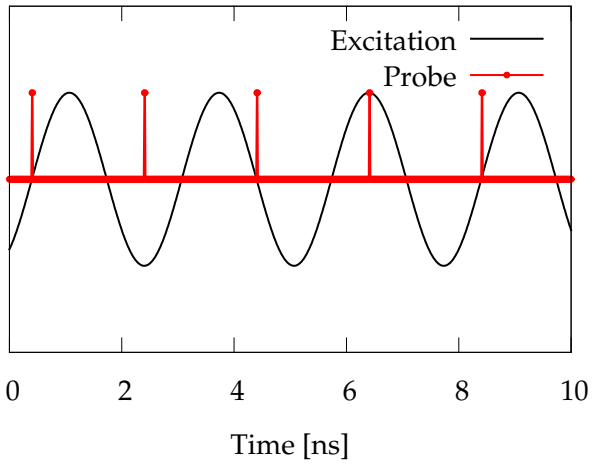

Figure 2.6: The timing diagram for TR-STXM, where in this case the ratio between excitation frequency and probe frequency was $P/C = 3/4$. The arrival of the beam (each 2 ns) probes the system at 4 different phases of the excitation, after which it returns to the original phase.

Phase locking the probe to the excitation implies that each pulse of the repetitive pattern will probe the magnetisation at a specific phase of the

excitation. In general the excitation frequency f will be phase locked to the synchrotron clock (of 500MHz), according to

$$f = \frac{P}{C} \cdot 500\text{MHz}, \tag{2.1}$$

where C is the number of phases that are being probed and P an arbitrary natural number to obtain a frequency in the region of interest.[1]
Because the X-ray bunches continuously illuminate the sample at different phases, the intensity has to be measured for each photon flash and each sample has to be correctly binned into one of the C channels corresponding to a specific phase. This is handled in hardware through the use of an FPGA.
The detection of soft X-rays with good efficiency is done by using an Avalanche Photodiode (APD), because these multiply the number of original photoelectrons and feature bandwidths of up to 1.5 GHz. Photomultipliers have a higher efficiency, but are slower.
APDs exploit the avalanche effect where the initial photoelectron is accelerated in a high electric field and impacts with atoms in the lattice of the crystal. This liberates more electrons, which in turn also undergo acceleration and lead to impact ionisation. Therefore the original photocurrent is multiplied several times. When compared with ordinary photodiodes, APDs have typical gains of 100, due to this internal amplification mechanism. The time required for the avalanche is the limiting factor for the speed, with typical upper values of 250 ps rise time for current Si APDs.

2.2.4 Spectroscopy of magnetic resonances

Though the method described above allows direct imaging of the out-of-plane magnetisation in the time domain, it is time consuming and does not yield direct spectral information. For example to find resonances one can pulse the sample and perform a Fourier transform on the time series. This however, gives a low Signal-to-Noise Ratio (SNR) due to the fact that the energy of the pulse is distributed across a broad portion of the spectrum and the excitation for each resonance is limited thereby.
The alternative is exciting the sample with a sine excitation (continuous wave, CW excitation) and measuring the response. This would yield a

[1] It is important for anti-aliasing purposes that C and P do not share a common factor in their prime decomposition.

stronger signal around the resonance frequency. However, such an approach is not only time consuming, but it does not allow for a fine mazed frequency grid. This would require a large number of channels as follows from Eq. 2.33, and results in a lower SNR due to the spreading of the detected photons over more channels.
The TR-STXM method has been applied in this work to observe the transient behaviour of excitations, but it was deemed necessary to set up a second method to investigate samples for possible resonances before performing TR-STXM measurements.

2.3 Stripline FMR

Initially the effort was undertaken to build a stripline FMR set up, such as depicted in Fig. 2.7. The method resembles cavity FMR, but there are several subtle differences. Firstly, stripline FMR is a broadband method whilst cavity FMR requires a high Q cavity, implying a narrow bandwidth. This translates to a higher signal quality for cavity FMR, but a fixed frequency in contrast to stripline FMR. Secondly, cavity FMR measures reflected power in contrast to transmitted power for stripline FMR.
The main reason for preferring stripline FMR is its broadband nature, where one gathers information (such a linewidth) directly in the frequency domain. Another consequence of the broadband nature is the ability to sweep frequency and not only field as is usually done for cavity FMR. This enables making measurements in remanence or at a specific bias field, which is of importance when the sample has a non uniform ground state.

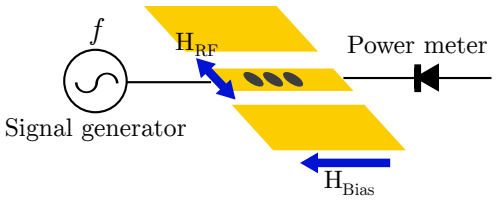

Figure 2.7: The basic layout of a stripline FMR set up. The sample is biased using an external magnetic field (H_{Bias}) and is excited using the magnetic field generated by the current through a coplanar waveguide (H_{RF}). The frequency is then scanned while the power through the sample is measured.

To excite the sample, a high frequency magnetic field needs to be generated. Therefore one needs a broadband microwave waveguide, such as a microstrip line or a coplanar waveguide (CPW), that efficiently transports the microwave power via the sample to the detector. Both examples are planar waveguides as they are formed by a planar geometric structure on top of a suitable substrate. This substrate can have a metallisation on the bottom, which is usually grounded. Microstrip is the most simple of such conductors and consists of a metallic strip of a specific width (signal conductor) on top of a microwave substrate with a bottom metallisation (ground). A CPW consists of a metallic strip (signal conductor) which is separated by two gaps from the rest of the top metallisation which is grounded. The bottom of the substrate can also be metallised and grounded, but this is not required. Both are illustrated in Fig. 2.8.

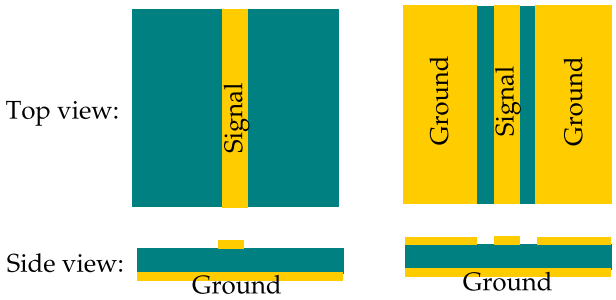

Figure 2.8: An illustration of a microstrip and a (grounded) coplanar waveguide. Yellow indicates metallisation (Au or Cu), blue substrate (Rogers RO4350b or Si).

If the sample under investigation is a metallic film, one has to take care that the sample does not short the signal conductor to ground. This induces strong frequency dependence of transmitted power and can reduce the high frequency current (and thus the magnetic field) that couples to the sample. For macroscopic samples we used microstrip lines, because they are less sensitive to shorting to ground via the sample. Microscopic samples are usually made on a Si or SiN substrate, where the grounded bottom layer is usually absent. This leaves coplanar waveguide as the only option. This has the added advantage that the spacing and width of the CPW can be optimised, not only to result in a flat frequency dependence of the transmission but also a high magnetic field at the sample.

Our stripline FMR set up used a large electromagnet capable of generating fields up to 800 mT in a 10 cm gap and could be calibrated using a NMR field strength probe. Microwave power was generated using a Hittite HMC-T2100 signal generator, producing signals up to 20 GHz and 0.5 W of output power. The microstrip for macroscopic samples was produced on a 0.762 mm thick RO 4350B substrate from Rogers Corp., leading to a width of 1.65 mm. The power detector used was a Point Contact Detector (i.e. diode, 2087-6001-00 from MACOM) with a sensitivity of 500 mV/mW and a noise floor of approximately -45 dBm.

Our samples themselves consisted of thin magnetic films (several tens of nanometers thick) of different materials (Co, Ni, Fe, Permalloy) on a Si substrate with the native oxide still present. We measured the output voltage of the diode detector, while sweeping the frequency of the excitation. At the same time, the sample was biased with a magnetic field. Under these circumstances, the magnetisation of the entire film will precess if the frequency of the excitation matches the resonance frequency of the system for this fieldstrength (see Chapter 3 for a detailed description). At resonance, this process takes up energy and the amount of power transmitted through the sample will drop. However, our measurements did not yield any information directly. Non-magnetic effects were dominant and we needed to correct for these.

The easiest method is switching the magnetic field on and off and comparing both resultant curves. This is shown in Fig. 2.9, where it is difficult to distinguish between noise, systematic effects and the actual magnetic signal. The sample under investigation was a 20 nm thick permalloy film on a 2x10 mm^2 Si substrate.

The result of this type of measurement is in contrast to a measurement at fixed frequency, where the magnetic field is swept. An example for exactly the same sample is shown in Fig. 2.10, where the resonance is now clearly discernible.

However, our interest goes out to microscopic samples and not macroscopic thin films. From this analysis we can induce several things about possible microscopic measurements. Firstly, measuring transmitted power directly will not yield any useful information. Electrical effects will probably swamp the spectrum, as for even a large macroscopic sample, the magnetic signal is a variation of 1% of the detector voltage at resonance, where

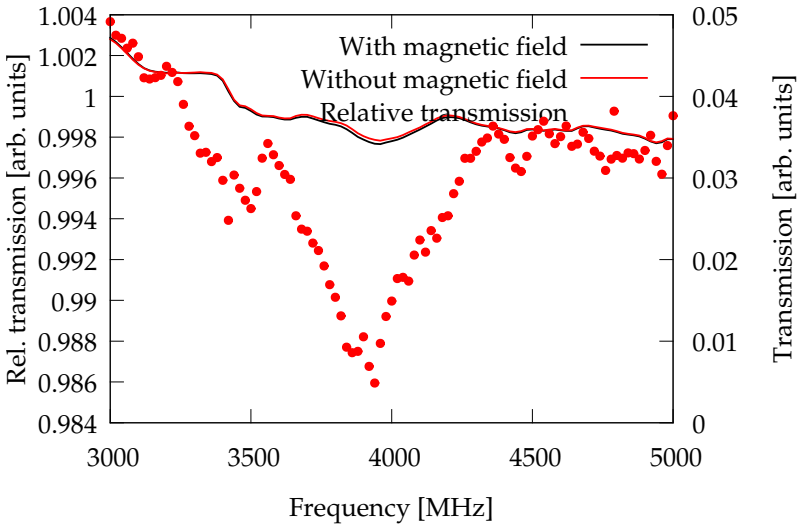

Figure 2.9: A FMR spectrum recorded by measuring the transmitted microwave power through a microstrip with the magnetic field both on and off. The final spectrum is the ratio of transmitted power with the magnet on, to the transmitted power with the magnet off. This is a sample of 2x10 mm^2, 10 nm thick permalloy, biased with 20 mT.

electrical effects can easily show variations of 50% over a comparable frequency range. Thus a method is required to separate magnetic from electrical effects. For experiments performed in remanence, this separation poses quite a challenge. For an optimal SNR, the correction should be performed at a rate of 100Hz or higher as too slow performed corrections can show significant issues with drift. If for example the RF power should drift between measurements, the drift might mask the actual magnetic signal. As a side note, when corrections are done at this rate one can speak of lock-in detection, though lock-in detection usually makes use of small modulations and not large ones such as presented here.

Secondly, we should be able to measure the difference between remanence (i.e. no bias field) and a saturated state, i.e. saturated in-plane or out-of-plane. The former has the advantage that only a small magnetic field is necessary to saturate a thin film in-plane ($\approx$ 5 mT for Permalloy), whilst a field with a strength of the entire demagnetisation field is required to saturate it out-of-plane ($\approx$ 1 T for Permalloy). Depending on the orientation of the exciting magnetic field, either state can have a uniform resonance,

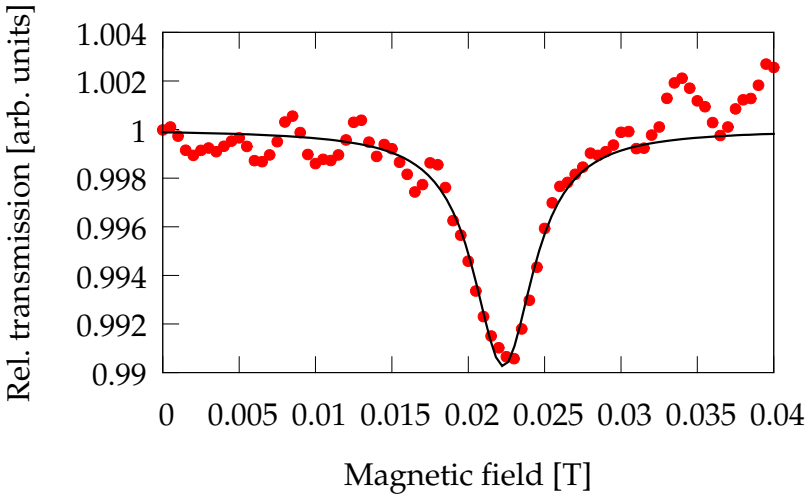

Figure 2.10: A FMR spectrum recorded by measuring the transmitted microwave power through a microstrip at a fixed frequency of 4 GHz and sweeping the magnetic bias field. The resonance is visible at 22.30±0.07 mT with a linewidth of 2.4± 0.2 mT. The same sample as in Fig. 2.9 was used.

leading to a measured spectrum that is the sum of both the magnetic signal one is looking for and a uniform resonance. A feasibility study was performed to analyse the possibility of building a magnet configuration that would generate the necessary magnetic fields. However the strength of the magnetic field needed was too high and varied too rapidly, to be practically obtainable. Thus the simple idea of stripline FMR was abandoned for all but macroscopic samples.

2.4 Magneto-Optical Spectrum Analyser

Optical methods probe the magnetisation directly and do not require extensive baseline corrections. The most well known method is of course TR-MOKE, discussed in Sect. 2.1.

Such an approach has drawbacks when the primary interest is in the frequency domain. Firstly, the pulsed excitation has a high frequency cut-off that is typically lower than achievable with CW excitation. The spectral content of the pulse is also not under the control of the experimenter, with e.g. ringing being a possible issue. The final spectrum is the product of

the spectrum of the excitation and the magnetic system, thus such effects are quite nefarious. Secondly, when a FFT is employed to transform to the frequency domain, the total acquisition time limits the spectral resolution. For example, a 5ns time trace would yield a resolution of 200MHz.
Thus despite being a highly sensitive method, TR-MOKE is more appropriate for transient studies than investigating the spectral domain.

2.4.1 Introduction

We are looking for a way to transform the high frequency magnetisation dynamics in to the low frequency domain. We need some form of frequency mixing process and we can discern two possible solutions:

1. Optical mixing, where the laser used for illumination is modulated near the same frequency of the magnetisation dynamics;

2. Electrical mixing, where the mixing takes place after the conversion to an electric signal by a fast photodiode.

Current technologies allows laser modulation up to several gigahertz for 650 nm light. On the other hand, commercially available photodiodes have bandwidths as high as 12 GHz.
Because we use elements from both VNA-FMR (measurement abilities) and TR-MOKE (underlying physics), our method can be regarded as a hybrid between these two. The basic concept is a polar Kerr set up[2] with a CW laser, but where the polarisation change is detected at high frequency. A high speed photodiode and sensitive receiver is required to this end.

2.4.2 Jones calculus

Before discussing the microscopic nature of the Kerr effect, it is interesting to shortly address what is called Jones calculus, which simplifies calculations involving polarisation states of light.
The polarisation of light can be defined with respect to the plane of incidence (i.e. the plane formed the incoming beam and the normal to the surface), with *s*-polarisation having the electrical field perpendicular (*s* from the German word «*senkrecht*», meaning perpendicular) to this plane and

[2]If one is interested in in-plane magnetisation dynamics, a longitudinal Kerr set up is recommended.

p-polarisation having a polarisation axis lying in this plane (p from parallel). The situation is illustrated in Fig. 2.11, where also the Kerr rotation is shown for an incident s-polarised beam.

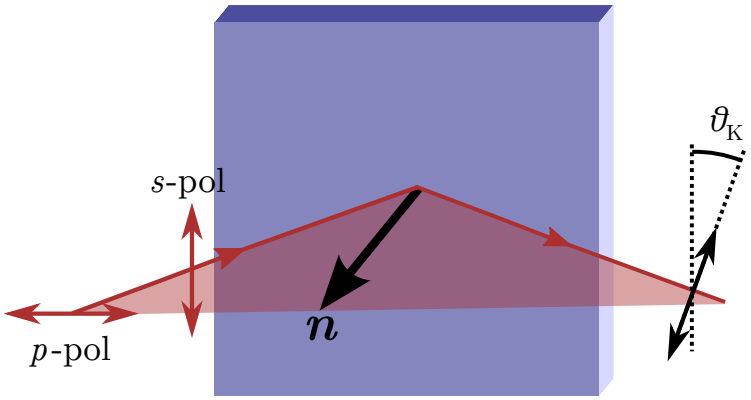

Figure 2.11: Shown is the definition of s and p-polarised light, with $\mathbf{n}$ the unit vector normal to the surface. When (s-)polarised light is reflected of a sample having a definite magnetisation, the polarisation axis will have rotated over an angle θ_K.

The unit vectors along both s and p direction can be taken as basis vectors for the decomposition of the electric field, i.e.

$$\mathbf{E}(t) = \boldsymbol{e}_s E_s \exp(-i\omega t) + \boldsymbol{e}_p E_p \exp(-i\omega t). \tag{2.2}$$

Leaving the exponential evolution implicit, we could write

$$\mathbf{E} = \begin{pmatrix} E_s \\ E_p \end{pmatrix}. \tag{2.3}$$

In this framework s polarised light would correspond with $E_s = 1$ and $E_p = 0$. For linearly polarised light with the polarisation axis 45° between $\boldsymbol{e}_s$ and $\boldsymbol{e}_p$ would correspond with

$$\mathbf{E} = \frac{1}{\sqrt{2}} \begin{pmatrix} 1 \\ 1 \end{pmatrix}, \tag{2.4}$$

taking into account proper normalisation ($E_s^2 + E_p^2 = 1$).
The advantage of this Jones calculus lies in the fact that the action of optical elements modifying the polarisation can be written in the form of matrix

algebra. A polariser with its axis parallel to $\boldsymbol{e}_s$ has a corresponding matrix:

$$\mathcal{P}_s = \begin{pmatrix} 1 & 0 \\ 0 & 0 \end{pmatrix}, \tag{2.5}$$

and the effect on diagonally polarised light being

$$\mathbf{E}' = \mathcal{P}_s \mathbf{E} = \begin{pmatrix} 1/\sqrt{2} \\ 0 \end{pmatrix}, \tag{2.6}$$

thus leaving the intensity ($\propto \mathbf{E}^\dagger \mathbf{E}$) halved, exactly what one would expect from the Malus equation.
Circularly polarised light can also be represented using this notation, as we know that it is the superposition of the two orthogonal linearly polarised states, but with a retardation in phase between the two. In the following we will use the notation and sign convention of [29]. For RCP light, we know that the s-component is delayed by $\pi/2$ radians with respect to the p-component, i.e.

$$\mathbf{E}(t) = \frac{\boldsymbol{e}_s}{\sqrt{2}} \exp(-i\omega t) + \frac{\boldsymbol{e}_p}{\sqrt{2}} \exp(-i(\omega t + \pi/2)). \tag{2.7}$$

From this it follows that we can write that

$$\mathbf{E}_{RCP} = \frac{1}{\sqrt{2}} \begin{pmatrix} 1 \\ -i \end{pmatrix}, \tag{2.8}$$

and by following the same line of reasoning for LCP, we arrive at

$$\mathbf{E}_{LCP} = \frac{1}{\sqrt{2}} \begin{pmatrix} 1 \\ i \end{pmatrix}, \tag{2.9}$$

It is clear that we can invert these equations and regard linearly polarised light as a superposition of both LCP and RCP light, i.e.

$$\mathbf{E}_s = (\mathbf{E}_{RCP} + \mathbf{E}_{LCP})/\sqrt{2}, \tag{2.10}$$

$$\mathbf{E}_p = i(\mathbf{E}_{RCP} - \mathbf{E}_{LCP})/\sqrt{2}. \tag{2.11}$$

More generally, light with a specific ellipticity (ϵ, denoting the degree of circular polarisation) and rotation of polarisation axis (θ) can be written as ([29]):

$$\mathbf{E} = \begin{pmatrix} \cos\theta \cos\epsilon - i \sin\theta \sin\epsilon \\ \sin\theta \cos\epsilon + i \cos\theta \sin\epsilon \end{pmatrix}. \tag{2.12}$$

Now consider a material having a different refractive index for RCP and LCP light, what would the effect be on s-polarised light? The beam propagates according to

$$\mathbf{E}(t) = \frac{1}{\sqrt{2}}\left(\exp(i(n_R kz - \omega t)) \cdot \mathbf{e}_{RCP} + \exp(i(n_L kz - \omega t)) \cdot \mathbf{e}_{LCP}\right), \quad (2.13)$$

i.e. after traversing a distance d, the new polarisation state $\mathbf{E}'$ can be written as

$$\mathbf{E}' = \begin{pmatrix} 1 + i\frac{\pi d}{\lambda}(n_R + n_L) \\ \frac{\pi d}{\lambda}(n_L - n_R) \end{pmatrix}, \quad (2.14)$$

assuming a $\pi d/\lambda \ll 1$. We directly see that the beam has acquired both an ellipticity and a rotation of polarisation axis, the latter being equal to

$$\theta \approx \frac{\pi d}{\lambda}(n_L - n_R), \quad (2.15)$$

valid for small angles and assuming a purely real refractive index (i.e. no absorption). Thus, when linearly polarised light passes through a medium with different scattering rates for LCP and RCP, the net effect will be a rotation of polarisation and the acquisition of a definite ellipticity.

2.4.3 Magneto-Optical Kerr Effect

The Kerr effect has three variations depending on the orientation of the incoming beam with respect to the magnetisation. This is sketched in Fig. 2.12, where the distinction is made between polar, longitudinal and transverse Kerr effect.

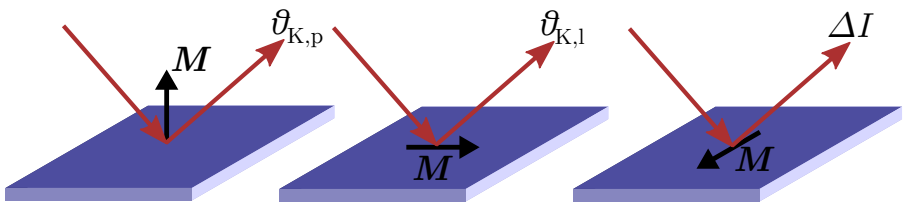

Figure 2.12: From left to right: polar Kerr effect where the magnetisation is oriented out-of-plane, longitudinal where it is in-plane and parallel to the plane of incidence of the incoming beam and transverse where it is in-plane and perpendicular to the plane of incidence.

For both polar and longitudinal effect an incident beam with linear polarisation, has its axis of polarisation slightly rotated, depending on the magnetisation. The intensity of the reflected beam is not altered. This is in contrast to the third effect, where the axis of polarisation is untouched but the magnitude is slightly reduced depending on magnetisation.

The microscopic origin of the polar Kerr effect was discussed for first time by H.R. Hulme[30] and later elaborated by P.N. Argyres[31].

Let us start the discussion by reviewing a phenomenon that is easier to explain, namely the Faraday effect. When light passes through a non-ferromagnetic material (e.g. quartz) and a magnetic field is applied along the direction of propagation, one finds that the axis of polarisation rotates as a function of the position. For quartz this rotation is a mere 3.7 rad/(T·m) for light with a wavelength of 632 nm[32].

This can be understood intuitively as the electrons in the material, responsible for the dielectric response, are split by the magnetic field (Zeeman splitting). LCP photons will couple to left circulating electrons and RCP photons will lead to a right circular motion of the electrons around the core. If no magnetic field is applied, both LCP and RCP photons will have the same refractive index, because they couple to (almost) identical electrons.

If a magnetic field is applied along the axis of propagation, it will exert a Lorentz force on the electrons with finite angular momentum. Electrons performing a left circular orbit will be pushed towards the core, electrons on a right circular orbit will move outwards. As the electric dipole moment is proportional to the radius of the orbit, left and right circular polarised light will have a different dielectric constant. This leads to a difference in refractive index. In the case for incident linearly polarised light, which can be regarded as the superposition of both left and right circularly polarised photons equal in magnitude but 45° out-of-phase, this has the effect that the beam leaving the material will have gained both a rotation of polarisation axis and a finite ellipticity, as has been shown in Sect. 2.4.2.

This illustrates the microscopic origin of the Faraday effect, but the question is still left open for the Kerr effect. The latter does not require an external field (only perhaps to yield large enough domains for measurement), but is also many magnitudes larger than the former. Typically, reflection of the top 10 nm yields a rotation of 1 mrad. The same rotation in quartz would require a magnetic field strength of 27,000 T. Only a magnetic field

of the order of the Weiss molecular field could explain such a large effect. However, a difficulty arises due to the fact that the molecular field does not couple to the electron motion and only serves to align spins. As was the case for XMCD, the issue is resolved through the spin-orbit coupling, which yields an additional term to the Hamiltonian of the system: $\hat{\mathcal{H}}_{SO} \propto (\nabla V \times \mathbf{p}) \cdot \mathbf{s} \propto \mathbf{l} \cdot \mathbf{s}$.

The above Hamiltonian can also be written as $\mathcal{H}_{SO} \propto (\mathbf{s} \times \nabla V) \cdot \mathbf{p}$, thus stating that the spin-orbit interaction has the effect of an applied magnetic field. For non-ferromagnetic materials there are equal numbers of spin-up and spin-down electrons, leading to zero net effect. Ferromagnetic materials on the other hand have an unbalanced spin population, as discussed in Sect. 1.3.2, allowing a non-zero effect.

In Ref. [31] it discussed how the electron wave function is determined by perturbation theory, where the spin-orbit interaction is the first perturbation. The Hamiltonian used for calculations is:

$$\hat{\mathcal{H}}_0 = \frac{\mathbf{p}^2}{2m} + V(\mathbf{r}), \tag{2.16}$$

$$\hat{\mathcal{H}}_{SO} = \frac{(\nabla V(\mathbf{r}) \times \mathbf{p}) \cdot \mathbf{s}}{2m^2c^2}, \tag{2.17}$$

$$\hat{\mathcal{H}}_{\gamma} = \frac{e\mathbf{A}(\mathbf{r},t) \cdot \mathbf{p}}{mc}, \tag{2.18}$$

where $V(\mathbf{r})$ is the potential formed by the crystal lattice and $\mathbf{A}(\mathbf{r},t)$ the vector potential of the incident light. One is then left with solving the Schrödinger equation:

$$(\hat{\mathcal{H}}_0 + \hat{\mathcal{H}}_{SO} + \hat{\mathcal{H}}_{\gamma})\psi = i\hbar\frac{\partial\psi}{\partial t}. \tag{2.19}$$

The approach followed in Ref. [31] is to first solve the problem taking only $\hat{\mathcal{H}}_0$ into account and applying perturbation theory for the spin-orbit interaction.

Afterwards time dependent perturbation theory is applied to the scattering of photons, represented by the Hamiltonian $\hat{\mathcal{H}}_{\gamma}$. From this the current density induced by the electric field is calculated and finally the relevant conductivity tensor $\bar{\bar{\sigma}}$. The latter being related to the refractive index by

$$\bar{\bar{n}}^2 = 1 + i\frac{4\pi}{\omega}\bar{\bar{\sigma}}, \tag{2.20}$$

as discussed in [31]. In this manner it can be shown that the polar Kerr angle is linearly proportional to the magnetisation of the sample.

For the general case of reflection of an incoming beam, we could write the effect of the sample on the polarisation state as the following:

$$\begin{pmatrix} E'_s \\ E'_p \end{pmatrix} = \begin{pmatrix} r_{ss} & r_{ps} \\ r_{sp} & r_{pp} \end{pmatrix} \begin{pmatrix} E_s \\ E_p \end{pmatrix}, \tag{2.21}$$

yielding a Kerr rotation θ and ellipticity ϵ[33] for an incident s-polarised beam equal to

$$\theta_s = \mathfrak{Re}\left\{\frac{r_{ps}}{r_{ss}}\right\}, \epsilon_s = \mathfrak{Im}\left\{\frac{r_{ps}}{r_{ss}}\right\}, \tag{2.22}$$

and for a p-polarised beam

$$\theta_p = \mathfrak{Re}\left\{\frac{r_{sp}}{r_{pp}}\right\}, \epsilon_p = \mathfrak{Im}\left\{\frac{r_{sp}}{r_{pp}}\right\}. \tag{2.23}$$

It can be shown[34] that the components of the reflection tensor have the form of:

$$r_{ss} = \frac{n_0 \cos\theta_0 - n_1 \cos\theta_1}{n_0 \cos\theta_0 + n_1 \cos\theta_1}, \tag{2.24}$$

$$r_{pp} = \frac{n_1 \cos\theta_0 - n_0 \cos\theta_1}{n_1 \cos\theta_0 + n_0 \cos\theta_1} - \frac{i2n_0 n_1 \cos\theta_0 \sin\theta_1 m_x Q}{n_1 \cos\theta_0 + n_0 \cos\theta_1}, \tag{2.25}$$

$$r_{sp} = \frac{in_0 n_1 \cos\theta_0 (m_y \sin\theta_1 + m_z \cos\theta_1) Q}{(n_1 \cos\theta_0 + n_0 \cos\theta_1)(n_0 \cos\theta_0 + n_1 \cos\theta_1) \cos\theta_1}, \tag{2.26}$$

$$r_{ps} = -\frac{in_0 n_1 \cos\theta_0 (m_y \sin\theta_1 - m_z \cos\theta_1) Q}{(n_1 \cos\theta_0 + n_0 \cos\theta_1)(n_0 \cos\theta_0 + n_1 \cos\theta_1) \cos\theta_1}. \tag{2.27}$$

The relevant refractive indices and angles have been indicated in Fig. 2.13 and Q is the Voigt constant, proportional to the off-diagonal terms of the dielectric tensor which are responsible for the rotation of polarisation.

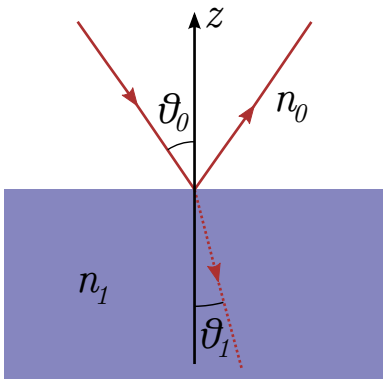

Figure 2.13: The coordinates used in calculating the Kerr effect for various angles of incidence.

An example curve of the effect of incident angle on polarisation rotation is shown in Fig. 2.14 for the polar effect. From this figure it is clear that for angles of incidence nearly perpendicular, the Kerr angle is the same, both in magnitude and sign, for s and p-polarisation.

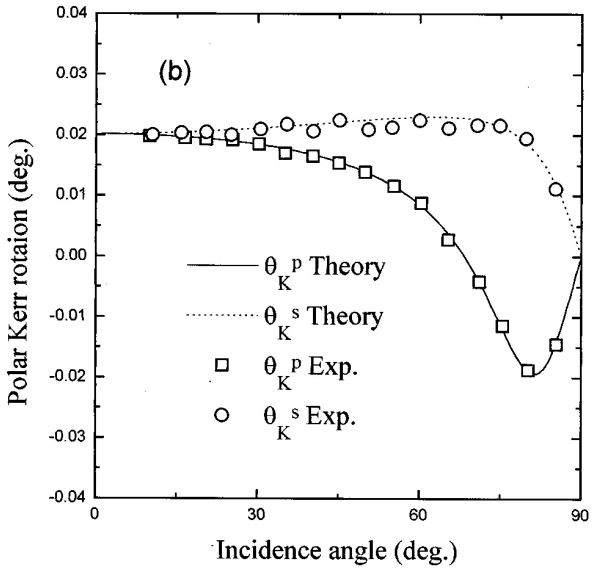

Figure 2.14: Experimental and calculated Kerr rotation angles for a Co/Pd multilayer system. For near normal incidence the sign and magnitude of the Kerr angle is the same for s and p-polarised rays. Reproduced from [34].

2.4.4 Optical path

The optical path is shown in Fig. 2.15. In the geometry shown, only the polar Kerr effect is measurable, because the beam is perpendicularly incident. The objective lens does focus the beam into a cone shape, thus the longitudinal Kerr effect may contribute to the reflectivity as well. However, when the entire beam is sampled, opposite halves of the beam, having opposite sign for the longitudinal effect, average out to zero.

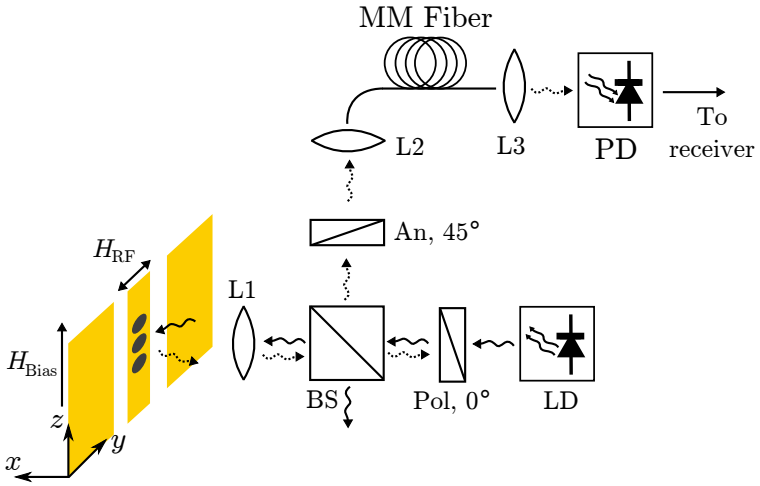

Figure 2.15: A basic sketch of the optical part of the set up, used for polar Kerr detection. LD is a laser diode, Pol a polariser, BS a non-polarising beam splitter, L1 an objective lens, An an analyser, L2 and L3 aspheric lenses and PD an ultrafast photodiode. The angle between the transmission axis of Pol and An is 45°. The coordinate system is indicated in the bottom left corner.

An off the shelf laser diode (655 nm, 50 mW, single mode, HL6544FM) generates light which is focussed by an aspheric lens into beam of 6 mm diameter, roughly the same size as the aperture of the objective lens. We chose red laser light for several reasons: firstly it is in the visible range, aiding in alignment. Secondly, both GaAs and Si photodiodes are sensitive in this wavelength range. GaAs photodiodes have the advantage of being fast, whilst Si photodiodes have a higher sensitivity and are easy obtainable. The former is used for the dynamic aspect, the latter for imaging purposes.

Light produced by a laser diode is already slightly linearly polarised[14, 35], but to maximise the effect we pass it through a linear polariser having an extinction ratio of 100,000:1. Of course, for maximum efficiency the transmission axis must be aligned with the polarisation axis of the original beam. In general, no specific orientation of the transmission axis with respect to the sample or applied magnetic field was maintained.

Laser light differs from conventional illumination sources used in microscopy. When dealing with the optics one can no longer use geometrical optics, which have to be abandoned in favour of Gaussian optics. A Gaussian

beam is characterised by two numbers (three if multiple transverse modes are present). The first is the beam width at the point where the beam is perfectly collimated, w_0. The intensity profile, perpendicular to the axis of propagation, is given by:

$$I(r) = I_0 \exp\left\{-2\frac{r^2}{w^2}\right\}, \tag{2.28}$$

where w is the width at that specific point.
The second number is the opening angle or the divergence of the beam, Θ, at a sufficient distance from the aforementioned point. Another important concept is the Rayleigh range, z_R, which is the distance over which the beam remains collimated. In the context of beams focussed to a point, this corresponds to the focal depth. The situation is sketched in Fig. 2.16.

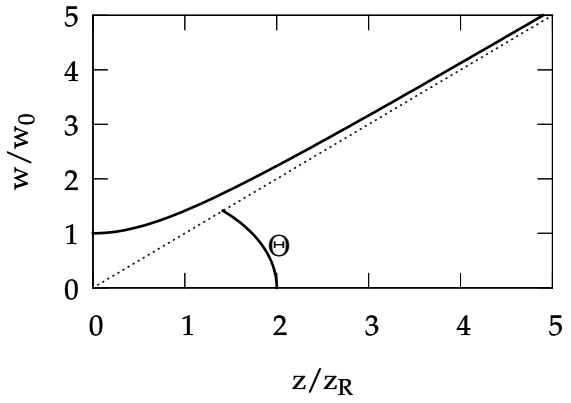

Figure 2.16: The evolution of the beamwidth of a Gaussian beam in function of the distance from the point of perfect collimation, in units of Rayleigh range. The dashed line indicates the asymptotic behaviour.

It can be shown that[35]:

$$\Theta = \frac{\lambda}{\pi w_0}, \tag{2.29}$$

$$z_R = \frac{\pi w_0^2}{\lambda}. \tag{2.30}$$

It can be shown that Θw_0 is an invariant under linear transformations, such as the effect of a lens. After a linear element, the beam parameters are given by:

$$w_0' \Theta' = w_0 \Theta. \tag{2.31}$$

Returning to our discussion of the optical set up, laser light coming from the polariser is passed through a beam splitter. This beam splitter performs a vital role in the optical path, because it allows to deflect light reflected of the sample to a different direction than its origin. Thus allowing it to be analysed. Several types of beam splitters are available, but one needs to carefully take into account that some of them affect the polarisation state. A beam splitter cube has a greater loss than other beam splitters ($\approx$ 10% in contrast to $\approx$ 3% typically), but it is the only type that does not alter the polarisation state. Though it performs a vital role, it is an optically costly component because is halfs the beam intensity. This means that only half the incident light is directed towards the required direction, the other half is directed towards a useless direction (typically a beamdump). For the illuminating path this is not a concern, but it also reduces the reflected light, requiring some compensation by increasing the incident flux.

After passing through the beamsplitter, the beam is focussed by a microscope objective lens, which is mounted on a piezo stage. We have opted to mount the objective on a piezo stage and not the sample itself because sample changes are frequently required, leading to exessive wear and tear of the delicate stage. The objective on the other hand never needs to be changed. We have made use of a 50X objective from Nikon, the parameters of which are summarised in Table 2.2. From the Numerical Aperture (NA) it follows that the focussed cone has a half angle of about 36°.

The optics of the objective have been aligned thusly that when the sample is in focus, the collected (white) light forms a nearly collimated beam, i.e. «*Infinity-Corrected*». Note that we are dealing with light collected by the objective, indifferent of how the sample was illuminated (brightfield, darkfield, ...) and does not pertain only to laser illumination. This (white) light can be then focussed by the tube lens onto a CMOS camera, which should be located in the focal plane of the tube lens. This type of imaging is called full frame imaging.

Though this may seem a minor technicality, it offers great advantage. Firstly, it implies that the tube lens and sensor can be located at any distance from the objective (due to the near perfect collimation), thus allowing greater flexibility in construction. Secondly, when the sample is in focus for full frame imaging, it is also in focus for laser illumination, i.e. both beams are collimated. This helps in obtaining a rough focus, and entails a significant

time gain in the operation of the microscope.

Table 2.2: Several key features of the objective lens used in the set up.

Nikon 50X CFI 60	
Type:	Infinity-Corrected Brightfield Objective
Magnification:	50X
Numerical Aperture:	0.6
Working distance:	11 mm
Focal length:	4 mm
Resolving power:	0.5 μm
Depth of focus:	0.91 μm

For a Gaussian beam, the objective lens with focal length f, transforms the beamwidth as

$$w_0' = \frac{\lambda f}{\pi w_0} = \Theta f. \tag{2.32}$$

The incident beam has a beamwidth of approximatly 3 mm, thus the focussed beam should have a beamwidth of 280 nm. However, this would entail an opening half angle of 42°, which is more than the NA of the objective allows for. If this is taken as the limiting factor, we arrive at a beamwidth of 350 nm. More meaningfull is the Full Width at Half Maximum (FWHM) of the beam intensity, equal to 410 nm, as can be derived from Eq. 2.28. Elements that are smaller than this, will yield a proportionally smaller signal, as they show decreasing overlap with the illuminating beam. The Rayleigh range is equal to 580 nm, which is the margin to keep the sample in focus.
The piezo stage allows for the positioning of the objective over a 20μm range in three directions: two parallel to the sample (y and z, used for imaging) and one perpendicular (x, used for focussing), as indicated on Fig. 2.15. The stage is specified with a bidirectional repeatability (i.e. the variation in position if the stage is moved away from a certain point and returned to it) of 200nm, sufficiently smaller than the optical resolution and focal depth discussed above. In practice, if successively smaller scanning windows are used the repeatability nears the step resolution of 20nm.
The reflected light is focussed on a conventional photodiode (not shown in diagram) which transforms the light intensity into a proportional current. The reflectivity data can then be used for imaging purposes and to

correctly focus and position the beam on the sample. The piezo stage itself is driven by a high voltage amplifier which receives input from an in house developed controller. A microcontroller generates analog output voltages and simultaneously and measures the photodiode current. This way, scanning the beam over the sample and measuring the reflectivity at each point is handled in realtime and does not require intervention from a computer. The latter would entail a certain delay ($\approx 100-500$ ms) between each pixel due to the non-realtime nature of the communication protocol used (USB). The data collected by the controller is then passed to the host PC.

The focussing procedure is the same as used for STXM measurements; the beam is repeatably scanned over a clearly defined edge (for example an edge of the gold CPW on the Si substrate) whilst the objective is moved perpendicular to the sample. The resulting image resembles a hourglass as shown in Fig. 2.17. The distance at which the sample is in focus is located at the waist. The length of the waist gives the length of the focal depth, in this case approximatly 1 μm, comparable with (twice) the Rayleigh range mentioned above.

Whilst scanning the beam over the sample is very efficient for final alignment, it is impractical for crude alignment because of the limited scanning range and it is very time consuming to obtain an image. Therefore white light can be injected before the beamsplitter through the use of a dichroic mirror so full frame imaging can be performed. To this end, the light is redirected through a tube lens onto a CMOS focal plane array.

Scanning a clearly defined edge also allows an estimate of the beamwaist of the light at focus. The actual profile is the convolution of the edge (Heaviside function) and the light beam profile (Gaussian with a defined width). In effect, the profile will follow the equation:

$$I(y) = A \cdot \operatorname{erfc}\left(\frac{\sqrt{2}(y - y_0)}{w}\right) + B, \tag{2.33}$$

where A and B are scale and offset parameters, y_0 the edge position and w the beamwidth. Such a profile is shown in Fig. 2.18, where the beamwidth was fitted to $w = 470$nm, comparable to the theoretical value mentioned above.

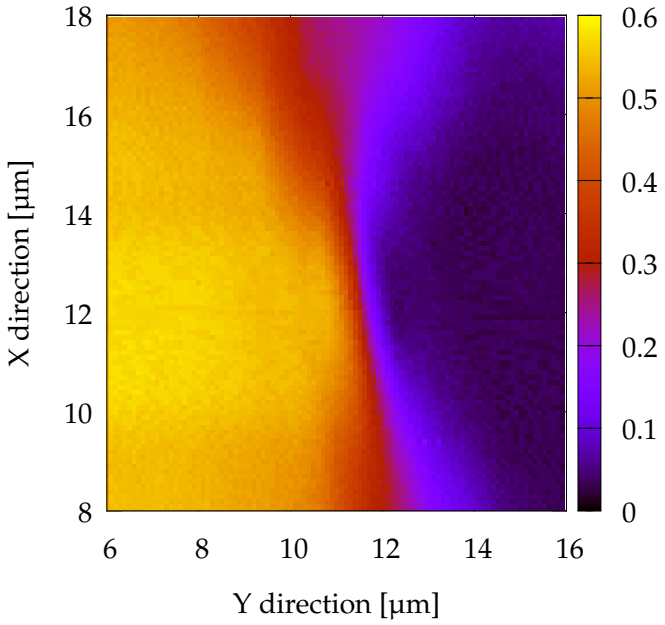

Figure 2.17: A focal scan where the probe beam is scanned over an edge of the gold CPW on the Si substrate (horizontal axis) and moved towards the sample (vertical axis). The narrowest point of the hourglass figure is where the sample is in focus. Each pixel corresponds to 20 nm and the colourscale relates to the photocurrent measured at each pixel.

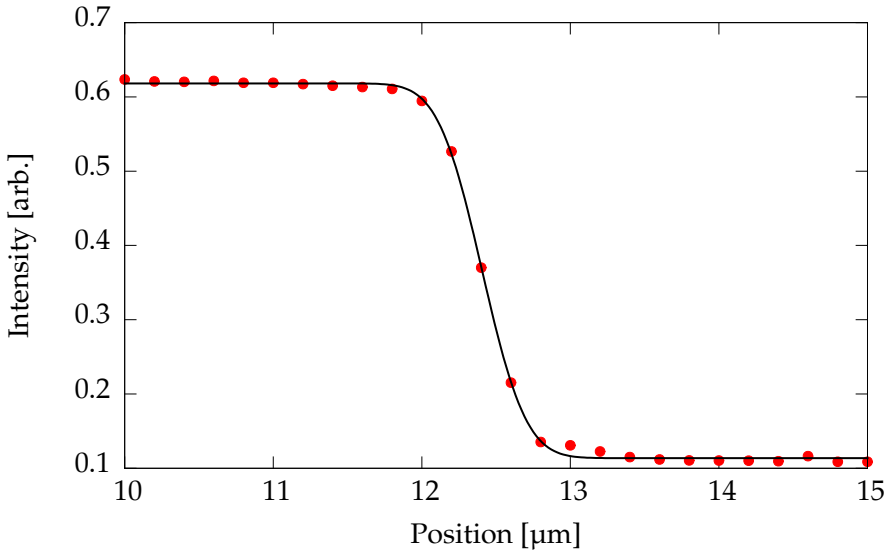

Figure 2.18: An optical reflection profile when the beam is scanned over an edge of the gold CPW on the Si substrate. The sample was properly focussed and the beamwidth was only 470nm.

To obtain such a resolution in practice, care has to be taken to keep the optics stable. Firstly, there are vibrations to which the system is subjected. In our case, an optical breadboard, a slab of marble and a rigid mechanical frame are sufficient to isolate the system for the most part from the environment. This is in stark contrast to a typical TR-MOKE set up, which requires extensive damping and a fullscale optical table. This is explained by the simplicity and rigidity of the optical path in our case. There are no critical alignments present in our case and almost all optical components are rigidly connected.
Secondly, care has to be taken that the set up is kept at a constant temperature. When subjected to temperture drift of several degrees Celsius, the sample can drift a considerable amount. In effect, the focus will be lost or the beam will no longer be positioned correctly.
The reflected laser beam is redirected by the beamsplitter onto an analyser (An) of which the transmission axis is at angle of 45°with respect to the transmission axis of the first polariser. We can prove quite easily that this analyser transforms the variations of the polarisation state of the light into intensity variations in a linear fashion. Let us assume the we are dealing with incoming *s*-polarised light[3]. The Kerr effect induces a rotation and and ellipticity depending on the magnetisation state, thus for the reflected light:

$$\mathbf{E} = \begin{pmatrix} 1 \\ \theta(m_z) + i\epsilon(m_z) \end{pmatrix}, \tag{2.34}$$

as follows from Eq. 2.12 and assuming small angles. We then pass this light through an analyser at angle of 45°, yielding a new polarisation state equal to

$$\mathbf{E}' = \frac{1}{2}\begin{pmatrix} 1 & -1 \\ -1 & 1 \end{pmatrix}\begin{pmatrix} 1 - i\theta(m_z)\epsilon(m_z) \\ \theta(m_z) + i\epsilon(m_z) \end{pmatrix}, \tag{2.35}$$

$$= \frac{1}{2}\begin{pmatrix} 1 + \theta(m_z) + i\epsilon(m_z) \\ 1 + \theta(m_z) + i\epsilon(m_z) \end{pmatrix}. \tag{2.36}$$

The intensity, given by $I = \mathbf{E}'^{\dagger}\mathbf{E}'$, thus yields

$$I \approx \frac{I_0}{2} + I_0\theta(m_z). \tag{2.37}$$

[3]Any other type of polarisation would only require a rotation of the coordinate system.

Thus any polarisation rotation is transformed linearly to an intensity variation. If θ_K is the Kerr angle for a completely out of plane saturated material and taking into account the linear dependence between magnetisation and Kerr rotation, we can write the relative variation as

$$\frac{\Delta I}{I_0} = 2\theta_K m_z, \tag{2.38}$$

where I is the intensity after the analyser.
After passing through the analyser, the light is focussed into a multimode fiber, having a diameter of 50µm and a NA of 0.2. This is done by making use of an aspheric lens assembly. Using Eq. 2.32, it follows that in order to obtain efficient coupling

$$f \geqslant \frac{w_0}{NA_{fiber}} \approx 8.8mm, \tag{2.39}$$

else the angle of incidence is too steep and not all light undergoes Total Internal Reflection (TIR), a prerequisite for fiber optic light transportation. The light also needs to be properly collimated, elsewise it can not be focussed onto a spot the size of the fiber diameter. Thus from Eq. 2.31 it follows that the maximal allowed divergence is

$$\Theta \leqslant \frac{NA_{fiber} r_{fiber}}{w_0} \approx 2.8mrad. \tag{2.40}$$

The lens is fixed at production with respect to the fiber end, needing no further alignment. More critical for efficient coupling than the position of the beam on the lens is the angle of incidence. For this reason the aspheric lens assembly is mounted on a tip and tilt stage which allows fine adjustment of the angle between the incoming beam and the assembly.
We opted for a commercial multimode fiber (OM3). The type of optical fiber places an upper limit on frequencies that can be transported. This is due to a feature called Intermodal Dispersion. This finds it origin in the fact that rays entering the fiber under different angles, travel slightly different distances through the fiber. When they arrive at the endpoint, the distance travelled by two rays could be equal to half the wavelength of the modulating signal. The upper frequency limit is thus dependent on the total length of the optical fiber. For OM3 fiber the upper limit is $1.5 - 2$ GHz·km for telecom wavelengths. Because of the dependence on wavelength, we expect that the upper limit for 655 nm is even higher. Since

the fiber we have used is only 50 m long, we estimate an upper frequency limit due to Intermodal Dispersion to be 40GHz. The situation in reality is more complex, but it is beyond the scope of this work. For a detailed discussion the reader is directed to Ref. [32].
OM3 cable has an increased attenuation for our wavelength (655 nm), of approximatly 10 dB/km. Due to the fact that we only need 50 m, this is not a problem.

2.4.5 Electrical path

Shown in Fig. 2.19 is the electrical part of the set up. The sample is excited with an RF magnetic field induced by the current from a microwave signal generator (HP 8672A) flowing through a stripline.

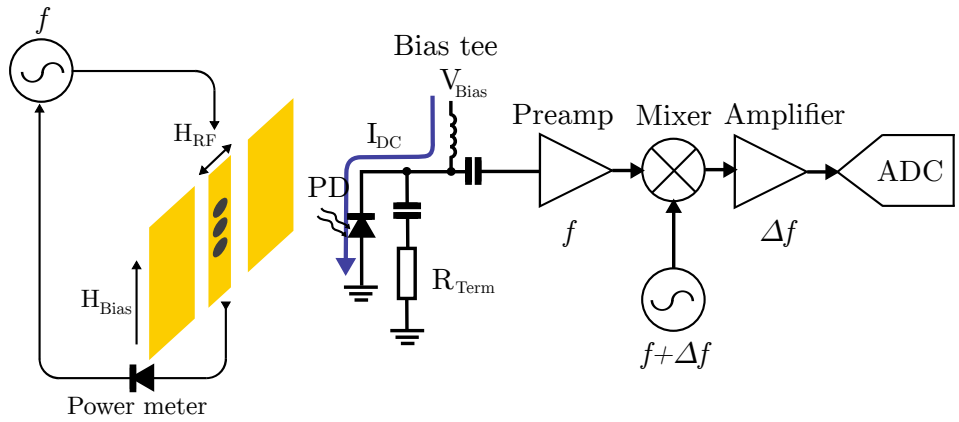

Figure 2.19: A simplified schematic of the electrical part of the set up. A diode detector connected to the sample helps in keeping the power transmitted through the sample level when the frequency is varied. Also shown are the photodiode (PD), termination resistor (R_{Term}), bias tee, RF preamplifier, frequency mixer, low frequency amplifier and ADC. Both signal generators produce a tone in the microwave range (f), but are slightly offset by frequency Δf in the kHz range.

The RF current flowing out of the sample is measured with a diode detector. The output power of the signal generator is not constant when the frequency is varied. Nor is the loss associated with transmission through a

coax cable or a CPW. Therefore, to keep the RF current through the sample constant, the signal of the diode detector is fed back to the signal generator. This in turn adjusts the output power to keep the detector voltage constant when the frequency is changed. In this manner the microwave magnetic field used for exciting the nano elements, is kept constant over a full range of frequencies.

As discussed in the previous section, the magnetisation dynamics of the sample modulates the polarisation state of the reflected laser light. When analysed, these polarisation changes are transformed into small modulations of the intensity. This in turn is transformed into a RF current by the ultrafast photodiode, model G4176-03 from Hamamatsu, shown in Fig. 2.20. This is a GaAs Metal-Semiconductor-Metal photodiode, which has a large area (200x200 μm), low dark current, low noise, high responsivity (the amount of photocurrent per incident optical power) and a rise and fall time of 30 ps, yielding a 3 dB cut off of about 12 GHz.

Figure 2.20: The external view of a G4176-03 MSM photodiode, which was used using during this work. Copyright Hamamatsu Photonics.

Such a photodiode is a planar construction where two interdigital electrodes are deposited directly on top of a semiconductor, forming two Schottky diodes[36]. This situation is sketched in Fig. 2.21. The two diodes are back to back, so when a voltage is applied across the terminals, at least one is biased in reverse and no current flows. However, when a photon strikes the semiconductor material between two metal fingers, charge carriers are generated. They then drift towards the electrodes, generating an electrical current known as the photocurrent.

Figure 2.21: A sketch of the structure of a MSM, yellow indicates metallisation, blue the semiconductor substrate (InGaAs in our case).

The photodiode is coupled to the signal chain through a capacitor, which blocks all low frequency components. This way, the large DC current is separated from the much smaller RF current. The photodiode itself is a high impedance source (i.e. current source) which is matched over a large frequency range to the 50Ω system impedance through the use of a 50Ω shunt resistor (R_{Term} in the diagram). The photodiode is biased via an inductor which forms a high impedance for the microwaves (effectively blocking them), but shunts the DC photocurrent. For monitoring purposes this DC photocurrent was recorded during each measurement.

The microwave signal from the photodiode is first amplified by the preamplifier (KU LNA BB 2001200 A) from Kuhne electronic GmbH. This amplifier increases the signal level by 30dB and adds very little noise of its own. The specifications are noted in Table 2.3. Such a preamplifier is one of the most important components; as we will later discuss it sets the noise floor of the entire system.

After a first amplification the signal frequency is lowered from the microwave range (GHz) into the low frequency range (kHz) by a frequency mixer. This a non-linear device which essentially performs a multiplication of two input signals. One of the input signals is named LO (Local Oscillator) and the other one RF (typically a low power signal), with the resultant called IF (Intermediate Frequency). From elementary trigonometry it follows that if we multiply two sinusoidal signals with frequencies f_{LO} and f_{RF}, the result will be two tones: one at a frequency of $f_{LO} + f_{RF}$ and one at $|f_{LO} - f_{RF}|$. In our case f_{RF} and f_{LO} are nearly equal, thus the signal at the highest frequency will be at twice f_{RF}, typically several gigahertz. This signal is terminated into a 50Ω load and not detected. The signal at the lower frequency will however be in the range of several kilohertz, set by

Table 2.3: The specifications of the preamplifier used in the set up (KU LNA BB 2001200 A). Data from the manufacturer[37].

KU LNA BB 2001200 A	
Frequency range:	$2-12$ GHz
Noise figure:	typ. 1.8 dB, max. 2.0 dB ($2-8$ GHz)
	typ. 2.3 dB, max. 2.5 dB ($8-12$ GHz)
Gain:	typ. 30 dB, min. 28 dB
Maximum input:	0 dBm
Saturated power (P1dB):	typ. 13 dBm ($2-8$ GHz)
	typ. 7 dBm ($8-12$ GHz)
Third order intercept (IP3):	typ. 18 ($2-8$ GHz)
	typ. 10 dBm ($8-12$ GHz)

the difference between LO and RF, and will be measured.

Mixers can thus convert a high frequency signal down to a lower frequency one, but in general this is a lossy process, quantified by what is called conversion loss. Moreover the conversion loss is dependent on the frequencies applied to the input. In Fig. 2.22 we have shown the conversion loss in function of f_{RF} for the mixer used in our set up. For this measurement the IF frequency is kept constant, i.e. f_{RF} and f_{LO} are separated by the same frequency throughout the graph. The mixer we have used is a ZX05-153+ from MiniCircuits and has a usable frequency range of $3.5-15$ GHz. It requires a constant power of +7 dBm, 5 mW to operate at maximum efficiency.

The mixer is driven by a second signal generator that produces a signal of which the frequency is offsetted by several kilohertz (Δf) with respect to the excitation frequency (f).

The low frequency signal is subsequently amplified, filtered and sampled using a 24-bit analogue to digital converter (ADC). An FFT is then performed on the acquired data and the magnitude of the signal at the frequency of interest (Δf) is calculated. The use of an ADC and FFT allows to narrow the detection bandwidth to levels not easily attainable by analogue components. This narrow bandwidth allows for a suppression of noise which is proportional to the square of detection bandwidth.

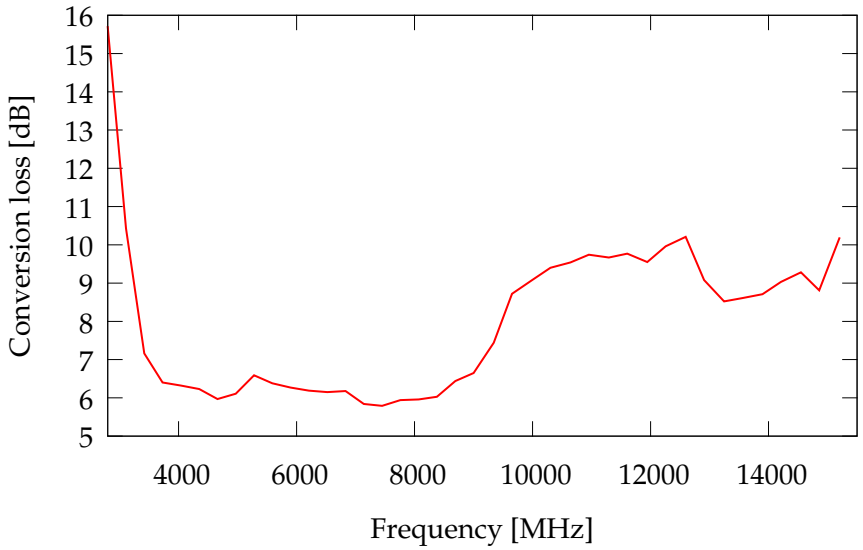

Figure 2.22: The conversion loss of the frequency mixer in dB scale. $f_{IF} = 30$ MHz throughout, +7dBm of drive supplied at the LO-port. Data obtained from the manufacturer[38].

Detection limit

It is interesting to perform an analysis of the signal to noise ratio of the set up, because this can give some insight into how fast measurements can be made. We will start by first estimating the strength of a typical magnetic signal.

Signal estimate We have seen in the previous section that the relative optical intensity variation is given by (we now use P as the symbol for intensity, to avoid confusing with the photocurrent, denoted I):

$$\frac{\Delta P}{P} = 2\,\Delta m_z\,\theta_K. \tag{2.41}$$

The photodiode transforms this intensity into a proportional current. If we take Δm_z to be the maximum value that m_z takes, and assuming sinusoidal oscillations, we find the root mean square value of the varying current to be

$$i = \sqrt{2}\Delta m_z\,\theta_K\,I_{DC}, \tag{2.42}$$

where I_{DC} is the DC photocurrent.

To estimate the signal current, we start out with the maximum power we want to illuminate our sample with. Several optical parameters for relevant materials are summarised in Table 2.4 for reference. Experience teaches us that high illumination can significantly heat up the sample, even destroying it.[4] We use about 10 mW of illumination at 655 nm. For Py the reflectance is 0.55, so about 5.5 mW of laser power is reflected back. If we refer back to Fig. 2.15, we see that this light needs to pass both the beam splitter (where it loses half the intensity) and the analyser (where it also loses half the intensity). The light that arrives at the fibre is thus about 1.4 mW. Taking losses from the coupling to the fibre into account, the light arriving at the detector is about 1 mW. The photodetector converts this optical power into a current with a responsivity of about 0.1 A/W, thus yielding a photocurrent of 100 μA.

Table 2.4: Optical parameters of several frequently encountered materials at a wavelength of 655 nm. Data reproduced from [39, 40, 41].

Material	Reflectance, R	Penetration depth, μ	θ_K
Au	0.95	15 nm	N/A
Si	0.34	29μm	N/A
Fe	0.56	16 nm	3.9 mrad
Co	0.69	12 nm	0.3 mrad
Ni	0.71	12 nm	0.8 mrad
Permalloy, Py,	0.55	-	1.0 mrad

As an estimate for the maximum excursion of m_z we arbitrarily choose 0.01 at resonance. It will be shown later that this value is indeed of the correct order of magnitude for the systems we have examined.
All of the measurements were done on Permalloy, which has a polar Kerr angle of 1 mrad when completely saturated out of plane[41]. Combining all these estimates, we arrive at a typical RMS signal current of i =1 nA, which is equal to a power of $5 \cdot 10^{-17}$ W or -130 dBm in a 50 Ω system.
At this point we face the first serious technical challenge, namely separation between the signal that excites the magnetic system and the signal that is generated by the latter. If we assume a 1 mW excitation signal, we need

[4]Under our standard illumination conditions, a SiN membrane had evaporated where exposed to the laser beam.

shielding between the start of the signal chain and the receiver equal to 130 dB or 10^{13} in terms of power. This level of shielding is unobtainable in our geometry (both sample and photodiode are exposed to free space) requiring that the detection is separated from the excitation by a large distance. Because we are dealing with an optical signal, we can transport it almost lossless (apart from coupling losses) over great distances using an optical fibre. This made it possible that the detection part of the set up could be placed in another room, 25 m away from the excitation part of the set up.

It is also important to take into account possible ground loops. When several electrical devices share a ground reference (e.g. mains earth, negative supply rail, etc.), these connections can form closed loops. These loops tend to behave as a quite efficient antenna for all types of low frequency noise (50Hz hum, switch mode power supply interference, ...). The interference that is picked up this way can interfere with measurements, which are performed in the same frequency range. Typically, the interference shows up as broad peaks in the FFT spectrum. All instruments received power from the same supply, but it was found that USB cables needed to be galvanically isolated to prevent ground loops. This was done using evaluation boards from Analog Devices for their ADuM4160 integrated circuit.

Noise estimate Now let us analyse the noise present in the system and estimate its magnitude. We can separate it into two major categories: additive and multiplicative noise. The magnitude of the additive noise does not depend on the signal level and for multiplicative noise it does. Orthogonal to this, we can make the division between high frequency and low frequency noise. Stability (laser intensity, piezo stage, ...) falls into the category of multiplicative low frequency noise and will not be taken into account, because it is relatively easy to control and does not form a fundamental limit.

Noise is always proportional to the square of the detection bandwidth. If we average over longer periods (i.e. lower bandwidth) the noise will average out. Therefore noise is always specified as the noise spectral density, e.g. $\mathrm{A}/\sqrt{\mathrm{Hz}}$, which removes this dependency on bandwidth.

The major contribution to the noise of the set up is formed by the additive high frequency noise of the photodiode, followed by the noise added by the

preamplifier. Noise generated by the photodiode has three contributions:

- The light that is incident and the current that is generated are both quantised by respectively photons and electrons. These carriers are ruled by Poisson statistic, which results in an average number N of carriers with a standard deviation of $\sqrt{N}$. Variation of the number of quanta within this standard deviation results in what is called Shot noise. For the generated photocurrent, one can show that the RMS current noise density is given by

$$i_{Shot} = \sqrt{2qI_{DC}}, \tag{2.43}$$

  where q is the elementary charge.

- Even when not illuminated, the photodiode will still produce noise. This is characterised by an optical signal that would produce the same strength as the noise in a 1Hz bandwidth, called the Noise Equivalent Power (NEP) and is specified in $W/\sqrt{Hz}$. For the photodiode we use, this is equal to $3 \cdot 10^{-15} W/\sqrt{Hz}$ at 850 nm, which is a factor of ten better than an off the shelf Si photodiode such as the BPW34 with $4 \cdot 10^{-14} W/\sqrt{Hz}$.

- The terminating resistor (R_{Term}, 50Ω), which matches the photodiode to the signal chain, also generates a voltage across its terminals. This is due to thermal excitation of the charge carriers and gives a noise voltage of

$$v_{Johnson} = \sqrt{4k_B T R_{Term}}, \tag{2.44}$$

  where k_B is Boltzmans constant.

These are all forms of white noise because there is no frequency dependence in their magnitude. They are only limited in frequency by the parasitic elements of the photodiode such as inductance from bond wires or stray capacitances. Therefore we assume they have the same frequency cut off as the signal bandwidth of the photodiode, i.e. 12GHz. As these three sources are uncorrelated, we can add them in the following fashion

$$i_{total} = \sqrt{i_{Shot}^2 + i_{Johnson}^2 + i_{NEP}^2}. \tag{2.45}$$

If we would calculate the magnitude of each factor, we would find that the major contributor is the Johnson noise with a value of $1.8 \cdot 10^{-11} A/\sqrt{Hz}$.

About three times smaller is the contribution from the Shot noise (at $I_{DC} = 100\mu A$) at $5.7 \cdot 10^{-12} A/\sqrt{Hz}$. Completely negligible is the NEP which is only $4.5 \cdot 10^{-17} A/\sqrt{Hz}$.
The Signal to Noise Ratio (SNR, expressed in dB) is calculated by comparing the magnitude of the signal and noise power, thus we can write that

$$SNR = 10 \cdot \log\left(\frac{2I_{DC}^2 \theta_K^2 \Delta m_z^2}{B(2qI_{DC} + 4k_B T/R_{Term} + (\mathcal{R}_{850\,nm} \cdot NEP)^2)}\right). \quad (2.46)$$

As we follow the signal through the signal chain we would find that the SNR systematically degrades as each stage adds its own noise. The degradation of SNR by a component is quantified by the Noise Figure (NF, expressed in dB), which is usually frequency dependent. For an amplifier it needs to be measured, but for a lossy component it is simply equal to the loss. For a chain of components each with linear gain G_i and noise factor F_i (the linear equivalent to NF) the noise factor is given by the Friis equation[42]:

$$F = F_1 + \frac{F_2 - 1}{G_1} + \frac{F_3 - 1}{G_1 G_2} + \ldots. \quad (2.47)$$

Due to the dependence on gain, components towards the end of the signal chain have little or no impact on the overall NF of the system and in most cases the first preamplifier will determine the total NF.
For each of the electrical components in Fig. 2.19, we have summarised their gain (or loss) and NF in Table 2.5.

Table 2.5: Gain and Noise Figure of the different stages in the signal chain.

Device	Gain (db)	NF (dB)
Bias tee	-0.25	0.25
Preamplifier	30.0	1.8
Frequency mixer	-9.0	12.0
Audio amplifier	30.0	1.0

Using Eqn. 2.47 with these values, we arrive at a NF of 2.3dB, just a bit larger than the NF of the preamplifier.
With estimates for both signal and noise, we can derive the SNR for a certain detection bandwidth, which is shown in Fig. 2.23. A yardstick is the SNR at a 1 Hz bandwidth, because this is the quality for a measurement that takes one second. If this is too low, measurements will take a very

long time (from minutes up to hours). This would place a more stringent requirement on the stability of the optics and signal generators.
If on the other hand, the SNR is a large value for a 1 Hz bandwidth (i.e. $\approx$ 20 dB), then each measurement point can be done in one second. In this case, drifts are not such an important issue.

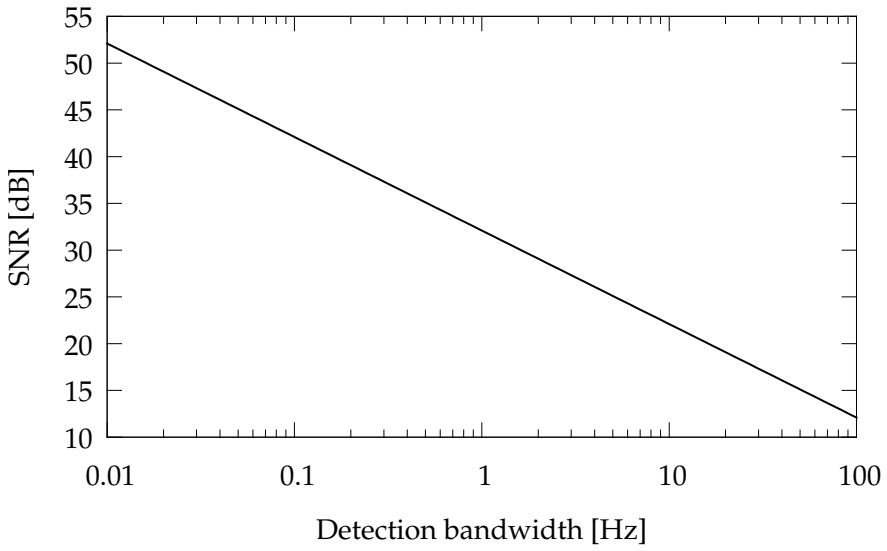

Figure 2.23: The SNR for a typical DC photocurrent of 100μA and a maximum excursion of m_z of 0.01 for a Permalloy sample.

From Fig. 2.23 we see that the SNR for a 1 Hz bandwidth is even more than 20 dB. Thus we can rest assured that drifts and stability will not have a large impact on the measurements.

2.4.6 Frequency dependence

Any spectrum that is measured is the product of the physical spectrum (i.e. the magnetic signal) and the frequency response of the signal chain. Typically, the gain or loss of an amplifier or mixer can vary by several decibels when the frequency is changed over several gigahertz. This means that a possible magnetic resonance could be hidden or severely distorted by electrical effects.
In order to minimise these effects, both excitation and detection need corrections. As mentioned previously, the excitation power that was transmitted through the sample was kept level through the use of a power detection

diode in a feedback loop with the signal generator. On the side of the detection, it is not immediately clear how the conversion efficiency could be kept level. To correct these effects in software after the measurement, the conversion efficiency in function of frequency needs to be known.

If we look at where the measured noise comes from, we find that it mostly originates at the source of the signal chain in the termination resistor. Therefore, all this noise follows exactly the same path as the signal itself, apart from the electro-optical conversion. Thus, if we measure the noise in function of the frequency, we acquire a conversion efficiency function for the signal chain. The noise is measured in a 10kHz bandwidth around each frequency. The result is shown in Fig. 2.24, where the lowest conversion efficiency is set to one.

The recorded spectra are normalised by dividing the measured value by the conversion efficiency at each frequency. If we compare the efficiency in Fig. 2.24 with the loss of the mixer in Fig. 2.22, two differences strike us. Firstly, the total efficiency varies much faster in function of frequency than the mixer. Secondly, the efficiency does not drop by 50% around 9GHz as it does for the mixer. Clearly, the mixer is not the main component determining the frequency behaviour of the set up.

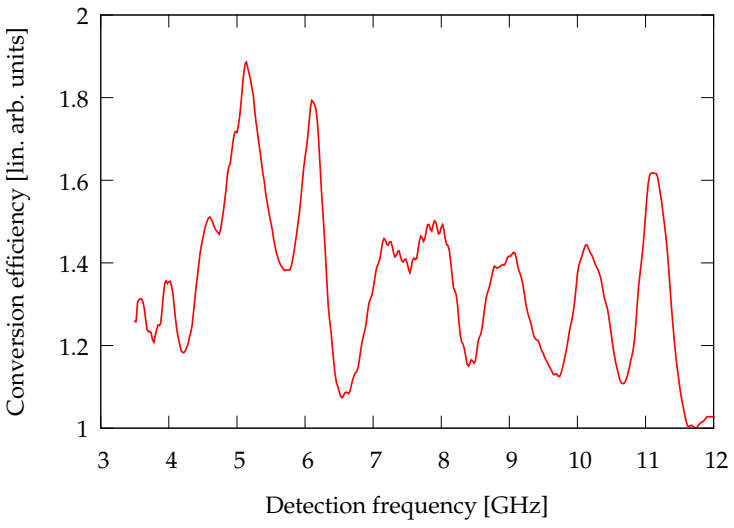

Figure 2.24: The relative conversion efficiency of the signal chain, apart from the photodiode. The lowest efficiency is set to one. The scale is linear in terms of power.

2.4.7 Anomalous noise

As we have just discussed, the measured noise serves as a calibration for the conversion efficiency. It was found however that the measured noise did not resemble that calibration curve of Fig. 2.24 when the photodiode is illuminated. The measured response is shown in Fig. 2.25, with the previous calibration curve also shown for comparison.
The noise was obviously dominated by another factor than the terminating resistor, as we had assumed in the previous section. This noise spectrum was reproducible, thus eliminating sources such as ground loops, which are more or less random.
The first hint towards the cause was found in the spacing of the oscillations, which was approximately 350MHz. If these high frequency noise peaks would originate from some cavity, the latter would have a length of $f/(2c)$ (with c the speed of light) in vacuum. The cavity would thus have to be about 60cm long, which corresponds with the distance between the sample and the laser diode. This was confirmed as the introduction of a glass rod in this part of the optical path would slightly alter the oscillation frequency.

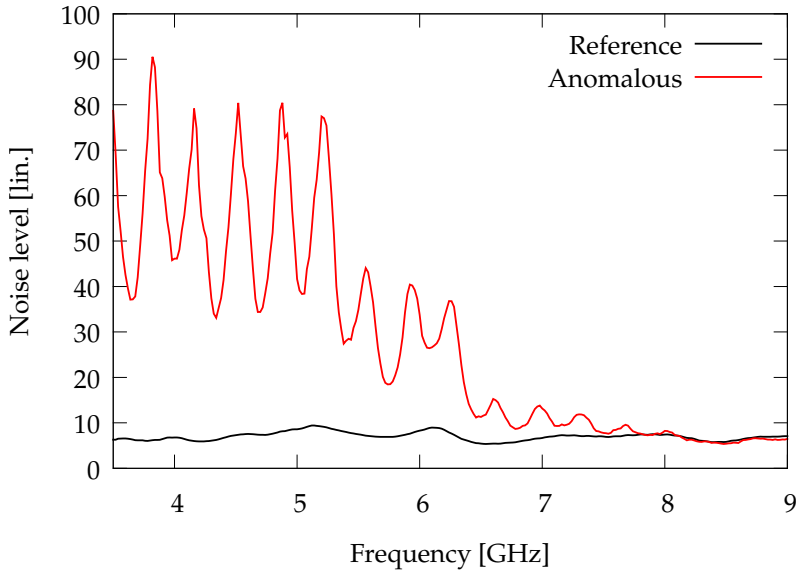

Figure 2.25: The normal and anomalous noise levels in function of the measurement frequency, with the latter clearly showing more noise then would be expected. Moreover the anomalous noise has a very strong frequency dependence.

As mentioned in Sect. 2.4.4, the beam splitter redirects part of the reflected laser beam away from the laser diode so it can be analysed. However, half of the light that is reflected of the sample ends up back at the laser diode. The optical cavity of the laser diode (which was previously only a few mm) has been expanded in this way up to several tens of centimetres.

A laser is nothing more than an optical resonator, exciting all modes that fit in the resonator and that fall within the gain curve of the material (gain in function of frequency). For a diode laser the gain curve drops to one only at several terahertz[35]. The excessive noise is thus due to a closer mode spacing introduced by the larger cavity.

The solution to the problem is sketched in Fig. 2.26.

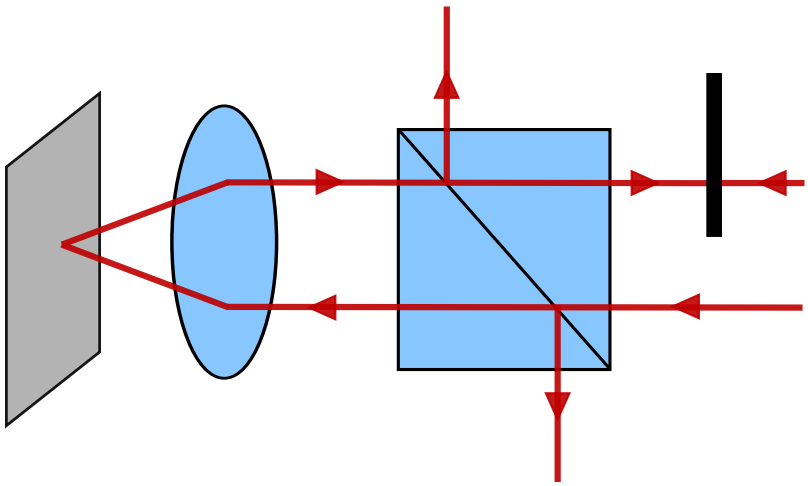

Figure 2.26: To resolve the anomalous noise issue half of the beam is blocked between the laser diode and the beam splitter.

The light is incident under an angle on the sample, thus light travelling towards the sample on the left half of the beam will be reflected into the right half. This creates an opportunity to block the reflected light. By blocking half the beam between the laser diode and the beam splitter, the reflected light is prevented to return to the laser diode. In effect, the optical cavity is reduced to its previous dimensions and the anomalous noise has disappeared.

2.5 Sample preparation

Samples were prepared by A. Gangwar at the University of Regensburg. Most samples were prepared on a Si substrate, in contrast to SiN substrates typically used for STXM measurements. These SiN substrates consist of only a thin SiN membrane, typically 100 nm thick. Because it was found that the thermal load caused by laser illumination could damage the fragile SiN substrate, we opted for a Si substrate (10mW of optical power on a 1µm diameter spot equals 13GW/m^2, cfr. 1kW/m^2 for sunlight). This provides a thermal sink for the heat produced both by the laser beam and the microwave generator.
Samples were produced in a two step lithography process, one for each type of metallisation (Au or Permalloy). Electron beam lithography was used for making the necessary definitions. One such a lithography step if sketched in Fig. 2.27.

Figure 2.27: A sketch of the lift-off process used to prepare the samples. A thin layer of e$^-$-beam resist (dark green) is deposited on top of a Si-wafer (blue) and exposed to a focussed beam of electrons. This causes decomposition into shorter molecules (bright green), which can be selectively dissolved, leaving the rest of the resist intact. The sample is then exposed to a metal vapour, which condenses on the surface (gold). Afterwards one dissolves all the remaining resist, also removing metal deposition not directly on the surface. The resulting sample (shown at the far right), is obtained after ALD deposition of Al_2O_3.

First a thin layer of electron beam resist was spin coated to the sample. A highly focussed beam of electrons (with a typical energy of $10 - 30$kV) then irradiated specific areas of the sample where later metal would be deposited. Such an exposure would take place in either a modified Scanning Electron Microscope or a dedicated tool. Molecules that make up the resist (polymers) that were exposed to the radiation broke up into smaller parts,

which are easier to dissolve than their bigger brethren in suitable solvent. In this manner areas exposed to the radiation would no longer be covered by a protective layer of resist.

After this step, a metal deposition took place, where the sample was exposed to a metal vapour. The vapour condenses on the sample, forming a very thin layer (typically $1 - 100\,\text{nm}$). However, after deposition the sample is be exposed to a strong solvent, dissolving the remaining photoresist and any metal on top of this layer. Thus only the irradiated areas would be covered with the metal film. This process is called lift-off.

The entire process was then repeated for a second time, now using a different material. First a Au CPW was deposited, after which Permalloy structures were fabricated. To prevent rapid oxidation, especially taking into account the thermal load, the samples were «*capped*» with a conformal coating of Al_2O_3 using Atomic Layer Deposition. This layer had a typical thickness of 7 nm. Now they could be mounted on sample carriers and electrically connected.

The samples consisted of thin Permalloy discs placed on top of the centre conductor of a CPW. The current flowing underneath the discs induces an in-plane magnetic field used for exciting the sample. We require a strong excitation, which leads to a compact CPW used for exciting the sample.

Due to the use of a thin substrate (200 μm Si) there is little coupling between the centre conductor and the ground plane. If the gap between centre and ground plane is too large, the CPW will behave as an inductor, reflecting most of the microwaves back to the generator. Closing the gap will lead to an increased capacitive coupling, balancing out the inductance to yield a $50\,\Omega$ transmission line.

We chose a gap of 50 μm which yields a centre conductor with a width of 100 μm, and a thickness of 50 nm. The scattering parameters of this CPW were calculated with Sonnet Lite[43] and are shown in Fig. 2.28. Clearly the CPW is well designed and usable up to 10GHz and higher.

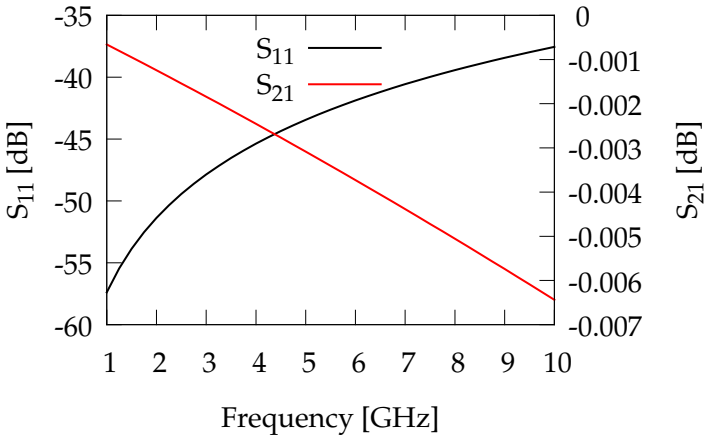

Figure 2.28: The scattering parameters of the CPW used for exciting samples showing both the reflection (S_{11}) and transmission (S_{21}). Data obtained by calculation with Sonnet Lite.

Because Sonnet Lite can also calculate the current density, it is possible to estimate the magnetic field induced by the RF current. To this end, we wrote a small piece of software to perform the necessary calculations. To calculate the magnetic field, we made the assumption that every cell used in the calculation of the current distribution is a current carrying conductor. This is sketched in Fig. 2.29.

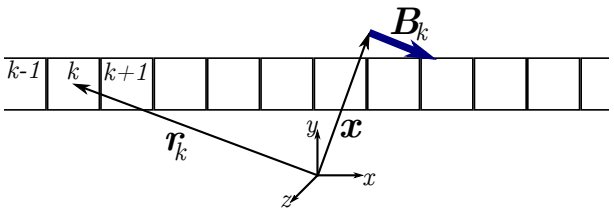

Figure 2.29: The scheme to calculate the magnetic field induced by the microwave current flowing through a coplanar waveguide. Each of the cells used for the RF simulation is considered as a current carrying wire. The total magnetic field is then equal to the sum of all the induced magnetic fields.

The total magnetic field is then equal to the sum of the magnetic fields

induced by each cell, i.e. a discrete version of the Biot-Savart law:

$$\mathbf{B}(\mathbf{x}) = \sum_{k} \frac{\mu_0 i_k}{2\pi r_k} \frac{(\mathbf{x} - \mathbf{r}_k) \times \mathbf{e}_z}{|\mathbf{x} - \mathbf{r}_k|}. \tag{2.48}$$

In this equation i_k is the current in each cell.
The position of each cell ($\mathbf{r}_k$) is taken at its centre. The magnetic field was calculated for positions ($\mathbf{x}$) that were always half the thickness h above the CPW.
The result of the calculation is shown in Fig. 2.30.

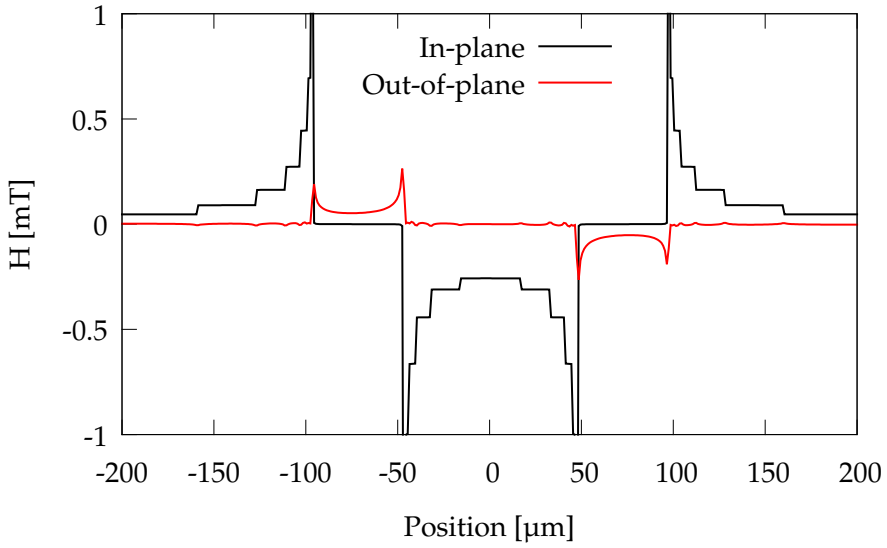

Figure 2.30: The peak magnetic field induced by current flowing through a CPW of 100 μm wide, 50 μm gap, with an applied power of 10 mW. The discontinuities are from the discretisation by the EM software used for calculating the current distribution and are not physical. The peaks on the other hand are physical and the result of the fact that the current flows mostly at the edges of the conductors.

Several conclusions be drawn from this. First of all, the out-of-plane component is negligible with respect to the in-plane field. This is explained by the fact that the current flows under the sample, yielding a strong in-plane component due to the small separation ($\mathbf{r}_k - \mathbf{x}$). Symmetry does not allow for an out-of-plane component on top of the centre conductor. This is because there flow two almost equal currents to the left and to the right

of these positions, and their respective out-of-plane magnetic fields cancel out.
In the gap, the current is now asymmetric due to the fact that the ground currents are opposed to the current in the centre conductor. Therefore, no in-plane field is present and the out-of-plane field is now largest. However, due to the large separation from the edges of the conductors, the out-of-plane field is rather small. Secondly, the in-plane magnetic field peaks at the edges of the conductors. This is explained due to the fact that the current mostly flows at the edges.

Chapter 3

Uniform precession of magnetisation in a confined geometry

In this chapter we will have an in depth look at the uniform precession (UP) of magnetisation in a Permalloy disc several tens of microns in diameter. UP measurements have been applied for many years to determine and study basic material parameters, such as saturation magnetisation, magnetocrystalline anisotropy, etc. and thus serves as a sort of benchmark for our method. I.e. would our newly developed set up, described in the previous chapter, yield usable results, it should be able to measure linewidths and resonance frequencies of the uniform precession.
Moreover, the basic principles of UP are well understood. This allows a direct comparison between theoretical values and the experimentally recorded data. As we rigorously derived a signal to noise ratio in the preceding chapter, this can now be experimentally validated.

3.1 Introduction

Fig. 3.1 shows an early measurement of UP in thin magnetic films. This measurement was made by Griffiths[44]. He made use of a microwave resonant cavity, where the bottom wall was replaced by a thin film, made from a ferromagnetic material (Supermalloy; 75%Ni, 20%Fe, 5%Mo). As

the RF magnetic field is most intense at the walls of a cavity, the magnetic absorption was maximised in this way. The result of their measurement is shown in Fig. 3.1.

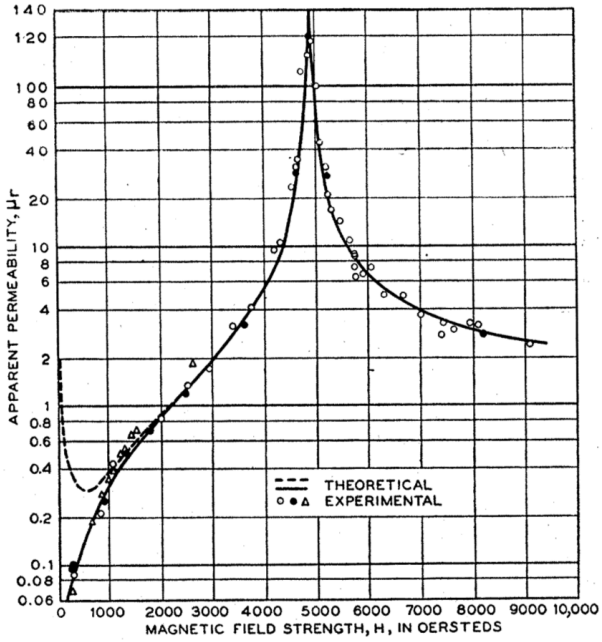

Figure 3.1: An early FMR spectrum on a magnetic thin film. The sample under investigation is from Supermalloy. Reproduced from [45]

Kittel later developed a theoretical framework[46].
We shall now show how the resonance frequency and the angle that the magnetisation will tilt out-of-plane, can be derived for an infinite thin film, Because we are dealing with uniform precession, the magnetisation is equal at all points, i.e. $\boldsymbol{M}(\boldsymbol{x}) = \boldsymbol{M}$.
We define the plane of the film to be the xy-plane, with the external bias field parallel to the x-axis. Therefore all components of the demagnetisation tensor, $\bar{\bar{\mathcal{N}}}$, are zero except:

$$\mathcal{N}_{zz} = 1. \tag{3.1}$$

This enables us to write the effective field as follows:

$$\boldsymbol{H}_{eff} = H_0 \boldsymbol{e}_x + H_{RF}(t)\boldsymbol{e}_y - M_z \boldsymbol{e}_z, \tag{3.2}$$

with H_0 the biasing field, $H_{RF}(t)$ the high frequency alternating field used as excitation and M_z the out-of-plane component of the magnetisation. The LLG,

$$\frac{d\mathbf{M}}{dt} = -\gamma\mu_0\mathbf{M}\times\mathbf{H}_{eff} + \frac{\alpha}{M_s}\left(\mathbf{M}\times\frac{d\mathbf{M}}{dt}\right), \tag{3.3}$$

can thus be written as[1]:

$$\dot{M}_x = 0 = \frac{\alpha}{M_s}\left(M_y\dot{M}_z - M_z\dot{M}_y\right), \tag{3.4}$$

$$\dot{M}_y = -\gamma\mu_0\left(M_s + H_0\right)M_z - \frac{\alpha}{M_s}(M_s\dot{M}_z), \tag{3.5}$$

$$\dot{M}_z = -\gamma\mu_0\left(M_sH_{RF}(t) - M_yH_0\right) + \frac{\alpha}{M_s}(M_s\dot{M}_y). \tag{3.6}$$

In deriving these equations we have made the approximation $M_x = M_s$ and that terms of the second order in either $H_{RF}(t)$, M_y or M_z are negligible. We make the following ansatz about the solution for M_y and M_z:

$$M_y = C\exp\{-i\omega t\}, \tag{3.7}$$

$$M_z = C'\exp\{-i\omega t\}, \tag{3.8}$$

where ω is the angular frequency of the excitation field, i.e. $H_{RF}(t) = H_p\sin(\omega t)$. As one can see, these solutions fulfil Eqn. (3.4). For simplifying further derivation, we now introduce the following variables:

$$\omega_M = \gamma\mu_0M_s, \tag{3.9}$$

$$\omega_H = \gamma\mu_0H_0. \tag{3.10}$$

We can rewrite Eqns. (3.5) and (3.6) into:

$$i\omega M_y = -(\omega_M + \omega_H)M_z + i\omega\alpha M_z, \tag{3.11}$$

$$i\omega M_z = -\omega_MH_{RF}(t) + \omega_HM_y + i\omega\alpha M_y. \tag{3.12}$$

Rearranging the terms gives us:

$$\begin{bmatrix} 0 \\ H_{RF}(t) \end{bmatrix} = \frac{1}{\omega_M}\begin{bmatrix} -i\omega & \omega_M + \omega_H - i\alpha\omega \\ \omega_H - i\alpha\omega & i\omega \end{bmatrix}\begin{bmatrix} M_y \\ M_z \end{bmatrix} \tag{3.13}$$

However, we are more interested in the susceptibility, $\bar{\bar{\chi}}$:

$$\mathbf{M} = \bar{\bar{\chi}}\mathbf{H}, \tag{3.14}$$

[1] At this point we introduce the shorthand notation $\dot{x} = \frac{dx}{dt}$

where both $\mathbf{M}$ and $\mathbf{H}$ are dynamical terms. Therefore we invert Eqn. (3.13) to obtain:

$$\bar{\bar{\chi}} = \omega_M \begin{bmatrix} -i\omega & \omega_M + \omega_H - i\alpha\omega \\ \omega_H - i\alpha\omega & i\omega \end{bmatrix}^{-1} \tag{3.15}$$

$$= \frac{\omega_M}{\Delta} \begin{bmatrix} i\omega & -\omega_M - \omega_H + i\alpha\omega \\ -\omega_H + i\alpha\omega & -i\omega \end{bmatrix}, \tag{3.16}$$

with

$$\Delta = (1+\alpha^2)\omega^2 - \omega_H(\omega_H + \omega_M) + i\alpha\omega(2\omega_H + \omega_M). \tag{3.17}$$

This equation can be simplified with the assumption that $1 + \alpha^2 \approx 1$ and the definition that $\omega_R^2 = \omega_H(\omega_H + \omega_M)$.
The susceptibility diverges when $\omega = \omega_R$, which can be identified as the Kittel equation for the resonance frequency of a uniform precession. The more familiar form being:

$$f = \frac{\gamma\mu_0}{2\pi}\sqrt{H_0(H_0 + M_S)}. \tag{3.18}$$

As our set up can measure dynamics using the polar Kerr effect (i.e. measure Δm_z), our interest goes out to the perpendicular component of the $\bar{\bar{\chi}}$ tensor, i.e. $\chi_\perp$. Using the above equations, one can show that this is equal to

$$\chi_\perp = -\frac{i\omega_M\omega}{\Delta}, \tag{3.19}$$

with real and imaginary components

$$\mathfrak{Re}\{\chi_\perp\} = \frac{-\alpha\omega_M(2\omega_H + \omega_M)\omega^2}{(\omega^2 - \omega_R^2)^2 + \alpha^2\omega^2(2\omega_H + \omega_M)^2}, \tag{3.20}$$

$$\mathfrak{Im}\{\chi_\perp\} = \frac{-\omega_M(\omega^2 - \omega_R^2)\omega}{(\omega^2 - \omega_R^2)^2 + \alpha^2\omega^2(2\omega_H + \omega_M)^2}. \tag{3.21}$$

$$\tag{3.22}$$

Of interest to us is the magnitude of this susceptibility as this is related to the experimentally observable out-of-plane magnetisation:

$$|M_z| = |\chi_\perp| H_{RF}(t), \tag{3.23}$$

$$= H_{RF}(t)\frac{\sqrt{\alpha^2\omega_M^2(2\omega_H + \omega_M)^2\omega^4 + \omega_M^2(\omega^2 - \omega_R^2)^2\omega^2}}{(\omega^2 - \omega_R^2)^2 + \alpha^2\omega^2(2\omega_H + \omega_M)^2} \tag{3.24}$$

For the parallel component, the calculation is completely analogous. For brevity it has been withheld. Both are plotted in Figs. 3.2 and 3.3. Several interesting observations can be made and intuitively understood.

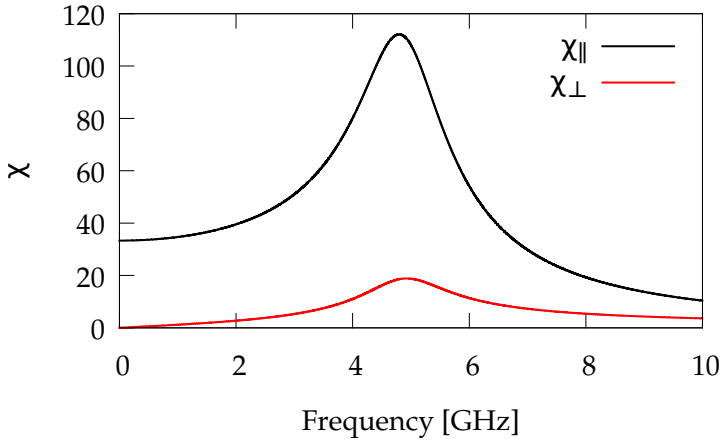

Figure 3.2: The AC susceptibility for an infinite thin film when the excitation is in-plane, orthogonal to the bias field. Both the in-plane (parallel to the excitation) as out-of-plane susceptibility are shown. In this case the bias field is kept constant and the frequency is swept. Parameters are as follows: $\alpha = 0.05, H_0 = 0.03\,\mathrm{T}, M_s = 1\,\mathrm{T}$

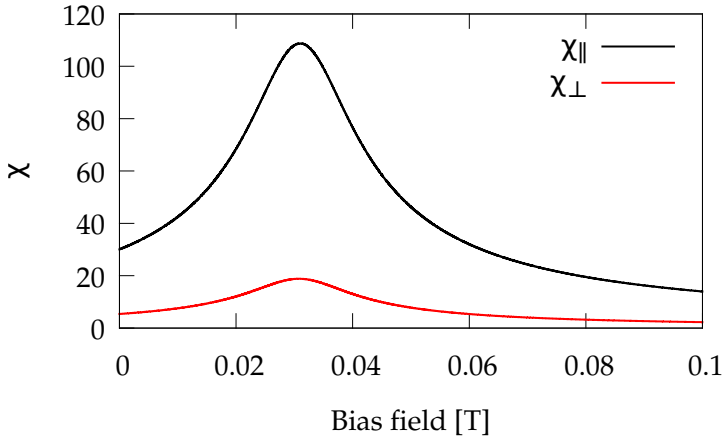

Figure 3.3: Exactly the same as Fig. 3.2, but now the bias field is swept and the excitation frequency is kept constant. Parameters are as follows: $\alpha = 0.05, f = 5\,\mathrm{GHz}, M_s = 1\,\mathrm{T}$.

For our brief discussion, we will limit ourselves to the susceptibility when the frequency is swept. Most obvious here is the fact that the $\chi_{||}$ is much larger then the out-of-plane component. This is due to the demagnetisation field, forcing the magnetisation to remain in-plane. At low frequency and down to a static field, $\chi_{||}$ approaches a constant, i.e. the magnetisation is (quasi) statically displaced by the excitation field. $\chi_{\perp}$ however goes to zero, as is expected. Though not completely clear from the graph, at high frequencies, exactly the opposite happens. $\chi_{\perp}$ approaches a constant values and $\chi_{||}$ goes to zero. There is a clear analogy between $\chi_{||}$ and the displacement of a damped harmonic oscillator.
At resonance ($\omega = \omega_R$), Eqn. (3.24) simplifies to

$$|M_z| = \frac{\omega_M}{\alpha(2\omega_H + \omega_M)} H_{RF}(t), \tag{3.25}$$

$$= \frac{M_s}{\alpha(2H_0 + M_s)} H_{RF}(t). \tag{3.26}$$

This equation will allow us to relate the maximum of the experimentally measured spectrum with the intrinsic damping, as will be used later.

3.2 Samples

The samples consisted of thin Permalloy discs on top of the centre conductor of a Au CPW, as described in Sect. 2.5.
Typically, we would excite the sample with 10 mW of power, which in a 50 Ω system would correspond to a peak current of 20 mA. It follows from Fig. 2.30 that the induced in-plane magnetic field is approximately 0.25 mT. If we apply a bias field of 30 mT, the susceptibility derived in the previous section (Eqn. 3.26) would give an out-of-plane magnetisation of 0.023T for Permalloy (with typical parameters $M_S = 1$ T, $\alpha = 0.01$). This would correspond with a precession cone where the magnetisation turns 1.4 ° out-of-plane. If we compare this value with the detection limit, derived in Sect. 2.4.5, we see that this should be measurable.
The width of the centre conductor places an upper limit on the diameter of the discs and the question arises how representable a finite disc (e.g. a 20 µm diameter, 20 nm thick disc), is for an infinite film. To answer this question we performed micromagnetic simulations with mumax3 ([9]). We used 4096x4096x1 cells, entailing a cell size of approximately 5x5x20 nm^3.

The magnetisation was initialised to a uniform state, with magnetisation parallel to the external (static) bias field of 10 mT. The system then was allowed to relax, the result of which is shown in Fig. 3.4.

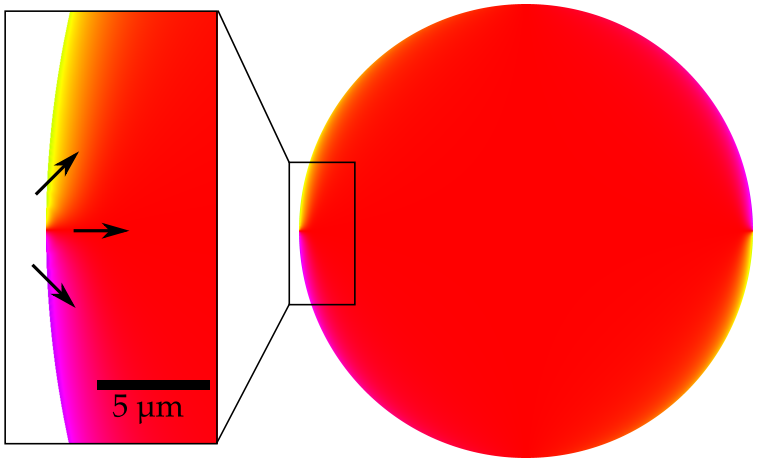

Figure 3.4: The ground state of a Permalloy disc of 20 µm diameter, with an applied magnetic of 10 mT parallel to the x-axis. At the edges, the magnetisation tilts in order to minimise the demagnetisation field. The magnification illustrates this effect (the arrows indicate the direction of the magnetisation).

The system does not relax to a uniform state, but there are edge effects that come into play. The question is how much impact these have. To resolve this issue, the relaxed state was excited with an in-plane pulsed magnetic field (i.e. $B_x \propto \sin(\omega t)/(\omega t)$). Afterwards, it relaxes by oscillating at its resonance frequency.

A Fourier Transform of the out-of-plane magnetisation taken during the oscillation then yields the resonance frequency. In order to be able to compare to our experimental measurements directly, we defined a 1 μm^2 area at the centre and recorded the time behaviour of the spatially averaged magnetisation in this area. The result of this simulation and the comparison with the Kittel equation (for an infinite film, Eqn. 3.18) is shown in Fig. 3.5. It follows from the graph that the UP is the dominant resonance in the spectrum.

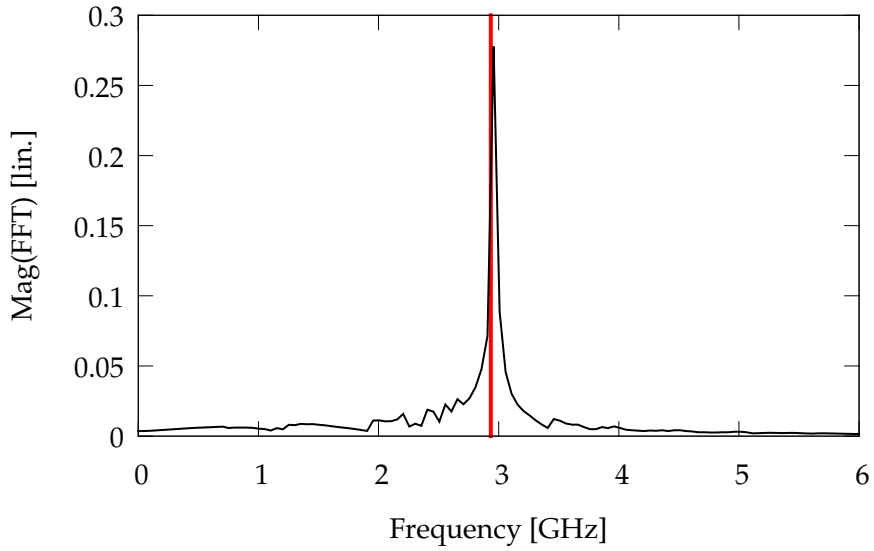

Figure 3.5: The simulated response of a 20μm Permalloy disc with an applied bias field of 10 mT. The red line indicates the position of the UP resonance of an infinite thin film calculated with the Kittel equation, Eq. 3.18. It follows that the UP is the dominant feature in the spectrum. Because the detection in our experimental set up is not phase synchronous with the excitation, we measure the magnitude of the response and Mag(FFT) is shown.

From this, we can conclude that the effects at the edges do not matter for the uniform precession.

3.3 Experiments

We will now examine the experimental results and see what we can learn about the experimental technique from these. To this end, we will compare field and frequency swept measurements and see how reproducible the results are. Likewise, we will take a look at the linewidths that follow from the measurements.

3.3.1 Field swept spectra

One of the first experiments was sweeping the magnetic field between 0 and 40 mT, whilst the sample was excited at 4 GHz with 7 dBm of power. The result is shown in Fig. 3.6, where we have plotted the RMS averaged

out-of-plane magnetisation $\langle m_z \rangle$. It can be shown that this proportional to the linear signal-to-noise ratio (snr), which in turn is partially calibrated for frequency dependent effects of the signal chain. A Lorentz curve has been fitted to the measured curve, yielding a resonance field of $20.63 \pm 0.12\,\mathrm{mT}$ and a FWHM of $1.45 \pm 0.18\,\mathrm{mT}$. This corresponds to a saturation magnetisation of $M_S = 0.970 \pm 0.006\,\mathrm{T}$, found through the application of the Kittel equation. It can be shown that the FWHM is related to the damping factor through:

$$\alpha = \frac{\gamma \Delta H}{4\pi f}, \tag{3.27}$$

in our case yielding a damping factor of $\alpha = 0.005$.

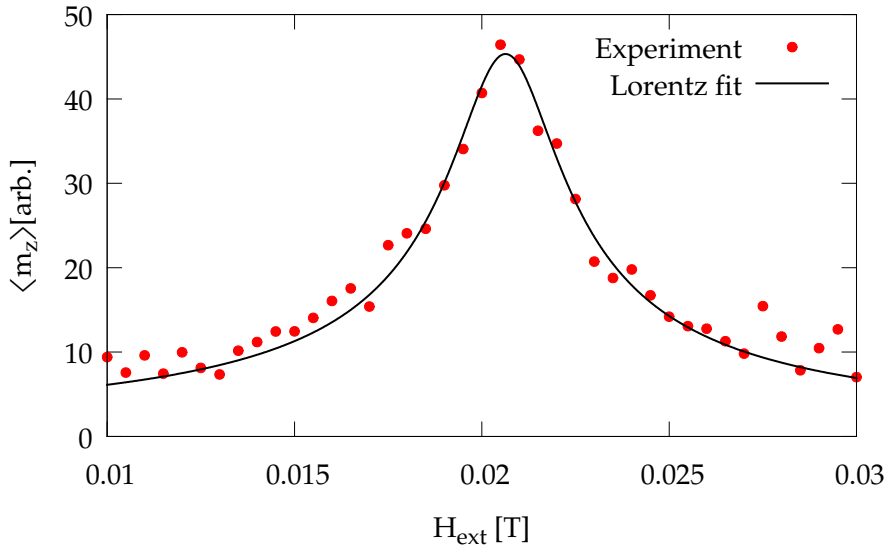

Figure 3.6: First measurement of the UP response. Measurement performed at a fixed frequency of 4GHz.

Measurements of the signal at the end of the chain are hard to relate to values of Δm_z, due to the frequency dependence of the conversion efficiency as discussed in Sect. 2.4.6. However, our rigorous derivation of SNR in Sect. 2.4.5, shows that the SNR is directly related to the out-of-plane magnetisation. Inverting Eqn. 2.46, neglecting all other terms than the Johnson noise, yields

$$\Delta m_z = \frac{\sqrt{\mathrm{snr} \cdot 4Bk_BT/R_{\mathrm{Term}}}}{2I_{\mathrm{DC}}\theta_K}, \tag{3.28}$$

where snr is the linear signal to noise ratio and Δm_z the maximum excursion of the out-of-plane magnetisation. Care has to be taken that we use the SNR at start of the chain, which is about 3 dB more than at the measured value, due to noise added by the chain itself. For the value in Fig. 3.6 we find an excursion of $\Delta m_z = 0.0098 \pm 0.0006$. The error was estimated by error propagation of the statistic error of the snr by fitting it to a Lorentz curve. Thus, systematic errors are not taken into account.

This can then be combined with the out-of-plane susceptibility of Eqn. 3.26 to provide an estimate of the damping factor, α, without measuring the linewidth:

$$\alpha = \frac{H_{max}}{\Delta m_z (2H_0 + M_S)}. \tag{3.29}$$

The peak magnetic field at 7 dBm is estimated to be 180 μT, which yields a damping factor of $\alpha = 0.01$. If we compare this value with the value obtained from the linewidth (0.005), we see that the two roughly agree. Taking into account the numerous approximations this result is quite satisfying.

3.3.2 Frequency swept spectra

Before proceeding to more systematic studies, we will first turn our attention to spectra where the field is kept constant, but the frequency of the excitation is swept. To this end, the same sample as used in the previous section, is biased with a fixed field of 20 mT. The result is shown in Fig. 3.7.

In comparison with Fig. 3.6, we see that $\langle m_z \rangle$ shows much greater fluctuations. The most probable explanation for this effect is that the correction for conversion efficiency is not perfect and leaves residual traces in the final result.

The signal was again fitted to a Lorentz curve, yielding a resonance frequency of 3953 ± 9 MHz with a linewidth of 73 ± 12 MHz. This corresponds with a saturation magnetisation of 0.977 ± 0.006 T, which is compatible with the value found when the field was swept.

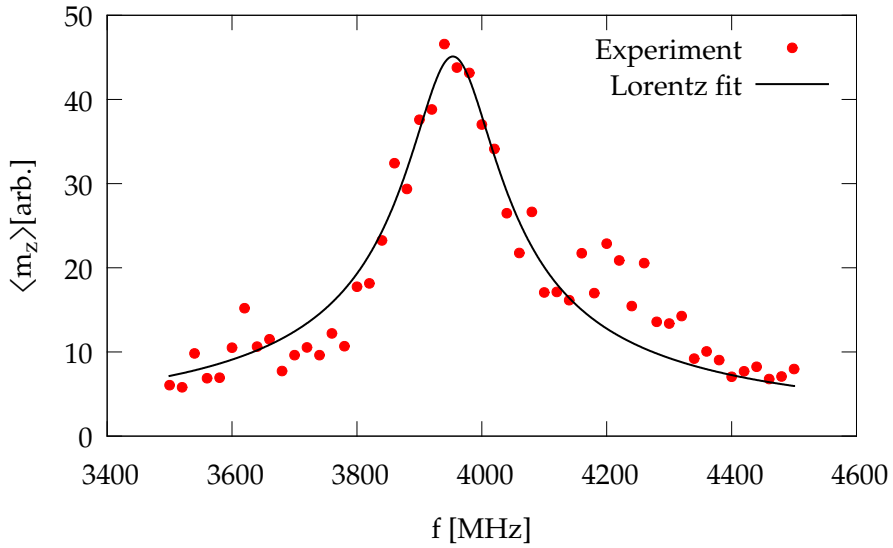

Figure 3.7: First measurement of the UP response, in the frequency domain. Measurement performed at a fixed bias field of 20mT.

The linewidth in frequency domain Δf is related to the linewidth in field domain by[19]:

$$\Delta H = \frac{2\pi\Delta f}{\gamma P(f_{res})}, \tag{3.30}$$

with

$$P(f) = \sqrt{1 + \left(\frac{\gamma M_s}{4\pi f}\right)^2}. \tag{3.31}$$

These equations can be combined with Eqn. 3.29, resulting in

$$\alpha = \frac{\Delta f}{2 f_{Res} P(f_{Res})}. \tag{3.32}$$

The linewidth measured in frequency domain of 73 MHz would thus correspond with a linewidth of 1.2 ± 0.2mT in field domain. This corresponds with a damping of approximately $\alpha = 0.004$. The comparison has been summarised in Table. 3.1.

Table 3.1: The comparison between field and frequency swept spectra

	Field meas.	Frequency meas.
M_S	$0.970 \pm 0.006\,T$	$0.977 \pm 0.006\,T$
ΔH	$1.6 \pm 0.2\,mT$	$1.2 \pm 0.2\,mT$
α	0.005 ± 0.001	0.004 ± 0.001

Measurements were performed with a magnetic field between 20 mT and 45 mT (the upper limit of our electromagnet). First the sample was biased with a specific magnetic field and then the frequency of the excitation was scanned to find the resonance.
The frequency and linewidth of these resonances were determined by fitting a Lorentz curve to the spectra. The Kittel equation was fitted to the measured resonance frequencies, resulting in an estimate for the saturation magnetisation of $M_S = 0.994 \pm 0.005\,T$. The experimental points are compared to the fitted curve in Fig. 3.8.

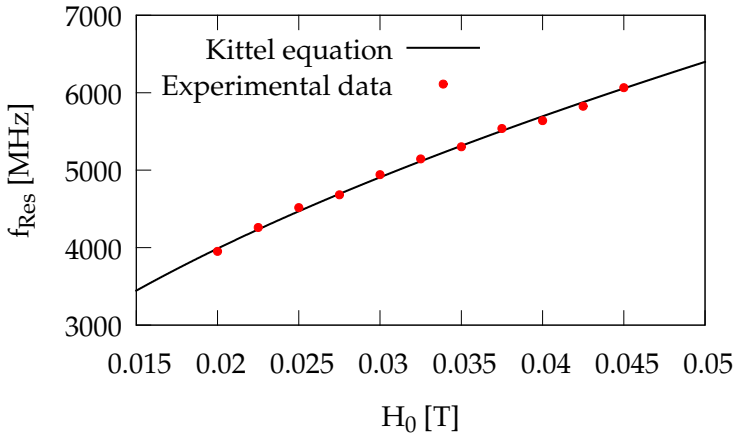

Figure 3.8: The resonance frequency in function of applied field. The fit to the Kittel equation results in a value of $M_S = 0.994\,T$. The applied field is kept constant for each measurement point, whilst the frequency is swept to determine the resonance frequency.

By applying Eqn. 3.32 to the data, we can calculate the damping as a function of the frequency. For the uniform precession, the only contribution to the damping is the intrinsic material damping, so the value should remain

constant as the frequency is varied. The result is shown in Fig. 3.9.

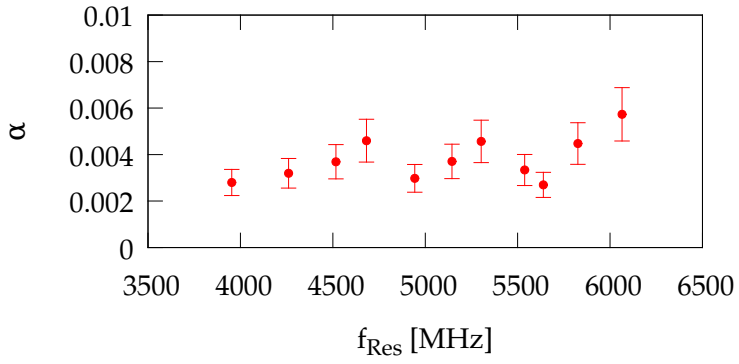

Figure 3.9: The damping as a function of the resonance frequency, swept frequency measurement.

Fig. 3.9 indicates that we probably underestimated the error on the linewidth, because the damping shown is very low (≈ 0.002). Uncalibrated frequency dependence of the excitation and detection can give rise to additional errors on the linewidth, because they distort the resonance curve. This gives rise to systematic errors which we can not take into account. It is interesting to compare this with measurements made by sweeping the magnetic field, as shown in Fig. 3.10.

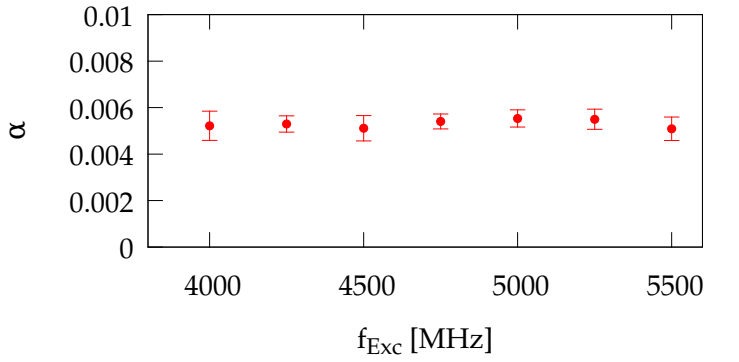

Figure 3.10: The damping as function of the resonance frequency, swept field measurement (i.e. fixed excitation frequency)

.

This type of measurements does not suffer from frequency calibration issues. Here, the damping has a reasonable value and shows no frequency dependence.

3.4 Measurement reproducibility

Finally, we turn our attention to the reproducibility of the measurement. A single measurement, as shown in Fig. 3.7, has some noise imposed on the trace, which does not necessarily equal the noise floor of the set up. Therefore, to estimate the uncertainty of the measurement curve, we should measure the same resonance a number of times and look at the spread of these measurements.
The result of such a measurement series is shown in Fig. 3.11, for both an applied field of 20 mT and 25 mT. The average value of five consecutive measurements is shown, with the error bars indicating the standard deviation. This figure shows that the curves are not pure Lorentzian in shape, but show skewing and posses some bumps. This would explain why the measurements of α in Fig. 3.9 are scattered over a rather broad range.

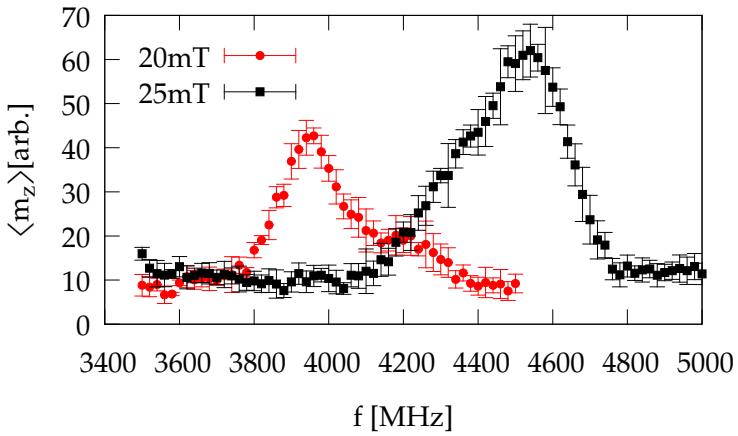

Figure 3.11: A UP resonance in the frequency domain, measured five times. Error bars indicate the standard deviation on these measurements. The applied bias field is indicated.

For an applied field of 22.5 mT, the effect is even stronger, as illustrated in Fig. 3.12. In this case the resonance curve appears to have obtained a shoulder-like feature. These features of the spectrum might be explained

as additional, non uniform modes. However, when we compare this with field swept measurements, the features do not appear.

When we compare $\langle m_z \rangle$ with the noise floor, which represents the conversion efficiency, we see that as the noise increases so does $\langle m_z \rangle$. Thus, incomplete compensation for the conversion efficiency of the signal chain might explain these features.

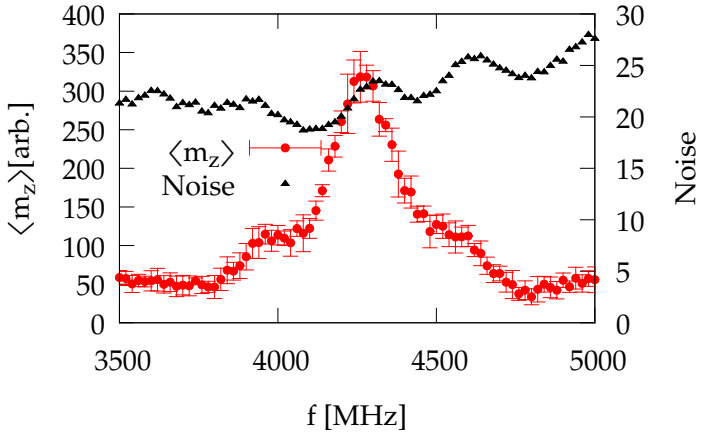

Figure 3.12: A UP resonance in the frequency domain, measured five times. Error bars indicate the standard deviation. 22.5 mT of bias field was applied.

We have compared both a field and frequency swept measurement, but we can do this for a number of fixed frequencies or fields. These should give comparable results. In Fig. 3.13 we compare the peak position of the field and frequency swept measurement. From this figure and the fitted values of M_S we see that these are compatible. Thus despite the incomplete correction of the frequency dependence, the position of the resonance curve can be determined with high accuracy.

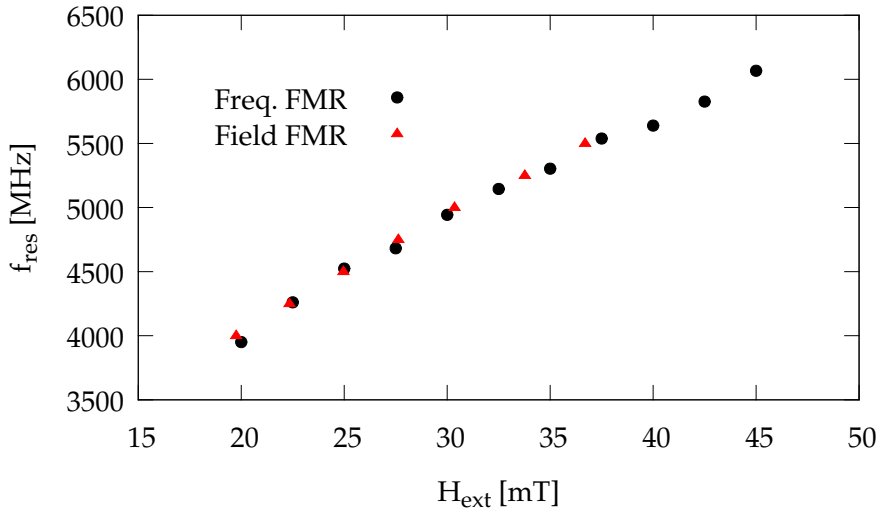

Figure 3.13: A comparison of the position of the UP resonance when either the field is swept (constant frequency) or the frequency is swept (constant field). $M_S = 0.994 \pm 0.015$T for frequency sweeps, and $M_S = 1.013 \pm 0.006$T for field sweeps.

3.5 Conclusion

We have seen that our newly developed method allows to quantitatively determine resonance positions and extract the saturation magnetisation. The resonance position can be determined in either field or frequency domain, both giving rise to the same saturation magnetisation, as shown in Fig. 3.13.

Measurements of the linewidth, made by sweeping the excitation frequency, are somewhat more difficult and less accurate. The fact that the measured curves are not perfect Lorentzian in shape is probably due to incomplete frequency compensation. When sweeping the magnetic field instead, this problem is overcome and reasonable values of the damping are found.

Chapter 4

Radial spin wave modes in thin magnetic platelets

In this chapter we will discuss the various excitations of a nano magnet with a vortex ground state magnetisation. More specifically we will study the lowest order radial spin wave (RSW). Part of this work has been published in [47].

As explained in the first chapter, for thin film (thickness $\approx l_{exch}$) squares and discs with comparably large lateral dimensions ($R \gg l_{exch}$) , the ground state is no longer a single domain state, but a Landau or vortex state. These are identified by two parameters: their circulation (clockwise or counter clockwise) and polarisation (up or down). As a result, each element can be in any of four different states, in principle enabling the storage of two bits per element, as illustrated in Fig. 4.1.

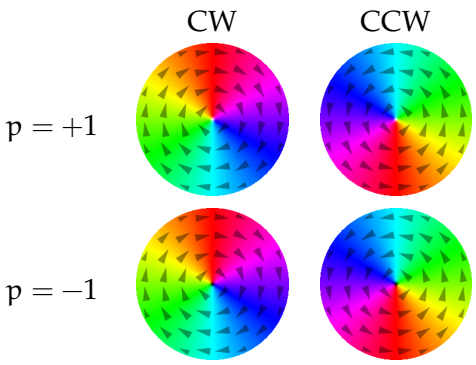

Figure 4.1: The four possible configurations of the vortex ground state in a magnetic disc. p indicates the polarisation of vortex core, either $+z$ or $-z$. The circulation specifies in which direction the in-plane magnetisation is curled. The arrows indicate the direction of the local magnetisation $\mathbf{m}$.

4.1 Introduction

The vortex ground state has several modes of excitation, the one with the lowest frequency is the gyration of the vortex core.
When the vortex core is displaced from the centre, it starts to precess around the centre of the disc. The driving force behind this oscillation is the demagnetising field. When the core is displaced, flux closure is not complete and a demagnetising field is created. The vortex relaxes back to its original ground state by spiralling towards the centre, i.e. «*gyrating*».

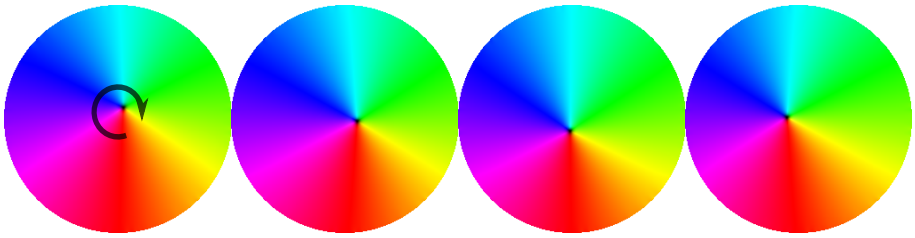

Figure 4.2: Vortex gyration illustrated for a 50 nm thick, 1 µm disc of Permalloy. In this case the gyration frequency was 410 MHz.

Analytically, this motion is described by Thiele's equation[48, 49]:

$$\mathbf{G} \times \frac{d\mathbf{X}}{dt} - \frac{dW(\mathbf{X})}{d\mathbf{x}} = 0, \tag{4.1}$$

where $\mathbf{X}$ is the position of the vortex core, $W(\mathbf{X})$ the potential in which it moves (i.e. carrying contributions from exchange, demagnetising and Zeeman fields) and $\mathbf{G}$ the «*gyrovector*». It can be calculated in the general case by applying the following equation:

$$\mathbf{G} = \frac{M_S L}{\gamma} \int d^2\boldsymbol{\rho} \sin\theta(\nabla\phi \times \nabla\theta), \tag{4.2}$$

where $\phi(\boldsymbol{\rho})$ is the azimuthal angle of the magnetisation at a certain position of the unit sphere ($\boldsymbol{\rho}$) surrounding the configuration of interest, and $\theta(\boldsymbol{\rho})$ the polar angle. The integration is taken over the entire unit sphere. Though the magnetisation can be dynamic, it can be shown that the gyrovector remains constant if no switching of the vortex core polarisation takes place. For a vortex state it is given by[50]:

$$\mathbf{G} = -2\pi q p \boldsymbol{e}_z. \tag{4.3}$$

p indicates the vortex core polarisation associated with the vortex: $p = +1$, the core has positive m_z and $p = -1$, negative vortex core polarisation. q is positive (i.e. +1) for vortices and negative (-1) for anti-vortices. The difference between the two is shown below in Fig. 4.3. The gyrovector thus represents a topological quantity.

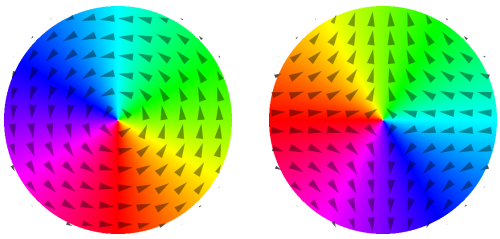

Figure 4.3: Shown is the difference between a vortex (left) and anti-vortex (right)

The gyrotropic mode, shown in Fig. 4.2, is the lowest mode in frequency and is typically found below 1 GHz in Permalloy, depending on the aspect ratio of the disc. It can be excited using an in-plane, oscillating magnetic field or spin polarised current[51]. When pumped with sufficient excitation, it can lead to the switching of the vortex core polarisation. This happens through the formation of a vortex/anti-vortex pair, where the anti-vortex annihilates with the original vortex core[51, 23].
When excited with a linear in-plane magnetic field (i.e. $\mathbf{B}(t) = B_0 \cos(\omega t)\boldsymbol{e}_x$) the core can switch from either state (i.e. core up or down), enabling the

back and forth switching of the polarisation. However, when excited with a rotating in-plane field (i.e. $\mathbf{B}(t) = B_0 \cos(\omega t)\mathbf{e}_x + B_0 \sin(\omega t)\mathbf{e}_y$), this symmetry is broken. This enables selectively switching from one to the other state. Experimentally this has been observed by Curcic *et al.*[52], as switching was only seen when the sense of gyration (proportional to the polarisation) was the same as the sense of the rotating magnetic field.

Another class of excitation modes are azimuthal spin wave modes. In contrast to the vortex gyration mode, these leave the position of the vortex core unperturbed. Instead, the out-of-plane magnetisation becomes a function of the azimuthal angle. To excite these modes (in a disc), an in-plane rotating magnetic field, oscillating at several GHz, is applied.

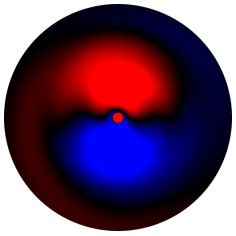

Figure 4.4: Shown is the out-of-plane magnetisation (m_z) of a 1 µm 10 nm thick disc, excited at the resonance frequency of the lowest order azimuthal spin wave (6.4 GHz). Red corresponds to $m_z = -0.01$, blue with $m_z = 0.01$ and black with $m_z = 0$.

Again, when the disc is pumped at resonance, the azimuthal spin wave can induce switching of the vortex core polarisation, mediated by vortex/anti-vortex formation as described by Kammerer *et al.*[24]. The azimuthal wave mode can rotate either clockwise (CW) or counter clockwise (CCW), and these could be degenerate modes. The interaction with the vortex ground state lifts this possible degeneracy however. This means that for a given excitation (CW or CCW) there are two possible resonance frequencies, depending on the vortex core polarisation.

Because this degeneracy is lifted, switching can be selective. For a given excitation frequency, a core can only be switched if the sense of rotation of the excitation matches with the core polarisation. Should they match and switching occurs, they do not match afterwards, effectively eliminating further switching. This is illustrated in Fig. 4.5.

To obtain these results, the authors used the TR-STXM method and ap-

plied bursts of RF with either CW or CCW sense of rotation. This way they scanned over a region of the parameter space (B_{ext}, f_{exc}, circulation of excitation) and verifying whether or not a vortex would change polarisation.

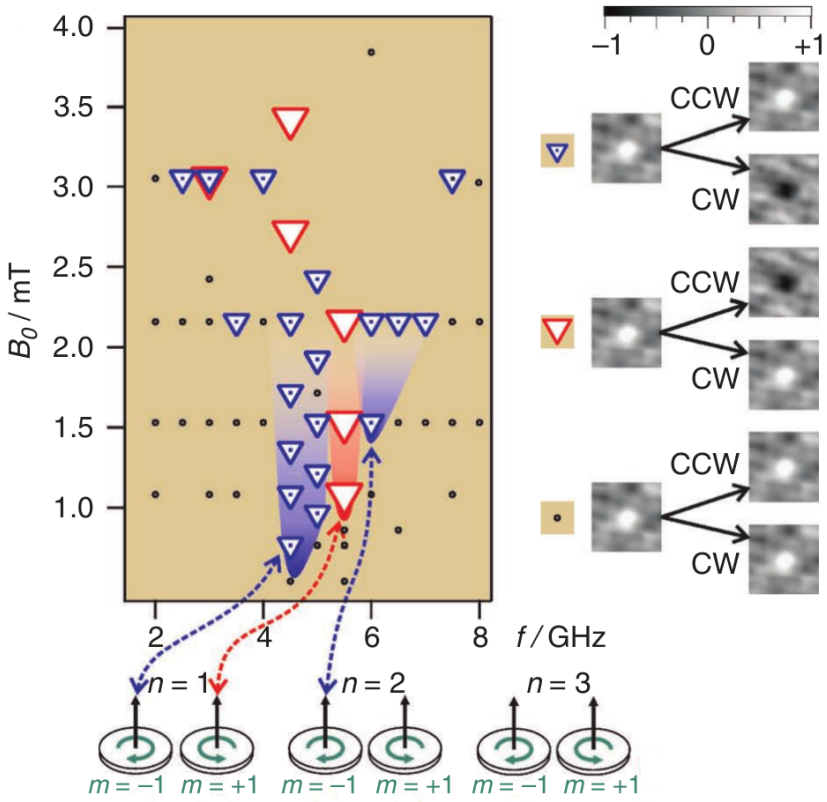

Figure 4.5: Shown is the experimental switching diagram for azimuthal spin-waves, showing selective switching. On the right are shown the transitions from an up-core for a constant excitation frequency. Reproduced from Kammerer *et al.*[24]

4.1.1 Radial spin waves

The last class of excitations is formed by radial spin waves (RSWs), where the out-of-plane magnetisation is now solely a function of the distance to the centre. These spin waves can only be excited using an out-of-plane oscillating field (at a frequency of at least several GHz). The first four even modes are shown in Fig. 4.6.

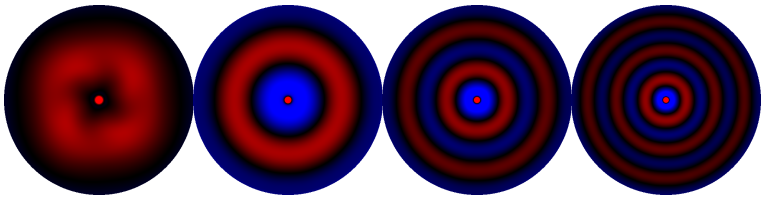

Figure 4.6: Shown is the out-of-plane magnetisation of the first four even radial spin wave modes in a 1µm 10nm thick Permalloy disc. The excitation frequencies were (from left to right) 4.5 GHz, 7.5 GHz, 9.8 GHz and 11.7 GHz.

Giovannini *et al.*[53] were the first to present experimental results and micromagnetic simulations of the radial modes. The result of their BLS measurement (Brillouin Light Scattering, see Sect. 2.1) is shown in Fig. 4.7.

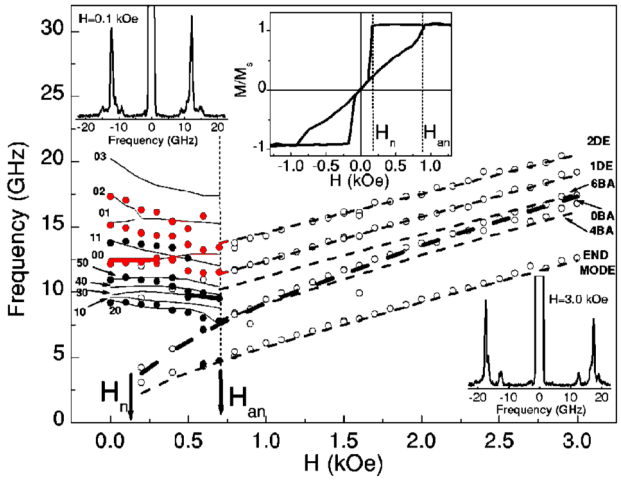

Figure 4.7: Experimental data of both azimuthal spinwaves and radial spinwaves (red symbols) obtained by BLS-spectroscopy on an array of Permalloy discs (100 nm radius, 15 nm thick) with an in-plane applied magnetic field. Shown is the resonance frequency of the modes in function of the applied magnetic field. The red symbols are the first three radial modes, the other symbols are azimuthal modes. The insets show the Brillouin splitting and hysteresis loop. H_n indicates the nucleation field (reintroduction of a vortex when lowering the external field) and H_{an} is the field at which the vortex core is removed from the disc. DE are Damon-Eshbach modes, BA are backward volume modes (both are discussed in Sect. 1.4.2 Reproduced from Giovannini *et al.*[53].)

In their paper the authors studied not only radial, but also azimuthal spinwaves both at remanence and with an in-plane applied field. To detect the modes they made a BLS-spectroscopy study of arrays of Permalloy discs (100 nm radius and 15 nm thick).

Buess *et al.* applied TR-MOKE to study both radial and azimuthal spin waves in Permalloy nano discs. They used samples that were 15 nm thick and had diameters of 3, 4 or 6 µm. These discs were placed inside a microcoil (shown in Fig. 4.8), through which a 100 ps wide pulse was sent. It was estimated by the authors that the pulse had an amplitude of 5 mT. The field was not homogeneous over the entire sample, but it was found by the authors that the field amplitude differed by 30% over the entire surface of the sample. Because of this strong inhomogeneity, they did not only excite azimuthal spinwaves, but found that these even inverted the core polarisation.

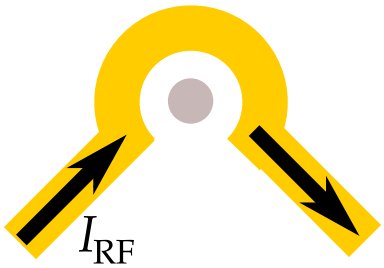

Figure 4.8: An illustration of a microcoil excitation structure. Though such a structure gives rise to strong out-of-plane fields, it has an inherently high field inhomogeneity and in-plane field due to the opening at the bottom.

After acquiring a time series of images of δm_z ($= m_z(t) - m_z(0)$), the authors performed a temporal FFT on the dataset. With a frequency resolution of 0.34 GHz (artificially lowered to 0.1 GHz through zero padding before applying the FFT) they were able to resolve the first three radial spinwaves. These are shown in Fig. 4.9.

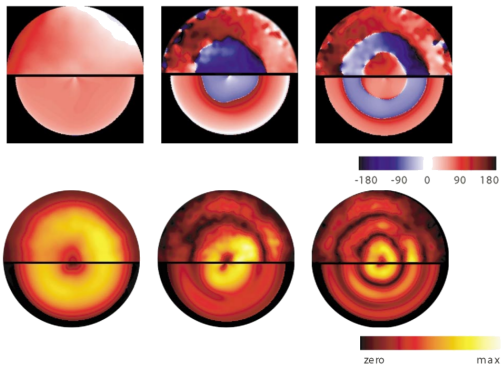

Figure 4.9: Shown are the three first radial spinwaves obtained by applying an FFT to a series of images obtained from a TR-MOKE experiment (top half of each image) for a 3 µm Permalloy disc. By comparison, the results from micromagnetic simulations are shown on the bottom half of each image. The series on the bottom is the magnitude, and on top is the phase. Reproduced from Buess *et al.*[54]

The dependence of the resonance position on aspect ratio was studied by Vogt *et al.*[55] using BLS. Their result is shown in Fig. 4.10.

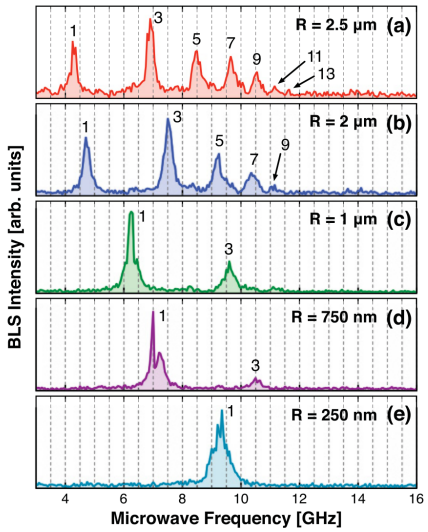

Figure 4.10: Shown are the experimental results of BLS-spectroscopy of Permalloy discs excited at a fixed frequency for different diameters. Each disc was 40 nm thick and placed in a microcoil. Reproduced from Vogt *et al.*[55]

They arrived at their results by combining measurements from BLS-spectroscopy with an analytic approach (based on the theoretical approach of Guslienko *et al.* discussed below). For their experimental work, they made use of discs with diameters between 250 nm and 2.5 μm, but all with the same thickness of 40 nm. These discs were placed in a microcoil through which an oscillating current was sent. The frequency of the latter was varied and the response of the discs studied using BLS-spectroscopy. They were able to measure up to the 13th radial mode.
Guslienko *et al.*[56] gave a theoretical treatment of these modes, on the assumptions that:

- They are of magnetostatic origin, due to the fact that they have a wavelength that is long in comparison with the exchange length;
- They are small perturbations of the magnetisation;
- The thickness of the discs (t) is of the order of the exchange length and the magnetisation is homogeneous along the thickness of the disc (z);
- The radius of these discs (R) is much larger than the exchange length, thus yielding an aspect ratio $\beta = t/R \ll 1$;
- The excitations are located outside the region of the vortex core and have no interaction with the latter.

The last point follows from the fact that vortex core is a very stable configuration, held together by the exchange coupling.
It can be shown that under these assumptions the problem becomes analytically tractable if we treat the dynamics as a small perturbation on the static magnetisation:

$$\mathbf{m}(r,t) = \mathbf{m}_0 + \boldsymbol{\mu}(r,t). \tag{4.4}$$

In this equation $\mathbf{m}_0$ is the static magnetisation, which lies completely in plane (except at the vortex) and has only a tangential component, i.e. $\mathbf{m}_0 = (0, m_0, 0)$ in cylindrical components $((e_r, e_\theta, e_z))$. $\boldsymbol{\mu}(r,t)$ is the small perturbation which has a negligible tangential component, i.e. $\boldsymbol{\mu}(r,t) = (\mu_r(r,t), 0, \mu_z(r,t))$. The time dependence of these factors is $\mu_r(r,t) \propto \sin(\omega t + \phi), \mu_z(r,t) \propto \cos(\omega t + \phi)$.

Using these assumptions it was shown that the frequency of the n-th radial mode is given by[56]:

$$\omega_n^2 = (\gamma 4\pi M_S)^2 \left(1 - \frac{1 - e^{\beta\alpha_n}}{\beta\alpha_n}\right), \tag{4.5}$$

where α_n is the n-th root of the first order Bessel function, J_1.
For the first order mode, we calculated the radial profile of the eigenmode, shown in Fig. 4.11, and the eigenfrequency to be 5.1 GHz for a 1 µm diameter, 10 nm thick Permalloy disc. This is comparable with the value of 4.5 GHz found by micromagnetic simulations (with M_S of 1 T).

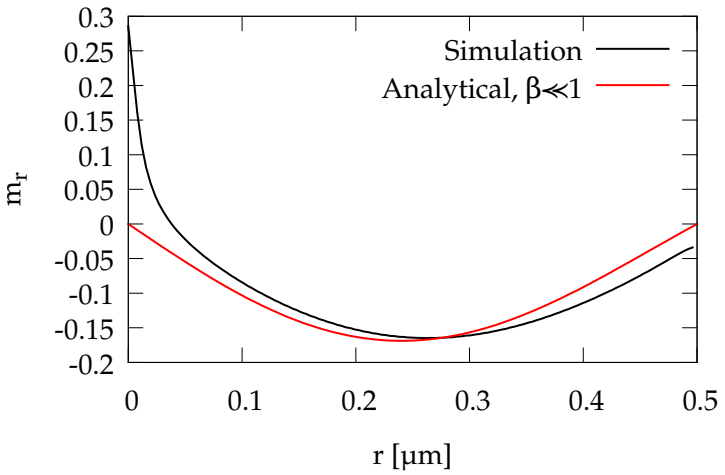

Figure 4.11: The radial component of magnetisation, m_r, in function of the radius for a 1 µm diameter, 10 nm thick disc for the lowest order radial mode. Shown is the comparison between the analytical solution[56] and results from micromagnetic simulations.

4.2 The STXM approach

In our first approach, we utilised the STXM-technique, which allows for direct imaging of these modes. It is expected that when the spin waves enter the non linear regime, they are not necessarily repetitive any more, but may perform some chaotic motion. This is confirmed by micromagnetic simulations. Because STXM can only reveal a repetitive pattern (see Sect. 2.2), no dynamics would be visible at all. Thus besides exciting the sample

with a continuous RF signal, we also used a burst pattern, which consists of repetitive packets of sine waves.

After each RF burst, the system can relax back to its ground state. The timing of the bursts has to be phase locked to the excitation. In this way, if the dynamics become chaotic we are still able to measure the (repetitive) dynamics until right before the onset of chaos.

Raw STXM data contains only the brightness of each pixel for each measurement channel (corresponding to a time), resulting in $\text{pixels}_x \cdot \text{pixels}_y \cdot$ channels values. It also contains an amount of crosstalk from the excitation. This is because the excitation is phase locked to the X-ray pulses, resulting in a possible direct coupling between the excitation and the detector (APD). The beam intensity is also not constant in time, but varies from bucket[1] to bucket. As a result, some of the channels will be brighter than others due to more electrons being present in a specific bucket.

Luckily, these issues can be resolved in post-processing when a small border of non-magnetic material is also visible in the frame. This can be used to normalise the intensity of all the frames. To obtain images from the raw data, software was written to process the data (using the GNU Scientific Library[57] and ImageMagick[58]). The procedure for going from raw data to images is described in Appendix A.

The dynamic images are obtained by calculating the average of all the channels and subtracting this from each channel, removing all static components.

To excite the radial spin waves, we need a very strong excitation field, preferable 10 mT and higher. But we also need this field to be as homogeneous as possible, to avoid exciting other modes. Therefore we need to optimise the excitation geometry (i.e. waveguide) and the amplifiers, which provide the RF current through the geometry.

For a conventional CPW (Fig. 4.12 (c)) it is only possible to increase the upper power limit by using two amplifiers, one at each end of the CPW, but with a phase difference of 180° between the two. This increases the limit of the total RF power at the sample to approximately $P_{1\,\mathrm{dB}} + 3\,\mathrm{dB}$, where $P_{1\,\mathrm{dB}}$ is the output power where the gain of the amplifier has lowered by 1 dB due to saturation. To overcome this limit, we used a differential pair (Fig. 4.12 (a)), which has no ground plane but instead a second conductor.

[1] A bucket is a single packet of electrons travelling around the synchrotron

This way the power limit is $P_{1\,dB} + 6\,dB$, or two times more, because one can use two more amplifiers. Though it is possible to generate higher fields this way, it requires a delicate balancing of the relative phase of each of the signals connected to four ends of the differential pair. The four coax cables connecting the sample with the amplifiers, need to be equal length within a margin of 40 mm. The three different types of excitation structures are shown in Fig. 4.12. We did not use a microcoil, because it was found by Buess *et al.*[54] that this geometry excites azimuthal spin waves.

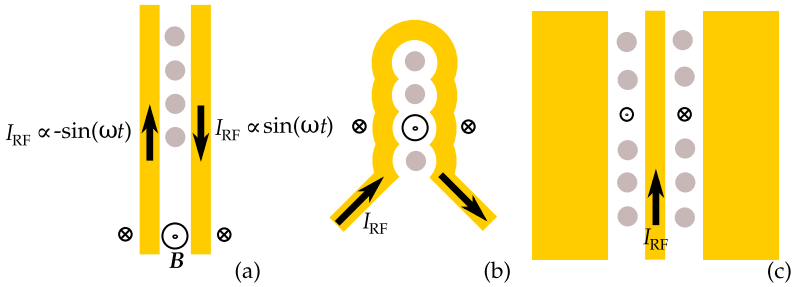

Figure 4.12: Three excitation structures: the differential pair (a), hairpin structure (b) and coplanar waveguide (c). Indicated are both the RF current and the magnetic field it induces. The discs indicate possible magnetic structures that need to be excited using an out-of-plane magnetic field.

Three snapshots of the out-of-plane magnetisation during the oscillation period are shown in Fig. 4.13. We see that the magnetisation turns out-of-plane uniformly over the surface, except near the vortex core.
Figure 4.13 apparently shows dynamics in the centre which is 180° out-of-phase with the rest. The question is if this a real phenomenon, or only an artefact of post-processing. To eliminate this ambiguity, we also measured a sample located in a hairpin structure (Fig. 4.12 (b)), shown in Fig. 4.14. This sample has an intrinsic mirror symmetry (in contrast to the differential pair, which requires manual tuning of the phase), thus ruling out any in-plane or inhomogeneous magnetic field. Again, this sample shows the same mode profile. Finally, micromagnetic simulations (with the same parameters as used for Fig. 4.20) indicate that the lowest order mode should be at 6.9 GHz and the next mode at 9.5 GHz. We can thus say with reasonable confidence that we were examining the lowest mode.
Despite being able to image the this mode, we were confronted with some

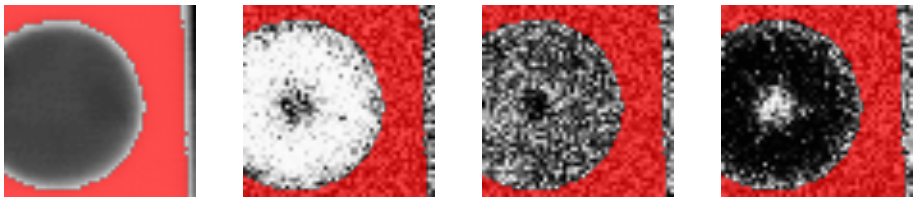

Figure 4.13: A series of STXM images, at the left a static image followed by a series of dynamic images showing m_z at three points of the oscillation. This is a 20 nm thick, 1 µm diameter Permalloy disc, excited at a frequency of 6016 MHz with 40 mW of RF power. The red area is used for normalisation and contains no magnetic material. The dynamic images are obtained by calculating the average of all the channels and subtracting this from each channel, removing all static components.

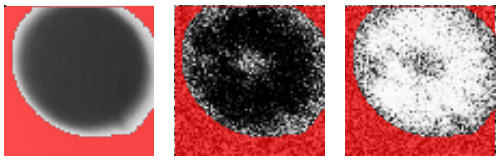

Figure 4.14: A static STXM image, as well as two dynamic images at the two ultimate points of the oscillation. This is for a 1 µm sample, 20 nm thick, located in a hairpin structure. This illustrates that the alternating centre as also found in Fig. 4.13 is not due to the excitation. The excitation was again 6016 MHz, with 20 mW of RF power.

of the limitations of the technique:

- The samples where between 10 nm and 30 nm thick, which yields a low magnetic contrast. In effect, the vortex core was not observed; neither static, nor dynamically through gyration.
- It was not possible to determine the exact resonance position of the lowest order mode, analogous to the discussion regarding TR-MOKE in Sect. 2.1: because the spacing between the excitation frequencies is too large.
- The combination of a thin membrane and a reduced atmospheric pressure, leads to an increased thermal stress on the samples. As a result, most samples were destroyed by the applied microwave power.
- The surface roughness of a SiN membrane is higher than for a Si sub-

strate. For very thin samples, this adds to the «*orange peel-effect*». The ground state may not be a magnetic vortex, but can e.g. contain multiple domains.

As a result, even for a 20 nm thick structure, the images are very noisy.
We could not excite the radial mode in all of the samples. Two examples of failed measurements are shown in Fig. 4.15, where an azimuthal spin wave is visible (left) and where the radial mode is severely deformed (right).

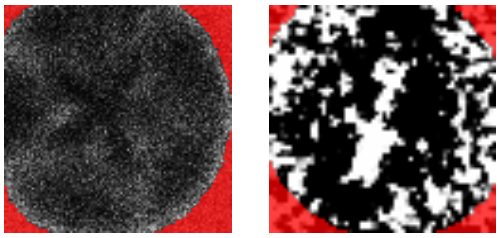

Figure 4.15: Shown are two (dynamic) STXM images for samples were no radial spin waves were visible. At the left is a 1 µm diameter, 20 nm thickness disc, showing an azimuthal spin wave profile. At the right, the radial profile is severely distorted for a 1 µm diameter, 10 nm thickness disc. The red areas correspond to non-magnetic material and are used for normalisation.

The azimuthal spin waves will most probably have been excited through an in-plane component of the magnetic field, as this disc was placed in the gap between a differential pair. If there was a slight phase imbalance between the two conductors, an in-plane magnetic field would have been generated.
The deformation of the radial mode is probably due to surface roughness, which can have very serious impacts on samples that are this thin (10 nm). Unfortunately, the sample did not survive the experiments and the post-mortem AFM did not yield any significant results.

4.3 Approach using the Magneto Optical Spectrum Analyser

The first measurement taken with our set up was on a 3 µm diameter, 30 nm thick Permalloy disc. This was one of multiple discs present in the gap

of a coplanar waveguide, as illustrated in Fig. 4.16. The samples had a typical DC resistance of the order of 10 Ω and typically showed a 3 dB loss in transmission. It is unclear whether this was due to the DC resistance, reflection from the inductance of the bond wires or the capacitance of the discs in the gap of the CPW.

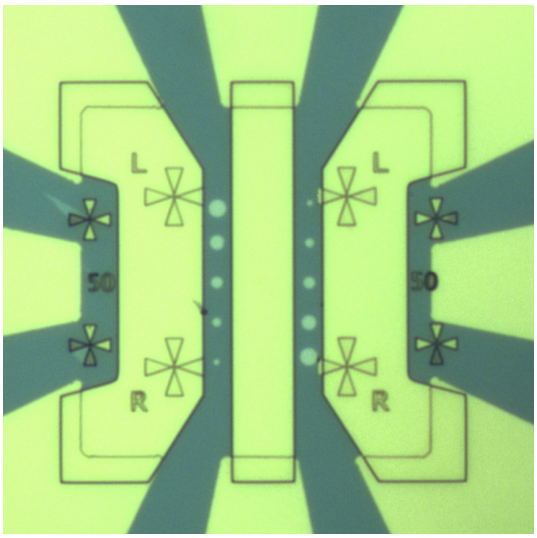

Figure 4.16: A micrograph of a sample used to study the effects of the aspect ratio on the resonance frequency of the lowest order spin wave. This sample has two series of 50 nm thick discs, with diameters between 3 μm and 1 μm, lying in the gap of a CPW.

The samples were excited with approximately 10 mW of RF power.

The result of a measurement (between the frequency limits of the set up) is shown in Fig. 4.17 for the aforementioned disc. In comparison with a typical UP spectrum, e.g. Fig. 3.7, the signal is much stronger for these radial modes. This was found to be consistent over all samples, with the exception of very thin samples (10 nm thick) which did show a reduction in signal of approximately 50%. The latter is due to the fact that the amount of light reflected is reduced for these very thin layers. Moreover, to prevent excessive heating, the power of the probe laser was also lowered. Note that $\langle m_z \rangle \propto$ snr, the time root-mean-squared average value of m_z is plotted. To determine the linewidth, a Lorentzian is fitted to the square of the spectrum.

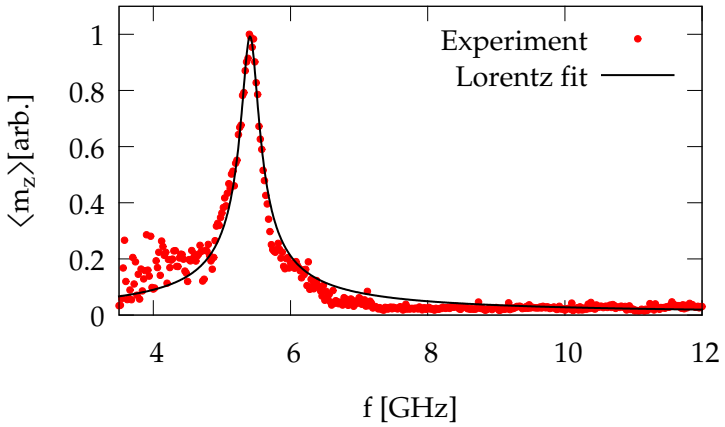

Figure 4.17: The first radial spin wave spectrum measured on a 3 µm diameter, 30 nm thick Permalloy disc using our set up. The frequency range extends between the lower and upper limit of the set up. A Lorentzian fit to the (square of the) spectrum is also shown, giving a resonance position of 5409.8 ± 1.2 MHz and a linewidth of 128.7 ± 1.7MHz.

Analogous to what was done for the uniform precession (UP) spectra, we measured the same spectrum five times and calculated the mean and standard deviation on these experimental curves, to obtain an estimate for the reproducibility of the measurement. This is shown in Fig. 4.18. They indicate that the signal quality is better than for the UP measurements.

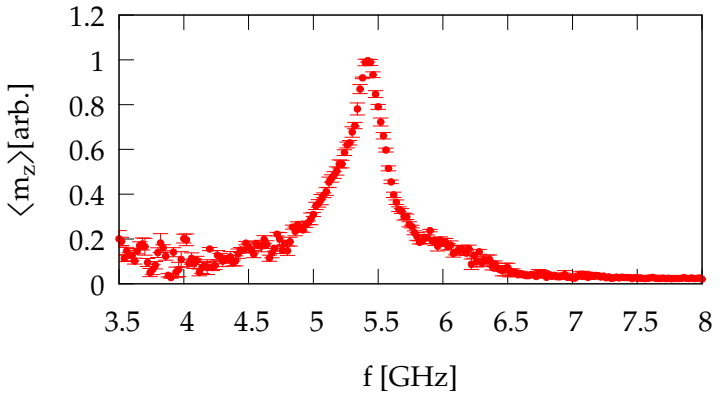

Figure 4.18: The lowest radial spin wave resonance curve, measured five times. The data points indicate the mean value, the error bars the standard deviation. This data is for a 3 µm diameter, 30 nm thick Permalloy disc.

Just as for the UP spectra, we also find that the spectrum in Fig. 4.18 is not exactly a Lorentz-curve. It is again slightly deformed and shows a bump around 6000 MHz.

4.3.1 Imaging in the spectral domain

In Appendix C we describe how the software is written in a modular fashion. This was required to allow for many different types of instrumentation to be added or removed and because one computer could not control all these. We shall now show that this has the added benefit that the type of measurement can also be easily modified. The image in Fig. 4.19 is exemplary of this versatility, because it is shows both m_z-dynamics (measured at a single frequency) and reflectivity.

To obtain this image, the laser beam was scanned over both the magnetic disc, Si substrate and Au CPW. For each pixel the magnetisation dynamics was recorded, together with the reflected light intensity. The 3 μm, 20 nm disc used in this measurement was excited at exactly the resonance frequency with 10 mW of RF power.

The Au CPW and Si substrate yield no $\langle m_z \rangle$-signal at all, as is expected. In contrast, the disc shows a response, uniform over the its surface. The fast scanning axis is the vertical axis for this image. This explains why we drifted slightly out-of-focus at the right side of the image, which was recorded about 20 minutes later than the left side. This is most clear for the reflectivity image.

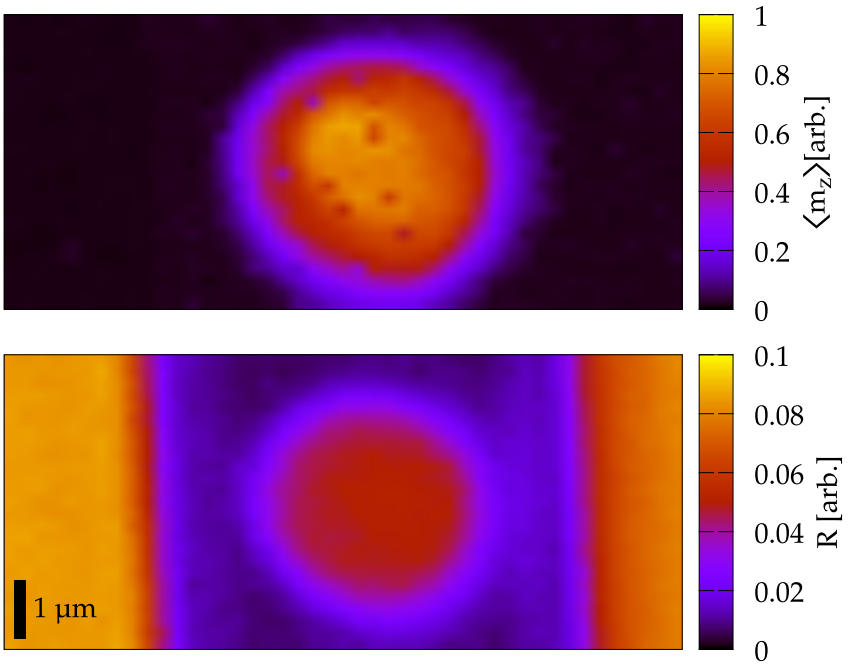

Figure 4.19: Shown at the top is an image of a 3 µm, 20 nm Permalloy disc in the $\langle m_z \rangle$-dynamics domain. The disc was excited at the resonance frequency of the lowest order RSW. At the bottom, the same disc, but now imaged using reflectivity data. Here we see not only the disc, but also the CPW which did not yield any signal in the top image. The pinning of the magnetisation near the vortex core is not visible here, in contrast with the TR-STXM image (Fig. 4.14). This is because our optical method is limited to a 500 nm resolution, whereas STXM can obtain a resolution down to 25 nm.

4.3.2 The effects of aspect ratio

In order to compare the analytical model with experimental data, samples containing discs with diameters between 1 µm and 3 µm of different thicknesses were fabricated. We selected thicknesses between 10 nm and 50 nm. For the 10 nm thick sample, only a diameter of 1 µm was fabricated, as the resonance frequency for larger discs would have been too low to be measurable with the set up. The limiting factor was the frequency mixer, which has a lower frequency limit of 4 GHz (cfr. Fig. 2.22, p.50).
For samples of 50 nm thickness, multiple diameters were available, but

these had a very low SNR. Therefore, these measurements show large uncertainty in determining the resonance frequency. They also do not follow the trend in Fig. 4.20 (they are indicated by the diamond symbols).

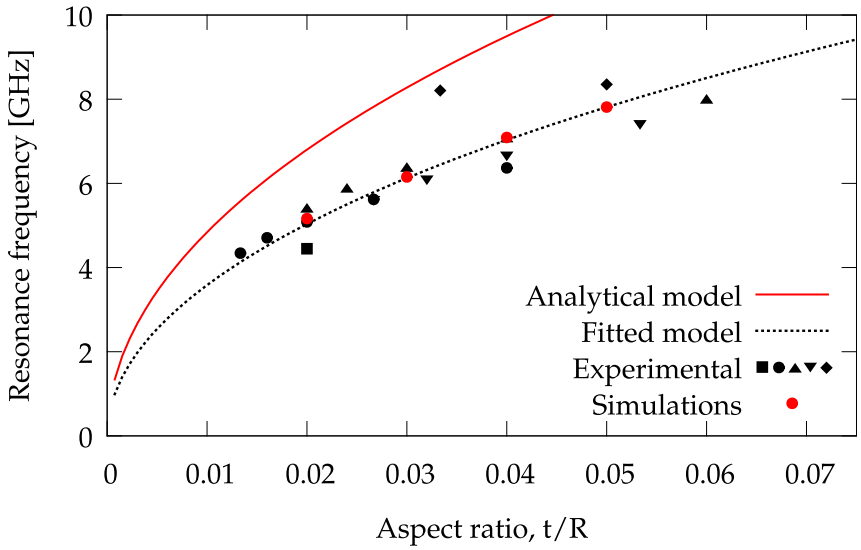

Figure 4.20: The influence of the aspect ratio on the resonance frequency of the lowest order radial spin wave determined experimentally. The solid line indicates the analytical solution of Eq. 4.5, which overestimates the resonance frequency. Only when M_S is reduced to 0.74 T does the analytical model match with the experimental data. The results from simulations with M_S=1 T (cfr. the value obtained from the FMR measurements in the previous chapter) are also shown. Square symbols correspond with 10 nm, circles with 20 nm, up pointing triangles with 30 nm, down pointing triangles with 40 nm and diamonds with 50 nm thick samples.

From Fig. 4.20 it follows that indeed the aspect ratio is the determining factor for the resonance frequency, and neither radius, nor thickness separately. This scale-independence indicates that there is no intrinsic length scale, such as exchange length, exerting any influence. Thus the magnetostatic energy determines their properties.

However, the experimental points only match up with the analytical curve if M_S is reduced to 0.74 T, which is a 25% reduction of the literature value of Permalloy. A possible explanation is that the thickness of the layers do not match with the values used in the calculations. Because the samples are

covered with a layer of Al_2O_3, it was not possible to measure their exact thickness (e.g. with AFM).

We also performed simulations with M_S=1 T (the value obtained from UP measurements in the previous chapter) for different thicknesses of 1 µm discs. Just as for the case for UP we used the strategy of exciting with an out-of-plane sinc-pulse, and performing a FFT on the recorded spatial average of m_z. The resonance frequencies that were found from these simulations also deviate from the theoretical prediction, and agree with our experimental points. The analytical model is most likely not accurate enough for this range of aspect ratios.

4.3.3 Beyond the linear regime

When the azimuthal spin waves are excited in the non linear regime, it was found that they can switch the vortex core polarisation. We can thus ask if the same holds for radial spin waves. Simulations have predicted a number of interesting features when these radial spin waves turn non linear, e.g., vortex core switching[59, 60] and Duffing oscillations [61].

A sample used for studying the non linear behaviour is shown in Fig. 4.21.

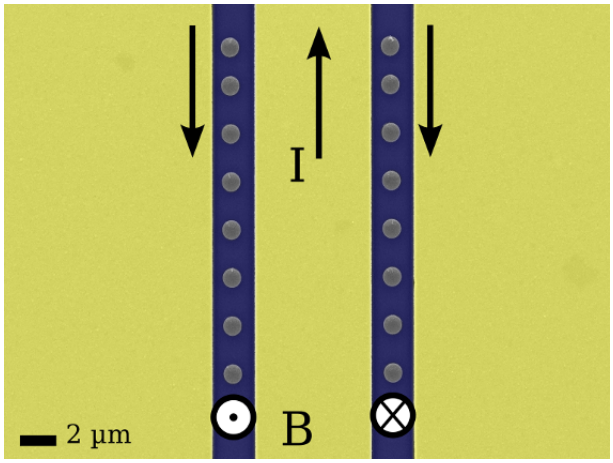

Figure 4.21: A false-colour SEM micrograph of the sample used for investigating non linear behaviour of radial spin waves. The discs lie directly on a Si substrate and are 1 µm in diameter and 10 nm thick. They are placed in the (2.5 µm) gap of a CPW in order to obtain a homogeneous and strong magnetic field.

In contrast to the samples required for STXM, the elements were not placed on a thin SiN membrane but on a thick Si chip (200 µm). Together with a 50 nm thick Au CPW ground plane, they succeeded in transferring all of the heat away from the magnetic discs.

The CPW shown in Fig. 4.21 was designed to balance two limiting factors. If the gap if the CPW was made very narrow, the magnetic field strength would have increased. However, it would have become less homogeneous and might excite the azimuthal spin waves. These could interfere with the radial spin waves in which we were interested, especially if the magnetic field is very strong (several milliteslas). If the gap of the CPW was made too wide, the field strength would have been too low to drive the radial spin wave into the non linear regime.

By combining calculations for the magnetic field profile and micromagnetic simulations for radial and azimuthal spin waves, a compromise was found. The centre conductor was 6.5 µm wide and the gap between the centre conductor and the ground plane was 2.5 µm. The in-plane and out-of-plane magnetic field were fitted to a fourth order polynomial and used for micromagnetic simulations. Several simulations were performed where each had the disc moved some distance from the centreline of the CPW. The sample was then excited at the resonance frequency of the lowest order RSW. When the discs were displaced by more than 500 nm from the centre, azimuthal spinwaves appeared. Therefore, only discs within this limit were probed experimentally.

The discs themselves were 10 nm thick, 1 µm in diameter and made of Permalloy. This thickness was chosen so the onset of the non linear behaviour was at a lowest magnetic field as possible, as was found by simulations. The samples could not be made thinner and still be reliable, because surface roughness would have a dramatic effect. Even for our 10 nm samples, about half of the probed discs did not respond to the applied excitation.

First the disc was excited using a relatively weak magnetic field amplitude, so the response would still be linear. Such a spectrum is shown in Fig. 4.22. Because the resonance position mainly depends on M_S and the linewidth depends on α, the influence of both could be separated. These material parameters were tuned until the simulations matched up with the experiment. The value of M_S was fixed at 690 kA/m and α at 0.008. The exchange

stiffness for the simulations was set at $13 \cdot 10^{-12}$J/m, a typical value found in literature[9].
For the simulations, we applied an oscillating magnetic field equal to

$$B_{ext,z}(t) = \sin(\omega t) \cdot \left(1 - \exp\left(-\frac{t^2}{\tau^2}\right)\right), \tag{4.6}$$

for the frequencies in the spectrum. The exponential term causes the excitation amplitude to smoothly ramp up. Applying the excitation in a step-like manner at $t = 0$ would cause an unwanted transient response (ringing). τ was chosen to be $30/\omega$, sufficient to suppress this ringing. The spatially averaged out-of-plane magnetisation, $m_z(t)$, was recorded and in post-processing the following was calculated:

$$\langle m_z \rangle = \sqrt{\frac{1}{T}\left(\int_0^T m_z(t)\sin(\omega t)dt\right)^2 + \left(\int_0^T m_z(t)\cos(\omega t)dt\right)^2}, \tag{4.7}$$

with T the runtime of the simulation. This corresponds with the experimentally accessible response, i.e. the narrowband, RMS value of m_z.

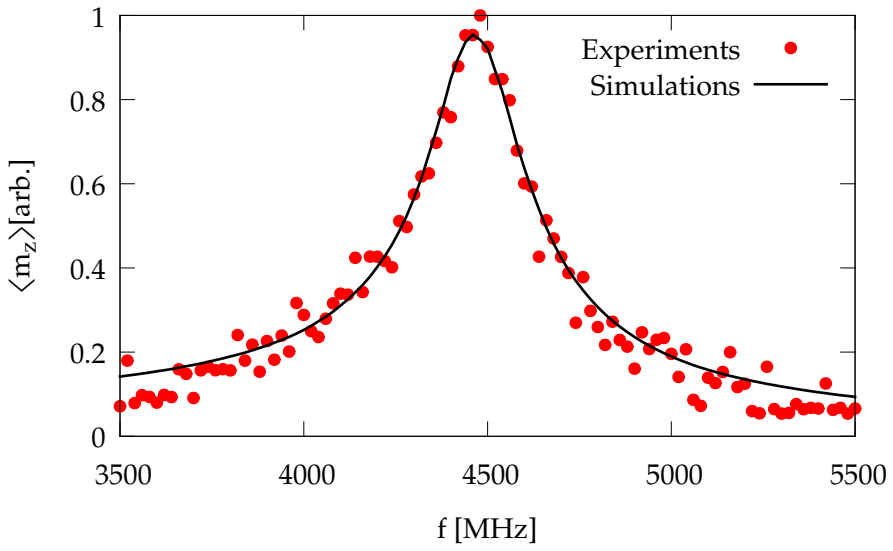

Figure 4.22: The first radial mode resonance of a 1 µm diameter, 10 nm thick Permalloy disc. This measurement was made in the linear regime with a moderate excitation strength of 0.5 mT. The material parameters used for this simulation (M_S = 690 kA/m, α = 0.008) were adjusted to fit the simulation to the experimental results. The exchange stiffness was the typical value of $13 \cdot 10^{-12}$ J/m as found in literature.

The RF power was then increased in such steps, that the corresponding magnetic field would increase linearly. The response of the sample in function of frequency and applied magnetic field is shown in Fig. 4.23.
From this figure, it follows that the mode succumbs to non linear phenomena when the excitation field strength is increased beyond 2 mT. This is evident because the resonance frequency start to shift to the lower range (i.e. red-shifting) and becomes very skewed at around 4 mT and above. The same transformation of the spectrum was found for non linear vortex gyration, studied by VNA-FMR[62]. When the vortex is displaced far from the centre, the harmonic approximation to the potential well is no longer valid. The authors also found evidence that the direction in which the resonance shifts, is related to the aspect ratio.

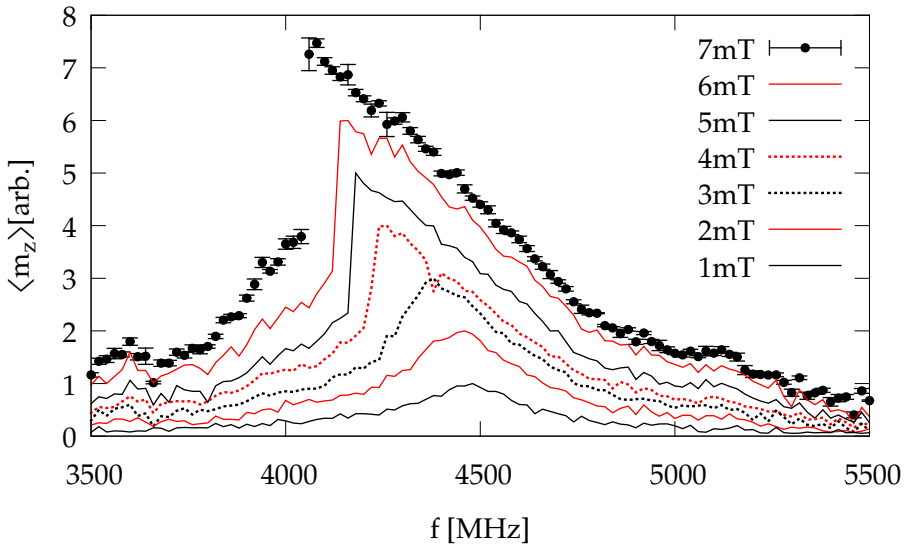

Figure 4.23: The first order radial spin wave mode in a 1 µm, 10 nm thick disc shifts towards lower frequencies when the excitation amplitude is increased. This, together with the strong skewing of the spectrum is indicative of non linear effects becoming dominant. The error bars (defined as the standard deviation on five consecutive measurements) for the strongest excitation are also indicative for the errors at lower excitation strengths. Frequency steps of 20 MHz were used.

The maximal field strength was 7 mT, which required a microwave power of approximately 0.5 W.
Though a Travelling Wave Tube Amplifier (TWTA) was available (which

could generate up to 10 W of power), it was found that 0.5 W was the upper limit. The problem was that the power could no longer be kept constant. As the sample absorbs about half of the applied power, the thermal drift by microwave heating becomes frequency dependent. In effect, the samples drifted significantly (several μm) when the frequency was varied between 3.5 GHz and 5.5 GHz.

Because the material parameters were determined in the linear regime, we could compare the experimental results with the results from simulations at the higher excitation levels (retaining the material parameters from the linear regime). This is shown in Fig. 4.24. The qualitative agreement between simulations and experiments gives us confidence that what we measured was indeed a non linear radial mode, and not e.g. the appearance of an azimuthal mode (as was the case for a STXM measurement).

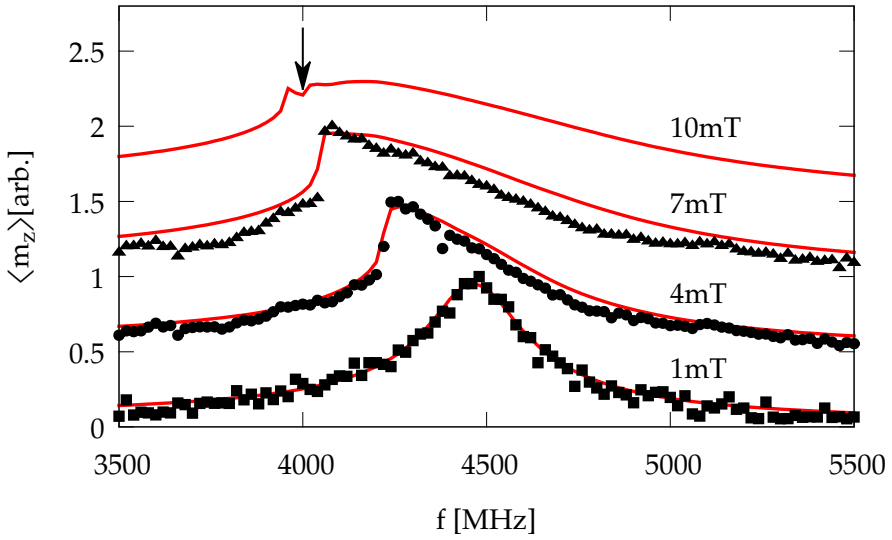

Figure 4.24: A comparison between the measurements and results from simulations. The material parameters for the simulations were fixed by comparing both in the linear regime (lowest curve). Curves are offset and scaled to unity for clarity. The simulation for an excitation field strength of 10 mT shows a reduction at the top of the resonance curve, indicated by the arrow.

Simulations were also performed at an excitation strength higher than experimentally available. In Fig. 4.24 we have shown the result of a simulation performed with an excitation strength of 10 mT. Besides further red-

shifting, this curve has a very interesting feature where the maximum response is expected. Here, the curve shows a reduction of signal.
To investigate what leads to this reduction, simulations were performed at the 4 GHz, 10 mT excitation, recording the full magnetisation in function of time. For a selected number of points in time, this is shown in Fig. 4.25.

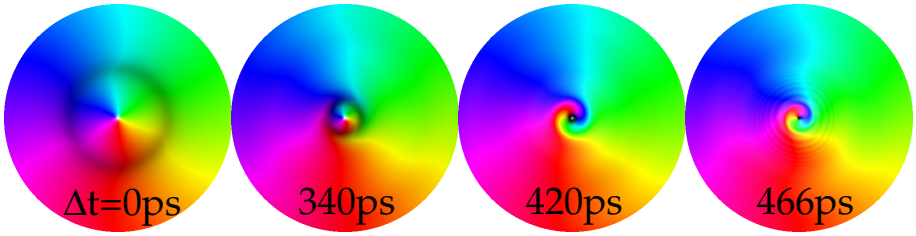

Figure 4.25: The formation of a soliton from a radial spin wave for a 1 µm Permalloy disc. The soliton collapses unto the centre of the discs, where it switches the vortex core polarisation

We see that instead of performing a uniform oscillation, the spin wave condenses into a soliton. Such behaviour has also been found in a non-confined geometry by Bauer *et al.*[63] by BLS.
In contrast to the RSW, this soliton is not a stationary phenomenon, but moves toward the vortex core. Because the magnetisation turns completely out-of-plane at the position of the soliton when it nears the core, it switches the vortex core polarisation. 3D simulations have shown that this switching process does not involve movement of the core or a vortex/anti-vortex pair. Instead it is mediated through the injection of a Bloch point. A Bloch point is defined as a magnetic singularity where: «*for any closed surface surrounding the point, the magnetisation vectors on this surface cover the surface of the unit sphere exactly once*»[64]. It takes approximately 1 ps for the Bloch point to traverse the core and invert the polarisation. This time is not very trustworthy though, because it is unclear how representative the micromagnetic framework is on these scales.
After scattering on the core, the soliton is broken up into short wavelength spin waves. These have a reduced contribution to the calculated response, as they average out over the entire surface of the disc. This self-focussing into a soliton, which then breaks up, explains the reduced response near the expected maximum of the resonance curve in Fig. 4.24.
The demagnetisation, exchange and total energy are shown in Fig. 4.26.

When the soliton is formed, the system builds up demagnetisation energy at an increased rate (from 3 ns on). When the diameter of the soliton decreases, the energy of this configuration due to the demagnetisation field decreases (starting at 3.8 ns). It is only when the self-focussed spin wave collapses unto the core of the disc, that the magnetostatic energy is transferred to exchange energy (at 4.2 ns). That high exchange energy is due to strong magnetisation gradients present in short-wavelength spinwaves.

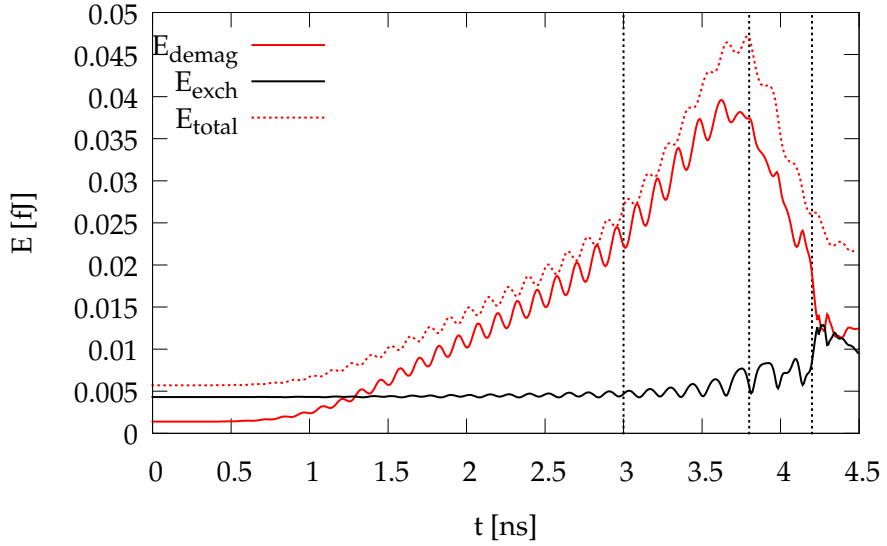

Figure 4.26: The demagnetisation, exchange and total energy of a 1 µm disc when excited at 4 GHz with a 10 mT out-of-plane magnetic field. At 3 ns the self-focussing starts, at 3.8 ns the formed soliton starts to collapse onto the centre. At 4.2 ns the soliton nears the vortex core, switching it only a few ps later.

We have also artificially pinned the vortex core in simulations through the application of a 20 T field at the centre of the core. This did not yield a different behaviour of the soliton. Removing magnetic material at the centre of the disc, but leaving the vortex ground state otherwise unaltered also did not affect formation and breaking up of the soliton. Hence, the soliton formation and breaking-up is a property of the vortex itself, unaffected by the presence of the vortex core.

The switching threshold (field amplitude needed to switch the vortex core polarisation) was also studied as a function of the excitation frequency. The

resulting switching diagram is shown in Fig. 4.27. For each excitation strength, the spectrum in function of frequency was scaled so the maximal $\langle m_z \rangle$ (excluding points showing switching) was equal to one. This was to increase the contrast.

Starting at the lowest excitation strength for a specific frequency, the excitation was increased until switching occurred. This was detected by verifying the vortex core polarisation each $1/(8f)$ time interval, with a total runtime per excitation amplitude of $50/f$.

The lowest order mode switches at the lowest field strength, with subsequent modes having a higher threshold. The even modes all have lower switching threshold than the odd order modes. This is most likely due to the spatial overlap between the mode profile and the excitation, which is strongly reduced in the case of the odd modes. Thus resulting in a diminished coupling between excitation and RSW.

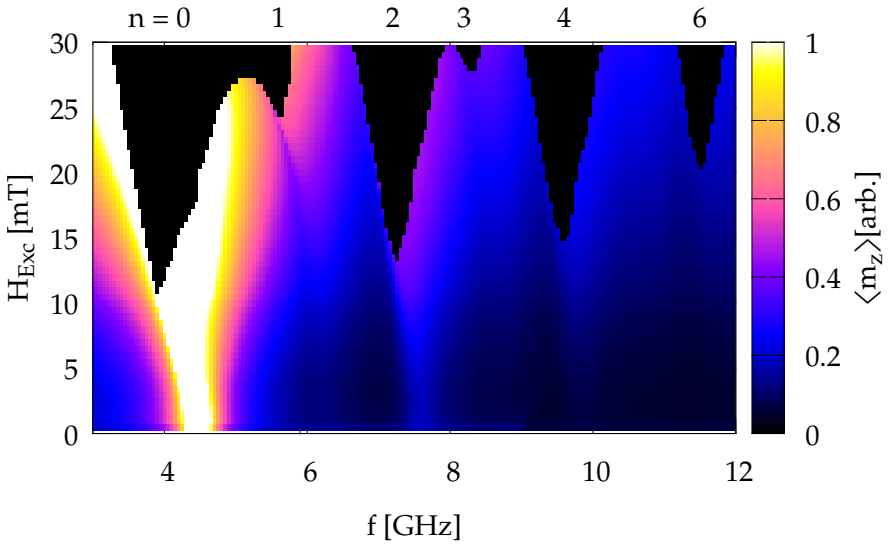

Figure 4.27: The switching diagram for a 1 µm diameter, 10 nm thick Permalloy disc in function of the excitation frequency f and amplitude H_{Exc}. Areas that are coloured black show vortex core switching. Higher order modes are also visible and can also lead to vortex core switching, though at higher excitation levels.

4.4 Discussion

Only recently has non linear behaviour of radial modes been studied from a theoretical perspective[65, 61]. Pylpovskyi *et al.*[65] take a combined approach of both micromagnetic simulations and analytic results using their reduced vortex model. They find that switching the vortex core polarisation can proceed in a selective fashion by using tailored RF bursts, and that the spectrum shows areas of chaotic vortex motion in the non linear regime. However, their excitation is unrealistic for practical experiments (several 100's of milliteslas at several gigahertz).
Moon *et al.*[61] take the approach of a pseudo-macrospin. Because the oscillation is almost uniform over the surface, except near the vortex core, the magnetisation can be represented by two angles. The first one is the angle at which the magnetisation turns out of plane, θ. The second angle, ϕ, indicates the amount the magnetisation tilts towards to the radial direction. Using these two variables, the magnetisation can be written as:

$$m_r = \cos\theta \sin\phi, m_t = \cos\theta \cos\phi, m_z = \sin\theta, \tag{4.8}$$

where m_t is the tangential magnetisation component. This can then be substituted in the LLG equation, yielding two coupled first order differential equations for θ and ϕ. This system can then be transformed into a single second order differential equation. Making the approximations $\theta \ll 1$ and $\phi \ll 1$, the equation governing the oscillating behaviour was found to be:

$$\frac{d^2\phi}{dt^2} + \omega_0^2 \left(1 - \frac{3}{2}\phi^2\right)\phi + D\frac{d\phi}{dt} - \gamma H\omega \cos(\omega t) = 0. \tag{4.9}$$

The third term is a dissipative term and responsible for the damping of the oscillation. The fourth term is the external driving term. The second term is the associated potential energy, which is no longer a harmonic potential but carries a third order term. This anharmonic term is responsible for non linear effects.
Performing micromagnetic simulations, Moon *et al.*[61] have also found evidence for hysteresis, shown in Fig. 4.28. They applied an oscillating magnetic field with a frequency above the resonance frequency. While keeping the phase of the signal continuous, they then swept the frequency to below the resonance frequency. Afterwards, they swept it in the opposite direction, stopping at the original starting frequency. What they found is that

the average out-of-plane magnetisation shows hysteresis, as is shown in Fig. 4.28. Moreover, when excited in exactly this manner, the core polarisation switches at lower excitation amplitudes than for continuous excitation. In our experiments and simulations, we have only used continuous excitation.

Such a hysteresis behaviour forms the basis for selective switching; only when sweeping along a particular direction does switching take place. This is in contrast to fixed frequency switching, where there is no selective switching and the core polarisation flips continuously. However, this type of excitation is almost impossible to create for the frequency range in which these radial modes can be found (above 4 GHz).

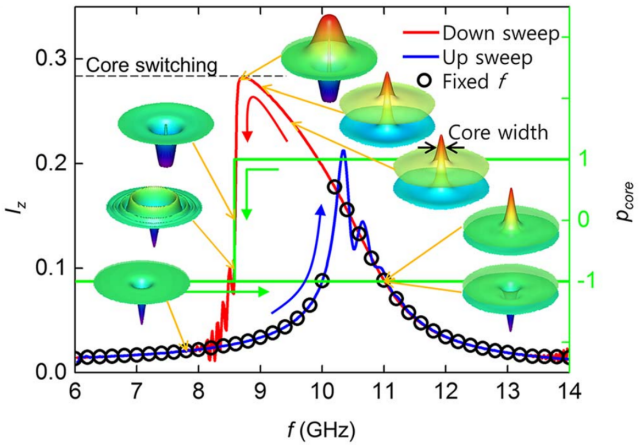

Figure 4.28: Shown is the hysteresis behaviour of the (spatially) average out-of-plane magnetisation (I_z) and core polarisation (p_{core}) when the excitation is swept in frequency, keeping the phase of the signal continuous. This figure is the result of micromagnetic simulations for a 160 nm diameter, 7 nm thick Permalloy disc. Reproduced from [61].

We have also performed sweeps in two directions experimentally, but found no evidence for hysteresis. This is not unexpected, as we can not keep the phase of the signal continuous as the frequency is altered. The shape of the experimentally measured resonance, e.g. Fig 4.23, does match up with the fixed frequency calculations of Moon *et al.*[61], shown in Fig. 4.28.

4.5 Conclusion

Using the Magneto Optical Spectrum Analyser, we were successful in measuring the radial spin waves. Because the method is fast and user friendly, a systematic study of the influence of the aspect ratio on the resonance frequency of the first radial mode was possible. It was found that for the thicknesses under study, the frequency depends solely on the aspect ratio. This is explained by the fact that the modes are of a magnetostatic origin, and thus lack a definite length scale (due to e.g. exchange interaction, crystalline anisotropy, etc.). The experimental data agreed very well with corresponding micromagnetic simulations.
It was found that when the modes were excited with increasingly stronger magnetic fields, the resonance frequency would shift towards lower frequencies. Besides this, the spectrum also becomes strongly skewed.
Simulations agreed with this on the quantitative level, and predicted the formation of a soliton. Such a soliton can switch the vortex core polarisation. It was found by Moon *et al.*[61] that hysteresis for the switching process can be created by sweeping the frequency, but keeping the phase continuous.
We also investigated radial spin waves using TR-STXM, but due to two main factors, were forced to abandon this approach. These factors were

- Insufficient contrast due to thin samples;
- Incompatibility of the samples with the required microwave power for the excitation.

Chapter 5

Conclusion and outlook

5.1 Conclusions

In Ch. 2 we explained in great detail how we developed a new type of measurement set up, with the ability to measure magnetisation dynamics in the frequency domain using an optical probe. When we compare this method with currently available techniques (e.g STXM, TR-MOKE, VNA-FMR and BLS) we see that it fills a gap where no other technique can measure.
Though the general concept of the measurement is easy enough, the practical realisation featured a number of technical challenges; the extreme shielding between excitation and receiver of 130 dB for example.
In Ch. 3 we benchmarked our method by measuring the uniform precession of magnetisation in a thin Permalloy film. This illustrated that our method produces quantitative results, yielding not only estimates for the saturation magnetisation but also for the intrinsic damping parameter α. The latter did suffer from some uncertainty due to incomplete calibration of the response of the detector in function of frequency.
Measurements presented in Ch. 4 were the main objective of this thesis: being able to measure radial spin waves in the nonlinear regime. (Because STXM measurements were unable to confirm non linear behaviour, we where forced to develop a new technique; described in Ch. 2.)
Using our method we were able to measure samples as thin as 10 nm without any problems. Measurements showed that as the excitation amplitude was increased, the resonance curve shift towards lower frequencies. At the same time, it becomes strongly skewed. Such behaviour was also found for

the case of non linear vortex gyration by Drews *et al.*[62].
Our experiments matched up with micromagnetic simulations in the non linear regime, with material parameters fitted in the linear regime. The simulations allowed us to explore the response to magnetic fields stronger than those available experimentally. We found that when the excitation is high enough, the spin wave starts to show self-focussing. Such a self-focussed spin wave collapses on the vortex core, possibly inverting its polarisation. Micromagnetic simulations performed by Moon *et al.*[61], show that such process can even be selective on the original core polarisation.

5.2 Future outlook

5.2.1 Improvements to the experimental set up

Our set up was specifically developed to study radial spin waves, and because of this it measures in the polar domain at frequencies between 2 and 12 GHz.
The polar configuration has a number of drawbacks. First, the number of magnetic phenomena that show out-of-plane dynamics is rather limited. My first suggestion would be the transform our set up so the probe beam is no longer perpendicular incident, but at an angle of 45°. The consequences of this are:

- No need for a beam splitter, thus not half of the reflected light (which carries the magnetic information) is lost.
- A slight reduction of the Polar Kerr Effect, but a gain for the Longitudinal Kerr Effect. This would allow for better measurements of uniform precession and make detection of vortex gyration feasible.
- The need for a second objective lens and somewhat more difficult alignment.

Another alteration to the set up follows from the results of Nembach *et al.*[66]. Their set up is sketched in Fig. 5.1. They use two frequency locked lasers, at frequencies ω_1 and ω_2. A photodiode illuminated by these two lasers performs a mixing operation (photocurrent is proportional to the intensity $\propto \mathbf{E}^2$), producing a RF signal at frequency $|\omega_1 - \omega_2|$ (among others

which are either at DC or extremely high frequency). This difference signal is then used for exciting the sample.
Because of the excitation, there will be magnetisation dynamics at a frequency $|\omega_1 - \omega_2|$. If this sample is then illuminated with the Probe Laser (with frequency ω_1), the signal will be upconverted to frequency ω_2. This light is then incident on a photodiode together with the LO Laser (with frequency ω_2). Therefore, the signal present at frequency ω_2 will be down-converted at the photodiode by the LO Laser to DC.
The advantage of this method lies in the fact that the resulting signal is not given by $V \propto |E|^2\theta_K$ (as it was in our case), but $V \propto |E_{probe}||E_{LO}|\theta_K$. There are no restrictions on the intensity of the LO laser as it does not illuminate the sample, therefore E_{LO} can be made much larger than E_{probe}. This would result in a much higher signal-to-noise ratio.

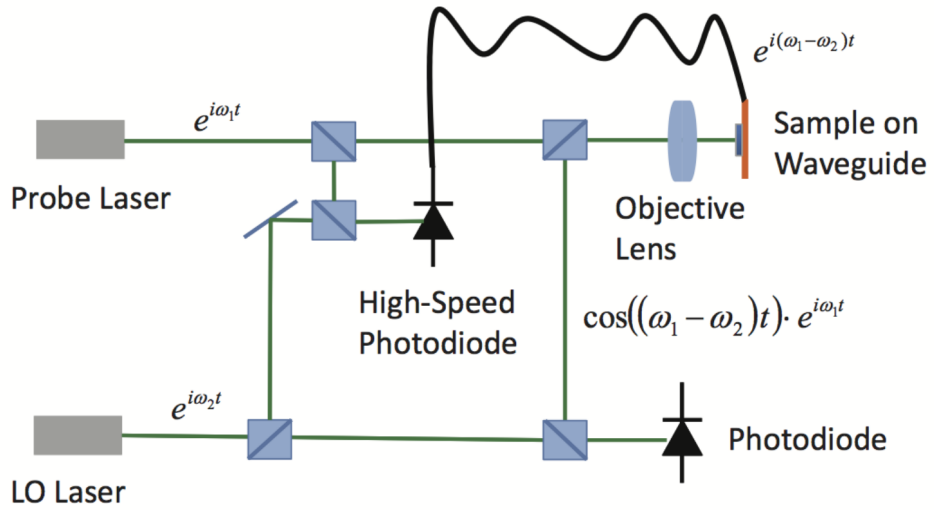

Figure 5.1: The experimental set up developed by Nembach *et al.*[66]. The RF signal used for excitation is obtained by mixing two frequency locked lasers. This type of set up enables them to substantially increase the detector efficiency. Reproduced from the Supplementary Materials of Ref. [66].

Our set up can be modified to accompany this kind signal boosting, as shown in Fig. 5.2. Because a large portion (90% in the example) of the original beam does not need to illuminate the sample, the total intensity can be made much larger without serious thermal problems for the sample. As

illustrated above, the signal-to-noise ratio can thus be increased ten times as well.

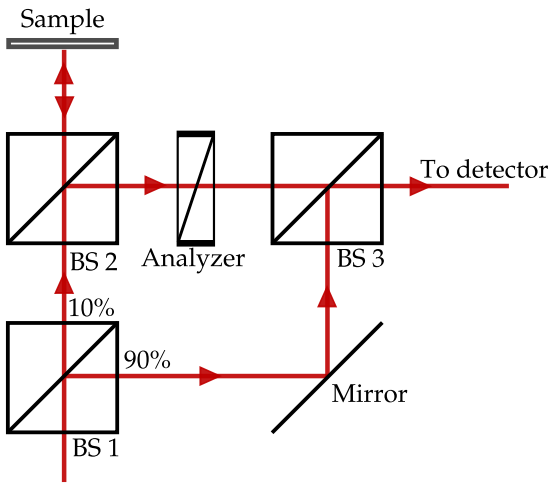

Figure 5.2: A possible way to increase the signal-to-noise ratio. The original beam is split in two, one high and one low intensity beam. The low intensity beam is used for illuminating the sample, while the high intensity beam is simple diverted around. The two are than combined after the sample and analyser crystal. Detection is still at high frequency.

This modification can be easily made and is highly recommended.

Appendix A

STXM post-processing

The following procedure was applied to transfer the raw STXM data into usable images:

1. (Optional) A median filter was applied when dead pixels (containing either almost none or too much intensity) were present, replacing each pixel with the median of its neighbours.

2. The image consists of bright areas where there is no Permalloy and darker areas where there is. Looking at a static image (i.e. summing all channels) the x% quantile of the intensity distribution (histogram of all pixel values) was calculated, with x between 60% and 90%. Pixels that were brighter than this value were determined not to be part of the Permalloy.

3. For each channel, the image was rescaled until the intensity of the non-magnetic areas was equal, using the mask that was obtained in the previous step.

4. The average of all channels was subtracted from all the channels, yielding a dynamic image and removing all static components.

5. (Optional) A Gaussian filter was applied to create a smooth image.

6. The channels were sorted in time.

7. The pixel values of the dynamic images follow a Gaussian distribution. We calculated the mean and standard deviation in the masked

region for each channel and used the cumulative Gaussian distribution with these parameters, to transform the pixel values to a grey scale value. This is a very robust method to increase the contrast of the images.

For a static image, a linear mapping from intensity to grey scale was used because the pixel value does not follow a specific distribution.

8. This grey scale value was used for plotting the final result, making use of the ImageMagick library.

Except for filtering and sorting, this is illustrated in the C++ code listing below.

```
#include "Channel.hpp"

#include <stdio.h>
#include <stdlib.h>
#include <vector>

#include <boost/math/special_functions/erf.hpp>

#define NBINS 100
#define INVSQRT2 0.7071067811865475244

int linearMapping( double x, void *args)
{
    Channel *ptr = (Channel *)args;
    double min = ptr->getMin(), max = ptr->getMax();
    return (int)(255.0 * (x-min)/(max-min));
};

int erfMapping( double x, void *args)
{
    double *ptr = (double *)args;
    double mu = ptr[0], sigma = ptr[1];
    double tmp = INVSQRT2*(x-mu)/sigma;
    //template double boost::math::erf<>(double);
    return (int)(125.5 * (1.0 + boost::math::erf<>(-tmp)));
    return 1;
};

int main(int argc, char **argv)
{
    assert(argc > 1);
```

```
    std::vector<Channel *> channels;
    importData(argv[1], &channels);

    Channel *a = channels.at(0);
    Channel staticImage(a->getRows(), a->getCols());
    Channel mask(a->getRows(), a->getCols());

    for(unsigned int i = 0; i < channels.size(); i++)
    {
        a = channels.at(i);
        mask += *a;
    }
    mask.toMask(0.7);
    mask.drawChannel("mask.gif", linearMapping, &mask);

    for(unsigned int i = 0; i < channels.size(); i++)
    {
        a = channels.at(i);
        a->scaleMean(&mask);
        staticImage += *a;
    }

    staticImage /= (double) channels.size();
    staticImage.drawChannel("static_image.gif", linearMapping, &
        staticImage);

    double params[2];
    char filename[1024];
    for(unsigned int i = 0; i < channels.size(); i++)
    {
        a = channels.at(i);
        *a -= staticImage;
    }

    for(unsigned int i = 0; i < channels.size(); i++)
    {
        a = channels.at(i);
        a->extractMaskedStats(params, &mask);
        params[1]*=1.1;
        sprintf(filename, "image_%03d.gif", i);
        a->drawChannel(filename, erfMapping, (void *)params);
    }

    return 0;
};
```

Appendix B

Optical alignment

The basis for this appendix lays in Fig. B.1.

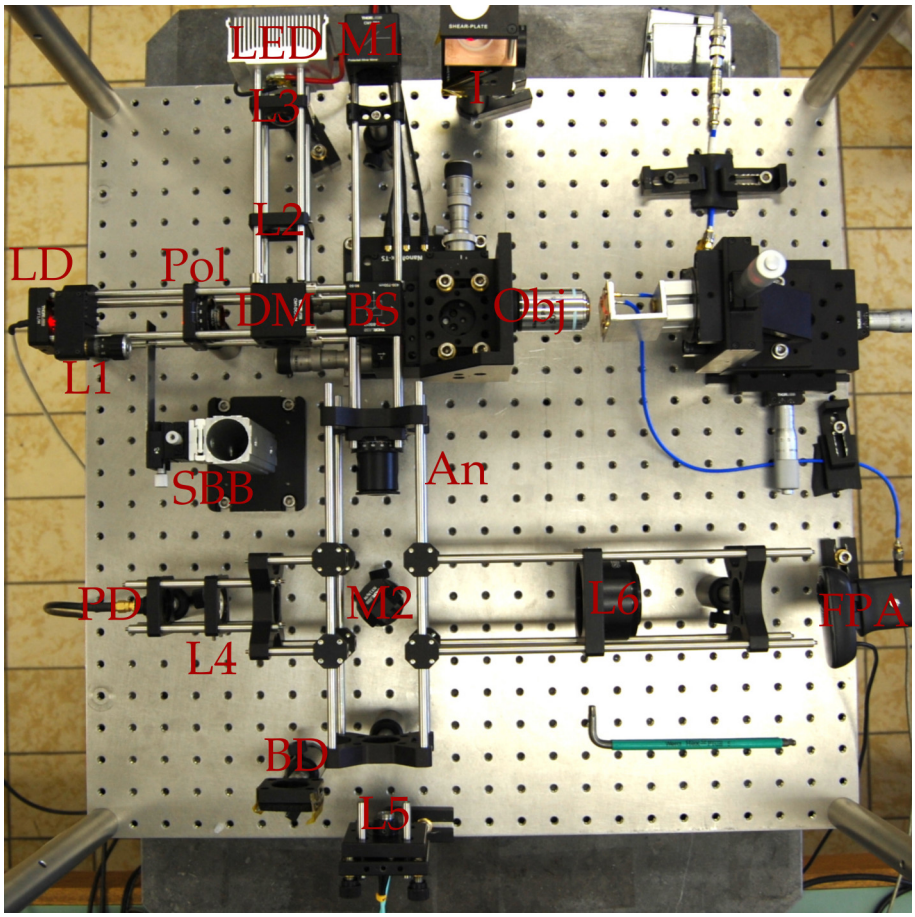

Figure B.1: A photograph of the optics set up, L1-6 are lenses, M1,2 are mirrors. LD is the laser diode with L1 the collimating lens. Pol is the polariser, followed by the dichroic mirror DM. After that comes the beam splitter BS which allows the laser beam to illuminate the sample through the objective. Reflected and redirected light is then analysed using the analyser An. Mirror M2 allows to redirect the light to a number of targets. L6 is a tube lens the focusses the (white) light onto the camera (FPA) for fullframe imaging. L5 focusses the light on the fibre. L4 focusses the light on the slow photodiode PD for piezo imaging. BD is a beam dump.

In the case of gross misalignment, e.g. earthquake, the following can provide a rough guide to aligning the optics.

1. Retract the semi-beam blocker (SBB) completely. We need a collimated laser beam perpendicularly incident on the objective. To achieve

this, you need to align the laser diode with the objective first. You can use the adjustment screws on the laser diode to this end. Once this is done, you can collimate the light with the collimating lens L1, directly after the laser diode. First, allow the beam that is incident but coming out of the beam splitter to travel a large distance, until it hits a wall. If the laserspot is the same diameter over the entire length it can travel, the light is collimated. Simply use a piece of paper to check this.

Now redirect this light using mirror M1 into the shearing interferometer I. When the fringe pattern visible on the interferometer is parallel to the line drawn on the interferometer, collimation has been achieved. For this step, I would recommend using only the precise Z-adjustment on L1. You should be able to see a fringe pattern on the interferometer, if this is not the case move the LD current around a bit. Taking different angles to look at the interferometer should help as well.

2. Hooray, you have been able to collimate light into the objective. Now you have to bring a sample into focus and make sure the light coming out is also collimated. You can focus the objective on a **dirty** mirror perpendicular to the beam to this end. Now move the objective lens towards and away from the sample until light coming out is in focus. Again, first make it travel a great distance and only then use the interferometer.

3. Now we are getting places. Because the sample is now in focus, we can start to align the tube lens L6. Turn down the laser diode until hardly any light is reflected of the sample. Make sure that mirror M2 redirects this laser light through L6 onto the camera FPA. If this is not the case, loosen the base of M2 and rotate it until light hits the FPA. Tighten the base and turn of the laser diode. Start the camera software and turn on the LED (it can handle 700 mA). Make sure that at least some light is focussed on the rear of the objective lens. L3 collimates LED light, L4 focusses it on the rear focal plane of the objective. Google Kohler illumination to see why I did this and how it works/how to align it. Now simply move the tube lens L6 until the picture becomes clear (if you used a clean mirror you probably will not see anything). Tighten afterwards.

4. We are almost done, now we only need to collect the laser light with L5 into the optical fibre. This is the most delicate operation. First make sure (using the alignment tool) that the laser spot hits the centre of L5 at perpendicular incidence. You can loosen the base to do this. Leave the fibre connection at L5, but disconnect the other end of the cable. You should see some light coming out of this end. Now turn the two knobs on the tilt stage until light coming out is maximum (the third knob is pretty useless). It is relatively safe to look directly at the fibre end because of reflection losses, coupling losses, etc. but if you are unsure, you can simply shine it on a piece of paper. Reconnect the fibre. If you can measure the photocurrent at the detector (see Appendix C) you can further optimise at the tilt stage.

This should be your quick-check list for the optics:

- Sufficient light?
- Semi-beam blocker in place?
- Analyser-polariser at 45° relative to each other? In aligning analyser and polariser, take into account that laser light from a diode is already (partially) polarised.
- Light on the lens/coupling assembly? Possibly disconnect other end of fibre to verify good coupling.

Appendix C

Software

The entire set up consists of several modules: signal generators, piezo stage, DAQs, etc. separated over a distance of 50 m. It is therefore difficult for only one PC to control all the different modules, especially since there can be variation in the instrumentation used in the set up. For example sometimes it was needed to use a different signal generator to obtain higher power levels. Such a modular structure required a distributed approach, such as the scatter-gather technique. This entails that a single master controls a number of slaves. Each of such slaves controls a specific piece of equipment (power supply, multimeter, etc.) and reports back to the master. In our case, each module has its own specific controller program. This leaves open the question of how these controllers communicate with the master. Each of these programs receives standardised commands over TCP and translates this to a command for its module, using the specific local interface protocol for that piece of equipment. For example to set a HP 8672A signal generator to 3.5GHz the command would be

```
SET,FREQ,3.5e9
```

which would be translated to the following ASCII string

```
Q350T000Z2
```

sent over GPIB to the signal generator in question. Each controller can be identified by the IP address of the server it is running on and the port it is listening on. For protection, the ports were hidden behind the firewall and were only available through secure SSH tunnels. The situation is depicted in Fig. C.1.

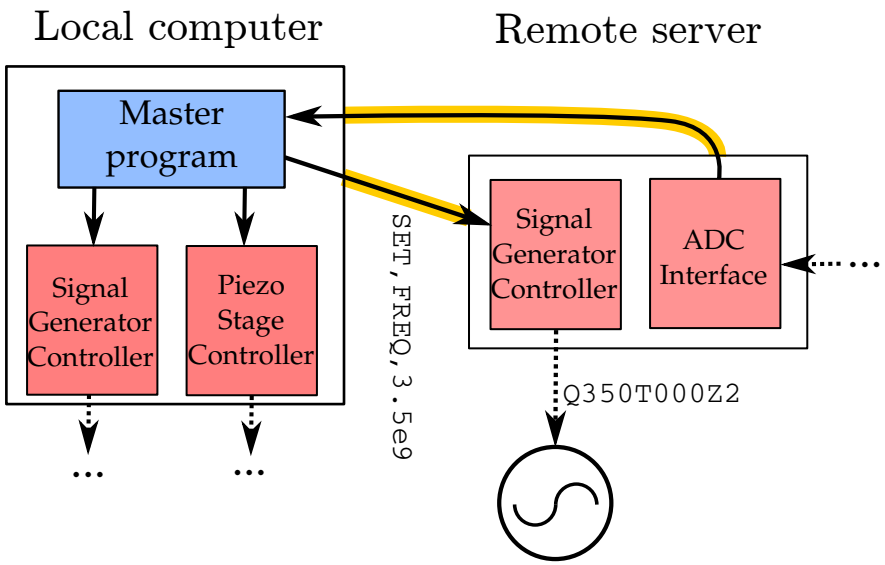

Figure C.1: A schematic representation of the software layout. Solid arrows indicate TCP connections, yellow backdrops imply SSH tunnels and dashed arrows can imply any number of local interface protocols used (GPIB, USB, ...).

At the end of the microwave chain the magnetic signal needs to be converted into the digital realm. Because the frequency range of the signal we are interested in, is only up to a few tens of kilohertz, an high grade audio ADC is the best option. We have opted for a sound card from Terratec GmbH; the «*DMX 6Fire*». This card features a 24-bit ADC that has a sampling rate of up to 196kSamples/s, combined with a dynamic range of 114dB.

When triggered, the software starts recording an audio sample and an FFT is performed on the recording. The FFTW2 library was used to calculate the FFT. An example of such low frequency spectrum is shown in Fig. C.2. The length of the recording depends on the bandwidth required, and is taken to be 2^N samples. Because of rounding, the actually used bandwidth will always be equal or less than the required one.

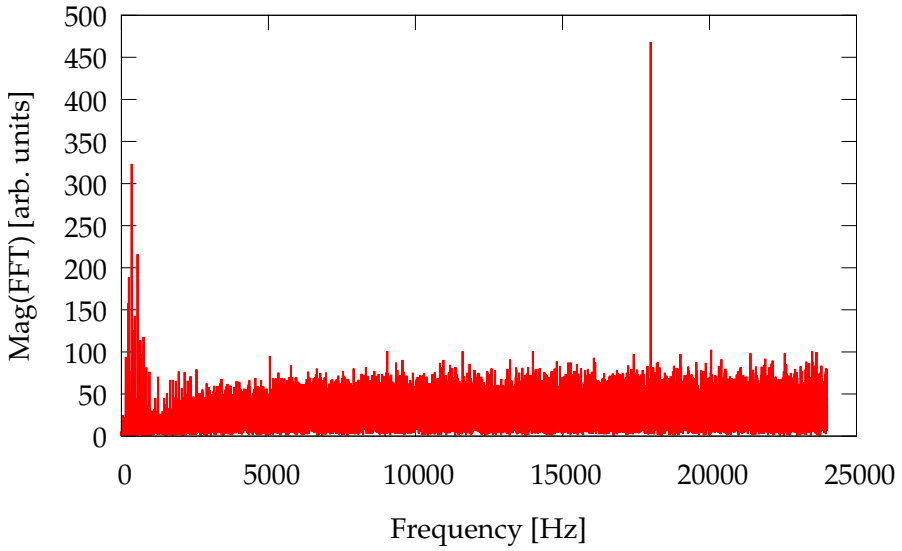

Figure C.2: An example FFT of the measured signal at the end of the microwave chain. This was measured for an FMR experiment with 30µA of photocurrent at the FMR resonance. The actual magnetic signal is the peak at an offset of 18kHz.

Instead of sending the entire FFT data over the network, a small section around the expected peak position is cut out. Note that because the sound card is not phase or frequency locked to the signal generators, the value of Δf calculated from the sound card is not necessarily equal to the value of Δf set by the signal generators. In this narrow region, the highest value is then recorded and regarded as the measured value of the signal. So even when no signal is present, this value will still be larger than the average noise floor.

The average signal level excluding this peak is also recorded and sent. This enables a calibration of the conversion efficiency as explained in Sect. 2.4.6.

The following should provide the user with a guide how to set up a basic measurement. The computer next to the optical set up is the master. On this computer, the following programs from the suite should be started:

- `user@mona> Controller 5000`

  This is the piezo and electromagnet controller. The controller should appear as /dev/ttyUSB0, if not you should disconnect and cycle the

power of the controller. Always turn off the piezo power supply before turning the controller on or off.

- ```
  user@mona> HPInterface 5003
  ```

  This is the interface between the master and the HP signal generator. The interface should appear as /dev/ttyACM0.

- ```
  user@mona> RigolInterace 5005
  ```

  This measures the DC voltage on the Rigol multimeter, which is usually connected to the RF detector diode.

Then a SSH tunnel needs to be set up from the master to the computer at the detector. This is because the other software opens ports that are above 1024 and thus closed by the firewall.

- ```
  user@mona> ssh -L 5004:localhost:5004 dynalab
  user@dynalab> FFTGrabber 5004
  ```

  This is the software that acquires the low frequency signal and processes it using FFT. After each measurement, the entire spectrum is saved in its execution directory as spectrum.dat. Make sure that the sound card microphone gain (using alsamixer) is maximised.

- ```
  user@mona> ssh -L 5001:localhost:5001 dynalab
  user@dynalab> HPInterace 5001
  ```

  Same as for the master.

- ```
  user@mona> ssh -L 5002:localhost:5002 dynalab
  user@dynalab> CurrentSense 5002
  ```

  This measures the DC photocurrent making use of a STM32-dev board, which should appear as /dev/ttyUSB0.

To see exactly what each program requires as input and what it returns as output, please refer to the source code.
To perform a piezo scan, use "PiezoScanner"-software and the associated config file. It requires a config file besides a "piezo_scans" directory in the user's home directory, where the results are saved.
To perform an FMR measurement (field or frequency), use "FMRScanner"-software and the associated config file. It requires a config file besides a
  ```

"fmr_scans" directory in the user his home directory. Besides saving the spectrum, it also adds the users comments, together with the filename of the spectrum in "index.txt".
Commands given to a server are always in ASCII, always capital letters. When (multiple) arguments are given, they are seperated by comma's. For example, the set the position of the piezo stage halfway in each direction, the command will be (given to "Controller"): SET,POSITION,0.5,0.5,0.5,0.0
To set the HP 8672A to 6.2GHz: SET,FREQ,6.2e9
Physical values (frequency, current, ...) will always be handled in SI-units. Piezo position and magnet current are limited between 0 and 1, no unit.
Each server will always reply with two int32_t values. The first holds the exit code, 1/SUCCESS if all went well. The second holds the number of bytes that will be returned to the user. If something went wrong, the resulting error code can be looked up in "Libraries/errors.h". If you do not read all bytes present, they may be present in the input buffer when you read at a later point in time. After these two bytes come the rest of the data. Returns are binary, not ASCII, unless the ID is requested.
Each server will always reply to the "ID" command with their respective identification string.
"ScannerGUI" might also be useful. This enables moving the piezo stage from the desktop using a graphical user interace.
The software set can be downloaded from `https://github.ugent.be/mahelsen/SetupSoftware`.

Bibliography

[1] B. Russell, *History of Western Philosophy*. George Allen & Unwin Ltd., 1946.

[2] R. Feynman, R. Leighton, and M. Sands, *The Feynman Lectures on Physics*, vol. 2. Addison-Wesley Publishing Co., Inc., 1963.

[3] J. M. D. Coey, *Magnetism and Magnetic Materials*. Cambridge University Press, 2009.

[4] J. Stöhr and C. Siegmann, *Magnetism From Fundamentals to Nanoscale Dynamics*. Springer-Verlag, 2006.

[5] J. Mathon and A. Umerski, *Physics of Low Dimensional Systems*. Kluwer/Plenum, 2001.

[6] A. Vansteenkiste, *Dynamics of magnetic vortices in nanodots: experiment and simulation*. PhD thesis, Ghent University, 2009.

[7] D. Ralph and M. Stiles, "Spin transfer torques," *Journal of Magnetism and Magnetic Materials*, vol. 320, no. 7, pp. 1190 – 1216, 2008.

[8] T. Moriya, "Anisotropic Superexchange Interaction and Weak Ferromagnetism," *Phys. Rev.*, vol. 120, pp. 91–98, Oct 1960.

[9] A. Vansteenkiste, J. Leliaert, M. Dvornik, M. Helsen, F. Garcia-Sanchez, and B. Van Waeyenberge, "The design and verification of mumax3," *AIP Advances*, vol. 4, no. 10, p. 107133, 2014.

[10] S. Demokritov and A. Slavin, *Magnonics: From Fundamentals to Applications*. Springer-Verlag, 2013.

[11] A. Slavin, "Dipole-Exchange Spin Wave Spectrum in Magnetic Films and Finite-Size Magnetic Elements," Presented at the International Advanced School on Magnonics, 2012.

[12] M. Helsen, A. Gangwar, A. Vansteenkiste, and B. Van Waeyenberge, "Magneto-optical spectrum analyzer," *Rev. Sci. Instrum.*, vol. 85, p. 083902, 2014.

[13] Y. Acremann, C. H. Back, M. Buess, O. Portmann, A. Vaterlaus, D. Pescia, and H. Melchior, "Imaging Precessional Motion of the Magnetization Vector," *Science*, vol. 290, no. 5491, pp. 492–495, 2000.

[14] C. Davis, *Lasers and Electro-Optics: Fundamentals and Engineering*. Cambridge University Press, 1996.

[15] S. Demokritov, B. Hillebrands, and A. Slavin, "Brillouin light scattering studies of confined spin waves: linear and nonlinear confinement," *Phys. Rep.*, vol. 348, pp. 441–489, 2001.

[16] A. Kos, T. Silva, and P. Kabos, "Pulsed inductive microwave magnetometer," *Rev. Sci. Instrum.*, vol. 73, p. 3563, 2002.

[17] T. Silva, C. Lee, T. Crawford, and C. Rogers, "Inductive measurement of ultrafast magnetization dynamics in thin-film permalloy," *J. Appl. Phys.*, vol. 85, p. 7849, 1999.

[18] I. Neudecker, G. Woltersdorf, B. Heinrich, T. Okuno, G. Gubbiotti, and C. Back, "Comparison of frequency, field, and time domain ferromagnetic resonance methods," *J. Magn. Magn. Mater.*, vol. 307, pp. 148–159, 2006.

[19] S. S. Kalarickal, P. Krivosik, M. Wu, C. E. Patton, M. L. Schneider, P. Kabos, T. Silva, and J. P. Nibarger, "Ferromagnetic resonance linewidth in metallic thin films: Comparison of measurement methods," *J. Appl. Phys.*, vol. 99, p. 093909, 2006.

[20] M. Goto, H. Hata, A. Yamaguchi, Y. Nakatani, T. Yamaoka, Y. Nozaki, and H. Miyajima, "Electric spectroscopy of vortex states and dynamics in magnetic disks," *Phys. Rev. B*, vol. 84, p. 064406, Aug 2011.

[21] T. Tyliszczak and K. Chou, *Advances in Magnetization Dynamics Using Scanning Transmission X-Ray Microscopy*. Wiley-VCH, 2010.

[22] M. Bolte, G. Meier, B. Krüger, A. Drews, R. Eiselt, L. Bocklage, S. Bohlens, T. Tyliszczak, A. Vansteenkiste, B. Van Waeyenberge, K. W. Chou, A. Puzic, and H. Stoll, "Time-resolved x-ray microscopy of spin-torque-induced magnetic vortex gyration," *Phys. Rev. Lett.*, vol. 100, p. 176601, Apr 2008.

[23] A. Vansteenkiste, K. W. Chou, M. Weigand, M. Curcic, V. Sackmann, H. Stoll, T. Tyliszczak, G. Woltersdorf, C. H. Back, G. Schutz, and B. Van Waeyenberge, "X-ray imaging of the dynamic magnetic vortex core deformation," *Nat Phys*, vol. 5, pp. 332–334, May 2009.

[24] M. Kammerer, M. Weigand, M. Curcic, M. Noske, M. Sproll, A. Vansteenkiste, B. Van Waeyenberge, H. Stoll, G. Woltersdorf, C. Back, and G. Schütz, "Magnetic vortex core reversal by excitation of spin waves," *Nat. Comm.*, vol. 2, p. 279, 2011.

[25] R. Follath, J. S. Schmidt, M. Weigand, and K. Fauth, "The X-ray microscopy beamline UE46-PGM2 at BESSY," in *10th International Conference on Synchrotron Radiation Instrumentation*, pp. 323–326, 2010.

[26] P. Guttmann and C. Bittencourt, "Overview of nanoscale NEXAFS performed with soft X-ray microscopes," *Beilstein Journal of Nanotechnology*, vol. 6, pp. 595–604, 2015.

[27] G. Schütz, W. Wagner, W. Wilhelm, P. Kienle, R. Zeller, R. Frahm, and G. Materlik, "Absorption of circularly polarized x rays in iron," *Phys. Rev. Lett.*, vol. 58, pp. 737–740, Feb 1987.

[28] C. T. Chen, N. V. Smith, and F. Sette, "Exchange, spin-orbit, and correlation effects in the soft-x-ray magnetic-circular-dichroism spectrum of nickel," *Phys. Rev. B*, vol. 43, pp. 6785–6787, Mar 1991.

[29] R. Azzam and N. Bashara, *Ellipsometry and Polarized Light*. North-Holland Publishing Company, 1977.

[30] H. Hulme, "The Faraday Effect in Ferromagnetics," *Proc. Roy. Soc. A*, vol. 135, pp. 237–257, 1932.

[31] P. N. Argyres, "Theory of the Faraday and Kerr Effects in Ferromagnetics," *Phys. Rev.*, vol. 97, no. 2, p. 334, 1955.

[32] F. Mitschke, *Fiber Optics: Physics and Technology*. Springer-Verlag, 2010.

[33] Z. Qiu and S. Bader, "Surface magneto-optic Kerr effect," *Rev. Sci. Instrum.*, vol. 71, no. 3, p. 1243, 2000.

[34] C.-Y. You and S.-C. Shin, "Derivation of simplified analytic formulae for magneto-optical Kerr effects," *J. Appl. Phys.*, vol. 69, pp. 1315–1317, 1996.

[35] O. Svelto, *Principles of Lasers*. Springer-Verlag, 5 ed., 2010.

[36] P. Berger, "MSM photodiodes," *IEEE Potentials*, vol. 15, pp. 25–29, 1996.

[37] K. electronic GmbH, "KU LNA BB 2001200 A, Low Noise Amplifier." `http://www.kuhne-electronic.de/`, 2014.

[38] Mini-Circuits, "Frequency Mixer wide band ZX05-153+." `http://www.minicircuits.com/`, 2014.

[39] P. Keatley, *Time-Resolved Magneto-Optical Investigations of Picosecond Magnetisation Dynamics in Arrays of Non-Ellipsoidal Ferromagnetic Nano-Elements*. PhD thesis, University of Exeter, 2008.

[40] M. Polyanskiiy, "Refractiveindex." `http://www.refractiveindex.info`, 2014.

[41] M. Veis and R. Antos, "Advances in Optical and Magnetooptical Scatterometry of Periodically Ordered Nanostructured Arrays," *J. Nanomater.*, vol. 2013, p. 621531, 2012.

[42] D. M. Pozar, *Microwave Engineering*. Wiley, 4th ed., 2011.

[43] Sonnet Software, "Sonnet lite," 2013. `http://www.sonnetsoftware.com`.

[44] J. Griffiths, "Anomalous High-frequency Resistance of Ferromagnetic Materials," *Nature*, vol. 158, pp. 670–671, 1946.

[45] W. A. Yager and R. M. Bozorth, "Ferromagnetic Resonance at Microwave Frequencies," *Phys. Rev.*, vol. 72, pp. 80–81, Jul 1947.

[46] C. Kittel, "On the Theory of Ferromagnetic Resonance Absorption," *Phys. Rev.*, vol. 73, pp. 155–161, 1948.

[47] M. Helsen, A. Gangwar, J. De Clercq, A. Vansteenkiste, M. Weigand, C. H. Back, and B. Van Waeyenberge, "Non-linear radial spinwave modes in thin magnetic disks," *Applied Physics Letters*, vol. 106, no. 3, p. 032405, 2015.

[48] A. A. Thiele, "Steady-State Motion of Magnetic Domains," *Phys. Rev. Lett.*, vol. 30, pp. 230–233, Feb 1973.

[49] K. Y. Guslienko, "Magnetic Vortex State Stability, Reversal and Dynamics in Restricted Geometries," *J. Nanosci. Nanotechnol.*, vol. 8, no. 6, pp. 2745–2760, 2008.

[50] D. L. Huber, "Equation of motion of a spin vortex in a two dimensional planar magnet," *Journal of Applied Physics*, vol. 53, no. 3, pp. 1899–1900, 1982.

[51] B. Van Waeyenberge, A. Puzic, H. Stoll, K. Chou, T. Tyliszczak, R. Hertel, M. Fähnle, H. Brückl, K. Rott, G. Reiss, I. Neudecker, D. Weiss, C. Back, and G. Schütz, "Magnetic vortex core reversal by excitation with short bursts of an alternating field," *Nature*, vol. 444, pp. 461–464, 2006.

[52] M. Curcic, B. Van Waeyenberge, A. Vansteenkiste, M. Weigand, V. Sackmann, H. Stoll, M. Fähnle, T. Tyliszczak, G. Woltersdorf, C. H. Back, and G. Schütz, "Polarization Selective Magnetic Vortex Dynamics and Core Reversal in Rotating Magnetic Fields," *Phys. Rev. Lett.*, vol. 101, p. 197204, Nov 2008.

[53] L. Giovannini, F. Montoncello, F. Nizzoli, G. Gubbiotti, G. Carlotti, T. Okuno, T. Shinjo, and M. Grimsditch, "Spin excitations of nanometric cylindrical dots in vortex and saturated magnetic states," *Phys. Rev. B*, vol. 70, p. 172404, Nov 2004.

[54] M. Buess, R. Höllinger, K. Perzlmaier, U. Krey, D. Pescia, M. Scheinfein, D. Weiss, and C. Back, "Fourier Transform Imaging of Spin Vortex Eigenmodes," *Phys. Rev. Lett.*, vol. 93, p. 077207, 2004.

[55] K. Vogt, O. Sukhostavets, H. Schultheiss, B. Obry, P. Pirro, A. A. Serga, T. Sebastian, J. Gonzalez, K. Y. Guslienko, and B. Hillebrands, "Optical detection of vortex spin-wave eigenmodes in microstructured ferromagnetic disks," *Phys. Rev. B*, vol. 84, p. 174401, Nov 2011.

[56] K. Y. Guslienko, W. Scholz, R. W. Chantrell, and V. Novosad, "Vortex-state oscillations in soft magnetic cylindrical dots," *Phys. Rev. B*, vol. 71, p. 144407, Apr 2005.

[57] M. G. et al, "GNU Scientific Library Reference Manual." `http://www.gnu.org/software/gsl/`, 2014.

[58] ImageMagick Studio LLC, "ImageMagick." `http://www.imagemagick.org/`, 2014.

[59] M.-W. Yoo, J. Lee, and S.-K. Kim, "Radial-spin-wave-mode-assisted vortex-core magnetization reversals," *Applied Physics Letters*, vol. 100, no. 17, pp. –, 2012.

[60] R. Wang and X. Dong, "Sub-nanosecond switching of vortex cores using a resonant perpendicular magnetic field," *Applied Physics Letters*, vol. 100, no. 8, 2012.

[61] K.-W. Moon, B. S. Chun, W. Kim, Z. Q. Qiu, and C. Hwang, "Duffing oscillation-induced reversal of magnetic vortex core by a resonant perpendicular magnetic field," *Sci. Rep.*, vol. 4, p. 6170, Aug. 2014.

[62] A. Drews, B. Krüger, G. Selke, T. Kamionka, A. Vogel, M. Martens, U. Merkt, D. Möller, and G. Meier, "Nonlinear magnetic vortex gyration," *Phys. Rev. B*, vol. 85, p. 144417, Apr 2012.

[63] M. Bauer, O. Büttner, S. Demokritov, B. Hillebrands, V. Grimalsky, Y. Rapoport, and A. Slavin, "Observation of Spatiotemporal Self-Focusing of Spin Waves in Magnetic Films," *Phys. Rev. Lett.*, vol. 81, pp. 3769–3772, 1998.

[64] A. Thiaville, J. M. Garcia, R. Dittrich, J. Miltat, and T. Schrefl, "Micromagnetic study of bloch-point-mediated vortex core reversal," *Phys. Rev. B*, vol. 67, p. 094410, Mar 2003.

[65] O. V. Pylypovskyi, D. D. Sheka, V. P. Kravchuk, F. G. Mertens, and Y. Gaididei, "Regular and chaotic vortex core reversal by a resonant perpendicular magnetic field," *Phys. Rev. B*, vol. 88, p. 014432, Jul 2013.

[66] H. T. Nembach, J. M. Shaw, C. T. Boone, and T. J. Silva, "Mode- and size-dependent landau-lifshitz damping in magnetic nanostructures:

Evidence for nonlocal damping," *Phys. Rev. Lett.*, vol. 110, p. 117201, Mar 2013.

[67] T. Orth, U. Netzelmann, R. Kordecki, and J. Pelzl, "Imaging of magnetic materials by photothermally modulated ferromagnetic resonance," *J. Magn. Magn. Mater.*, vol. 83, pp. 539–540, 1990.

[68] A. Baman, T. Kimura, Y. Otani, Y. Fukuma, K. Akahane, and S. Meguro, "Benchtop time-resolved magneto-optical Kerr magnetometer," *Rev. Sci. Instr.*, vol. 79, p. 123905, 2008.

[69] C. Kittel, "Interpretation of Anomalous Larmor Frequencies in Ferromagnetic Resonance Experiment," *Phys. Rev.*, vol. 71, pp. 270–271, 1947.

[70] K. S. Buchanan, M. Grimsditch, F. Y. Fradin, S. D. Bader, and V. Novosad, "Driven dynamic mode splitting of the magnetic vortex translational resonance," *Phys. Rev. Lett.*, vol. 99, p. 267201, Dec 2007.

[71] A. Vansteenkiste, J. De Baerdemaeker, K. Chou, H. Stoll, M. Curcic, T. Tyliszczak, G. Woltersdorf, C. Back, G. Schütz, and B. Van Waeyenberge, "Influence of domain wall pinning on the dynamics behaviour of magnetic vortex structures: Time-resolved scanning x-ray transmission microscopy in NiFe thin film structures," *Phys. Rev. B*, vol. 77, p. 144420, 2008.

[72] T. Kamionka, M. Martens, K. Chou, M. Curcic, A. Drews, G. Schütz, T. Tyliszczak, H. Stoll, B. Van Waeyenberge, and G. Meier, "Magnetic Antivortex-Core Reversal by Circular-Rotation Spin Currents," *Phys. Rev. Lett.*, vol. 105, p. 137204, 2010.

[73] V. Castel, J. Ben Youssef, F. Boust, R. Weil, B. Pigeau, G. de Loubens, V. V. Naletov, O. Klein, and N. Vukadinovic, "Perpendicular ferromagnetic resonance in soft cylindrical elements: Vortex and saturated states," *Phys. Rev. B*, vol. 85, p. 184419, May 2012.

[74] J. Park and P. Crowell, "Interactions of Spin Waves with a Magnetic Vortex," *Phys. Rev. Lett.*, vol. 95, p. 167201, 2005.

[75] K. Guslienko, X. Han, D. Keavney, R. Divan, and S. Bader, "Magnetic Vortex Core Dynamics in Cylindrical Ferromagnetic Dots," *Phys. Rev. Lett.*, vol. 96, p. 067205, 2006.

[76] S.-B. Choe, Y. Acremann, A. Scholl, A. Bauer, A. Doran, J. Stöhr, and H. Padmore, "Vortex Core-Driven Magnetization Dynamics," *Science*, vol. 304, pp. 420–422, 2004.

[77] Y. Acremann, M. Buess, C. Back, M. Dumm, G. Bayreuther, and D. Pescia, "Ultrafast generation of magnetic fields in a Schottky diode," *Nature*, vol. 414, pp. 51–54, 2001.

[78] H. Bennett and E. Stern, "Faraday Effect in Solids," *Phys. Rev.*, vol. 137, pp. 448–461, 1965.

[79] A. Awad, K. Guslienko, J. Sierra, G. Kakazei, V. Metlushko, and F. Aliev, "Precise probing spin wave mode frequencies in the vortex state of circular magnetic dots," *Appl. Phys. Lett.*, vol. 96, p. 012503, 2010.

[80] I. Neudecker, G. Woltersdorf, B. Heinrich, T. Okuno, G. Gubbiotti, and C. Back, "Comparison of frequency, field, and time domain ferromagnetic resonance methods," *J. Magn. Magn. Mater.*, vol. 307, p. 148, 2006.

[81] S. Kalarickal, P. Krivosik, M. Wu, C. Patton, M. Schneider, P. Kabos, T. Silva, and J. Nibarger, "Ferromagnetic resonance linewidth in metallic thin films: Comparison of measurement methods," *J. Appl. Phys.*, vol. 99, p. 093909, 2006.

[82] J. Zak, E. Moog, C. Liu, and S. Bader, "Universal approach to magneto-optics," *J. Magn. Magn. Mater.*, vol. 89, p. 107, 1990.

[83] S. Polisetty, J. Scheffler, S. Sahoo, Y. Wang, T. Mukherjee, X. He, and C. Binek, "Optimization of magneto-optical kerr setup: Analyzing experimental assemblies using Jones matrix formalism," *Rev. Sci. Instrum.*, vol. 79, p. 055107, 2008.

[84] A. Zvezdin and V. Kotov, *Modern Magnetooptics and Mangetooptic Materials*. Institute of Physics Publishing, 1997.

[85] P. Keatley, V. Kruglyak, R. Hicken, J. Childress, and J. Katine, "Acquisition of vector hysteresis loops from micro-arrays of nano-magnets," *J. Magn. Magn. Mater.*, vol. 306, p. 298, 2006.

[86] T. Silva and A. Kos, "Nonreciprocal differential detection method for scanning Kerr-effect microscopy," *J. Appl. Phys.*, vol. 81, p. 5015, 1997.

[87] P. Horowitz and W. Hill, *The art of electronics*. Cambridge University Press, 1989.